Politecnico di Milano
Scuola dell'Ingegneria Industriale e dell'Informazione
Corso di Laurea Specialistica in Ingegneria Fisica

Tesi di laurea

TOWARDS SPIN ORBITRONICS: INVESTIGATION OF THE FERROELECTRIC RASHBA SEMICONDUCTOR GeTe

Relatore:
Dott. Matteo Cantoni
Correlatori:
Dott. Christian Rinaldi
Prof. Riccardo Bertacco

Candidato:
Stefano Bertoli
Matr. 780517

Anno Accademico 2012-2013

Contents

Prefazione **xi**

Preface **xv**

1 Introduction to Semiconductor Spintronics **1**

1.1 Spin Injection 2

1.1.1 Current Spin Polarization 3

1.1.2 Spin Injection in Semiconductors 3

1.2 Spin Transport 9

1.3 Spin Manipulation 11

1.4 Spin Lifetime Measurements 13

1.4.1 Hanle Effect 14

1.4.2 Three Terminals Geometry 16

1.4.3 Four Terminals Geometry 18

1.4.4 Non-Local Resistance 19

1.5 Classical Spintronics Devices 21

1.5.1 The Datta and Das SpinFET 27

2 Spin-Orbitronics **30**

2.1 Introduction 30

2.2 Anatomy of the Rashba Effect 32

2.3 FerroElectric Rashba SemiConductor: GeTe 34

2.4 Spin Hall Effect 37

2.5 GeTe-based Concept Devices 40

3 Experimental Techniques **45**
3.1 LASSE: LAyered Structures for Spin Electronics 45
3.1.1 Structure 46
3.1.2 Molecular Beam Epitaxy 49
3.2 Magnetron Sputtering 50
3.3 Low Energy Electron Diffraction: LEED 52
3.4 Photoemission Spectroscopy 56
3.4.1 Three Steps Model 58
3.4.2 Angle Resolved Photoemission Spectroscopy 61
3.4.3 Synchrotron Light Source 62
3.5 Wet Etching 64
3.6 Optical Lithography 65
3.6.1 Direct Photolithography 66
3.6.2 Inverse Photolithography 67
3.7 Hall Effect Measurements 68
3.8 Hanle Effect Measurements 70

4 Investigation of Germanium Telluride **74**
4.1 Introduction 74
4.2 Sample Batches 76
4.3 Surface Preparation 76
4.3.1 Capping Layer's Removal 77
4.3.2 Surface Recovery 79
4.3.3 Antimony Content Analysis 86
4.4 Ferroelectric Characterization 89
4.5 ARPES on GeTe 91
4.5.1 Bands Dispersion Analysis 92
4.5.2 Spin-Resolved ARPES 101
4.6 Fe Growth on GeTe Surface 106
4.7 Hall Measurements 109
4.8 Spin Lifetime in Germanium 112

Conclusions and Perspectives **118**

List of Figures

1.1 (a). Spins injection from a ferromagnet (FM) into a non-magnetic material (N). J is the density of current. (b) Spatial distribution of the magnetization. 4

1.2 Sketch of the electrical situation using the two currents model for (**a**) a FM/SC device or (**b**) a FM/B/SC device. 4

1.3 Current spin polarization (α) for different interfaces: (1) Co/Cu (FM/NM), (2) Co/SC, (3) Co/B/SC (eq. 1.7) [1]. 7

1.4 Schematic view of (a) the lateral geometry of electrodes and (b) the perpendicular to plane geometry. 9

1.5 Schematic view of the spin Hall effect transistor designed by Wunderlich et al. [2]. The basic idea is that a circular polarized light hits the sample, inducing a spin population in the Hall bar. The gate voltage V_G is capable of controlling the precession of the spins and changing the R_H value. 13

1.6 Schematic view of the Hanle effect with and without an out-of-plane magnetic field. The connection between the Lorentzian line-shape and the spin lifetime is evidenced. Figure from ref. [3]. 15

1.7 Sketch of the three terminals geometry used for spin lifetime measurements in Germanium by Hanbicki et al. [4]. 16

1.8 (**a**)Inhomogeneous magnetic field caused by a sinusoidal roughness profile with wavelength λ. The precession of spins due to interaction with the field is represented and modifies the original in-plane magnetization of the injected spins. (**b**)Trend of $\Delta\mu$ spin accumulation for a rough interface compared to a perfect one. The decreasing due to a rough interface is evident. See ref. [5] 17
1.9 Inverted Hanle and Hanle signals for different surfaces [5]. . 17
1.10 Scheme of the four terminals geometry for non-local spin lifetime measurements on Germanium. The figure is taken from Chang et al. [6]. 18
1.11 Non local resistance measured in slightly n-doped Germanium by Zhou et al. (ref. [7]):1-D diffusion model fittings for parallel and anti-parallel orientations of the electrodes' magnetizations. 19
1.12 Non local resistance measured at 4 K in a four terminals device by Zhou et al. [7]. The blue arrows indicate the magnetization orientations. 21
1.13 Resistance (with respect to zero-field value) of three Fe/Cr superlattices with different non-magnetic thicknesses at 4.2 K. Current and applied field are in the same plane of the layers [8] 22
1.14 Spin-valve based on the GMR effect. The left image represents the case of applied field (H_s in eq. 1.20); the right one is the case without applied field. 23
1.15 Two-currents model applied to the TMR case. The resistance of the parallel case is smaller than the anti-parallel case because the DOS in the first ferromagnet granted a large number of electrons and the second FM has a large availability of states. 24
1.16 STT switching processes: from anti-parallel (AP) to parallel (P) (**a**) and from P to AP (**b**) [9]. 26
1.17 The original Datta and Das concept of the spin-FET 27

2.1 Sketch representing all the effects and technology that are merged together in FerroElectric Rashba SemiConductors [10]. 32
2.2 Rashba effect. The α_R parameter indicates the intensity of the effect. 34
2.3 Band structure of GeTe (a). The figure (b) shows a magnification around the Z point. The zero of the energy scale is given by the predicted Fermi level. 35
2.4 The inversion of electric polarization causes the entirely spin texture to flip. 36
2.5 Rashba parameters E_R, k_R and α_R as a function of the GeTe ferroelectric order parameter τ. 37
2.6 The carriers involved are electrons. The first image presents the Hall effect, where the Lorentz force generates charge imbalance. In the case of SHE, the V_{SH} voltage has opposite sign for spin up and down electrons [11]. 38
2.7 Non-volatile spinFET device concept. Gate voltage and back contact allow the switch of the ferroelectric polarization. . . 41
2.8 Table of truth of a GeTe-based spinFET. Different rows correspond to different combinations of electrodes' magnetizations and channel polarization. The high (low) resistance state H (L) refers to a logic state 1(0). 42
2.9 The FERSC channel generates an in-plane spin-polarized current and a spin and charge accumulations in the up-down directions. Switching the ferroelectric polarization corresponds to a switching in the resistance state, because the spins change their orientation with respect to the FM magnetization. . . . 43
2.10 (a) An out-of-plane spin polarized current is formed in the FERSC channel. The gate voltage determines the FE polarization and therefore the spin orientation. Due to the SHE, a spin and charge right-left accumulation occurs determining a lateral voltage. The switching of the polarization implies a change in sign of the lateral voltage. (b) Sketch of the multi-gate (3) Spin Hall Transistor. 44

3.1 Schematic plain view of LASSE. 46

3.2 Sketch representing (a) the shuttle on which the sample is mounted on, (b) the fork and (c) the sample holder. 47
3.3 Schematic view of the magnetron sputtering process. 51
3.4 AJA ATC Orion sputtering system. A is the deposition chamber, B the load-lock, C the transfer arm, D the generators that power the sources located under the deposition chamber. . . 51
3.5 Schematic view of the LEED system. 53
3.6 (a) Ewald sphere in a 2D lattice electrons' diffraction. (b) Ewald sphere in the case the electrons probe more than one layer. The third Laue condition thickens the rods, modifying the resulting intensity. 54
3.7 Sketch of the geometry of a LEED experiment. 56
3.8 Schematic view of a photoemission experiment. (a) Geometry of the problem. (b) Band structure of a semiconductor during a PES experiment. (c) Electron wave-vectors situation: the parallel component $k_{\parallel}$ conserves while the perpendicular one ($k_{\perp}$) does not because of the symmetry break of the surface. 58
3.9 Scheme of a synchrotron as light source. It is possible to distinguish the booster, the storage ring and some beamlines. 62
3.10 Beam train seen on an oscilloscope. The figure is taken from the Elettra lightsource site(www.elettra.trieste.it). 64
3.11 Schematic view of the steps in a direct photolithography process. 65
3.12 Karl Suss MA56 mask aligner. 66
3.13 Setup for a Hall measurement for electrons. Thanks to Wikipedia for the image. 68
3.14 Picture of the Cryogenic cryomagnetic system. 70
3.15 Optical microscopy (5 X) image of a three terminals structure. 71
3.16 **(a)** Set up used for three terminals geometry Hanle measurements. There are two electromagnets that grant in-plane (inverted Hanle) and out-of-plane (Hanle) fields. **(b)** Particular of the sample mounted in the cryostat. 72

4.1 (a) 10 x 10 μm^2 AFM images of Germanium Telluride (73 nm) surface with the silicon nitride capping layer (30 nm). The chromatic scale indicates the third coordinate. (b) Surface profile along a line of fig. (a). 77

4.2 AFM imaging on samples with 73 nm of $GeTe$ and 30 nm of Si_3N_4. (a) 10 x 6.5μm^2 image of the surface after 9 minutes of wet etching. The silicon nitride residues are imaged as bright points on the GeTe surface. (b) Depth profile of (a) surface; the RMS value is 6 nm while the flat zones roughness is 0.3 − 0.5 nm. (c) 10 x 10μm^2 surface image of a sample from the same substrate after a longer wet etching time: 20 minutes almost remove the capping layer. The RMS value is about 4 nm and the one of the flat zones is 0.5 nm. (d) 3D image of the surface corresponding to panel (c). 78

4.3 2 x 2μm^2 AFM image of a sample with 73 nm $GeTe$ and 30 nm Si_3N_4 after wet etching. Black lines have been drawn as a guide for the eyes to show the presence of triangular domains. 80

4.4 XPS (Al-Kα) chemical analysis on GeTe after 30 min of sputtering at 700 eV. The peaks of Te 4d and Ge 3d (a), O1s (b) and C1s (c) are represented. From figure (a) it is possible to deduce the stoichiometry of the sample by evaluating the ratio between the intensity of Te 4d peak and Ge 3d peak, both normalized to their cross sections and transmission coefficients. In this case the stoichiometry is $Ge_{0.47}Te_{0.53}$. . . . 81

4.5 XPS (Mg-Kα) Ge 3d peak. The two oxidation states are visible and the peaks are deconvolved. The chemical shifts are 3.2 eV for GeO_2 and 1.6 eV for GeO. The latter shift value differs from the one seen on germanium [12]. 83

4.6 Ratio between the intensities (normalized to the cross section and the transmission coefficient) of O 1s and C 1s peaks and the intensity of Ge 3d + Te 4d versus the sputtering time. The sputtering energy is 700 eV and the incident angle is 60°. 84

4.7 From the relative intensity of Te 4d and Ge 3d peaks in the XPS spectra it is possible to obtain the element content (%) within Ge_xTe_{1-x}. The clear tendency is the evaporation of Te that leaves a Ge-rich film. 85

4.8 From left to right: zinc-blende (111) surface lattice in which the hexagonal symmetry is evidenced; theoretical bulk first Brillouin zone: the (111) surface is in red and not equivalent high symmetry directions ZA and ZU are shown; the surface reciprocal lattice and the deduced Wigner-Seitz cell: not equivalent directions $\bar{\Gamma}\bar{K}$ and $\bar{\Gamma}\bar{M}$ are shown. We underline that the $\bar{\Gamma}\bar{M}$ ($\bar{\Gamma}\bar{K}$) surface direction is equivalent to the ZU (ZA) bulk direction. 86
4.9 LEED diffraction figure on a GeTe sample (taken at 114 eV). The diffraction points are evidenced by red circles and the Wigner-Seitz cell of the surface is illustrated. It is possible to distinguish the two not equivalent directions $\bar{\Gamma}\bar{K}$ and $\bar{\Gamma}\bar{M}$ according to the surface nomenclature. 87
4.10 O 1s, Sb 3d 3/2 and 5/2 peaks obtained by Mg-Kα XPS analysis on a GeTe sample. The Sb peaks are partially covered by the oxygen one. The percentage of oxidation is about 15% and the antimony contamination is 0.37% with respect to Ge and Te intensities. 88
4.11 Intensity of Sb 3d, Ge 3d + Te 4d, Si 2p + N 1s peaks and percentage of Sb content with respect to GeTe. We gradually removed the Si_3N_4 capping layer (within 150 min of sputtering in UHV) and then we proceeded with thermal treatments in order to obtain a good surface. Only after the annealing at 250°C, a small Sb 3d peak appears in the XPS spectrum. The Sb content is limited to fraction of percent even after very long thermal treatments and always increases with the annealing time (and temperature). 89
4.12 (a) Topography of the GeTe surface. Triangular domains and silicon nitride residues can be distinguished (see sec. 4.3). (b) Vertical piezo response phase after the application of 10 V bias to the square drawn in figure. 90
4.13 (a) LEED pattern of a GeTe sample in which rotation domains' presence is clearly distinguished. (b) First Brillouin zone of the surface reciprocal space corresponding to the LEED of panel (a). 92

4.14 Theoretical bulk bands calculated by Picozzi et al. [13]. The fig. (b) is a zoom of the panel (a) in the very proximity of the Z point and around the zero of the energy (the Fermi level of the calculated system). 93
4.15 Geometry of the ARPES experiment. 94
4.16 Measured band dispersion for a GeTe sample at different photon energies. For $h\nu = 22.5$ eV the maximum of the valence band is as close as possible to the Fermi level of the crystal (corresponding to binding energy $E_B = 0$). 96
4.17 (a) Experimental angular dispersion for $h\nu = 22.5$ eV in the $\bar{\Gamma}\bar{K}$ direction. (b) Theoretical surface (dashed line) and bulk (solid line) bands (ZA direction) [13] for GeTe. (c) Enlargement of the surface entering bands that shows the correspondence with theoretical calculations. (d) The red line shows the $\bar{\Gamma}\bar{K}$ direction (on the W.-S- cell) in which the angular dispersion is measured. 97
4.18 (a) Angular dispersion for $h\nu = 22.5$ eV in the $\bar{\Gamma}\bar{M}$ direction. (b) Theoretical surface (dashed line) and bulk (solid line) bands (ZU direction) [13] for GeTe. (c) The red line shows the $\bar{\Gamma}\bar{M}$ direction (on the W.-S- cell) in which the angular dispersion is measured. 98
4.19 Angular dispersion for $h\nu = 22.5$ eV in the $\bar{\Gamma}\bar{M}$ direction. The left half of image 4.18 has been mirrored. The panel on the right shows an enlargement of a bulk band. 99
4.20 GeTe calculated bands through one step photoemission calculations by J. Minar (LMU, Münich) (dots in figure) and measured surface bands (originating from Te states), represented with a second derivative filter. The surface states are shown to disperse changing the position along the ΓZ direction. 100
4.21 Photon energy: $h\nu = 22.5$ eV. Three iso-energy cuts are presented at (a) 0.1 eV, (b) 0.25 eV and (c) 0.4 eV binding energy. The energy cuts are represented as dashed lines on both the calculated and the measured carpet (at APE in July 2013). The band structure in the measured carpet is black on white background. 100

4.22 Experimental set-up of the COmplete PHotoEmission Experiment (COPHEE) at the Surface and Interface Spectroscopy beamline at the Swiss Light Source. The photoemitted electrons first pass a hemispherical electrostatic analyser and are then accelerated through an electron lens with chopper, onto the Mott detectors. This configuration allows for the simultaneous detection of the binding energy, momentum and all three components of the spin polarization vector of the electron [14]. 102
4.23 (a) Measured carpet along the $\bar{\Gamma}\bar{M}$ direction. The red solid line indicates the kinetic energy of the spin-resolved measurements. (b) Fitting with theoretical surface (dashed lines) and bulk (solid lines) bands along the $\bar{\Gamma}\bar{M}$ direction. (c) Mott counts (left and right) of the in-plane component of the photoelectrons' spins and raw spin asymmetry (calculated as the difference of the Mott counts). (d) In-plane polarization deduced from (c) after background subtraction. The arrows indicate the in-plane spin direction. 103
4.24 Summary image of the spin-resolved PES in GeTe at 18.30 eV kinetic energy, with 22.5 eV photon energy. The in-plane spin asymmetry measured with a single Mott can already demonstrate the rotation of spin in the iso-energy cut of the surface states that are crossing the Fermi level. 105
4.25 Iron b.b.c. (111) surface (by E. Hasselbrink, Universität Duisburg-Essen): the hexagonal structure can be distinguished. 106
4.26 Comparison between the LEED figures of a GeTe sample virgin (left) and with 2.5 nm Fe (right). In the image on the left the dashed line shows the sample profile. 107
4.27 Polar plot of the coercive field of Fe(2.5nm)/GeTe. The uniaxial anisotropy is not present if the sputtering at grazing incidence is not employed to clean the surface. 108

4.28 (a) Hysteresis loop for the Fe(2.5nm)/GeTe sputtered (60°) sample with the magnetic field applied at an angle θ with respect to the cleavage side. $\theta = 0°$ represents an easy axis, while $\theta = 90°$ is a hard axis. (b) Polar plot of the magnetization remanence. A uniaxial anisotropy is present along the cleavage side (0°). 109
4.29 Sketch of the Hall effect measurement. The current is considered as composed by holes only. 110
4.30 R_{xy} vs (positive) magnetic field at 1.6 K. The result is a straight line with positive slope. 111
4.31 Map of CoFeB/MgO contacts on Ge. The arrangement for non-local measurements is shown in green, while the three terminals arrangement is shown in black, as used for Hanle effect measurements. 113
4.32 NL signal with respect to the gap between the central electrodes. The spin diffusion length (L_s) is extracted by fitting with an exponential with 1.2μm characteristic length. 114
4.33 Hanle and inverted-Hanle peaks for different temperatures after linear background subtraction. The experimental data are presented as black points, while the Lorentzian fit is the red line. 115
4.34 (a) Spin lifetime in function of temperature. The value seems to be poorly dependent on temperature with a mean value of 156ps. (b) Spin signal vs temperature: the linear trend is evidenced in red. 116

Prefazione

Il lavoro sperimentale di tesi é stato svolto da me presso il gruppo NaBiS (NanoBiotechnology and Spintronics) nel centro L-NESS del Polo Regionale di Como del Politecnico di Milano. Il cordinatore del gruppo é il Prof. Riccardo Bertacco e nel corso di questo progetto sono stato seguito dal Dott. Matteo Cantoni e dal Dott. Christian Rinaldi.

L'attivitá di ricerca si inserisce nel contesto dell'elettronica di spin, in particolare della Spintronica su semiconduttori. Si tratta di un ramo di ricerca che recentemente ha acquisito grande rilevanza in quanto prevede l'integrazione di funzionalitá proprie dello spin in materiali dal largo bacino di applicazione commerciale (i.e. i semiconduttori del IV gruppo e i composti dei gruppi III-V).

L'inserimento di un grado di libertá rappresentato dallo spin nel contesto dell'elettronica permette di implementare nuove funzioni logiche basate sul concetto di quantum computer. La *Magneto-Resistenza Gigante* (GMR) e la *Tunnel Magneto Resistance* (TMR) sono due esempi di dispositivi spintronici basati sul paradigma di Mott: il cambio di resistenza elettrica dipende dall'orientazione relativa tra le magnetizzazioni di due layer ferromagnetici (FM). I metalli FM non si prestano facilmente alla miniaturizzazione e all'integrazione in circuiti ad alta densitá a causa dei campi magnetici (stray fields) che generano e del fatto che necessitano di ulteriori campi magnetici per riorientare le magnetizzazioni. Per superare questo problema negli ultimi anni la Spintronica si é evoluta verso il controllo elettrico della magnetizzazione, evitando i campi magnetici. Una via per ottenere questo risultato é tramite l'accoppiamento ferroelettrico/ferromagnetico: controllando la polarizzazione FE é possibile indurre una rotazione della magnetizzazione FM

[15]. Altrimenti, un'altra opzione sfrutta lo *Spin Transfer Torque* (STT) [16] per modificare la magnetizzazione di un layer iniettando una corrente spin-polarizzata.

D'altra parte, nonostante i problemi legati ai FM si possano risolvere in questi modi, la funzionalitá dei semiconduttori é necessaria per il controllo della resistivitá variando il drogaggio oppure sfruttando effetti di campo (come nel MOS-FET).

Un approccio non convenzionale per affrontare queste difficoltá é la *Spin Orbitronics*, recentemente introdotta da A. Fert (premio Nobel per la fisica nel 2007), capace di modificare le proprietá di spin nei materiali attraverso l'accoppiamento spin-orbita (SOC) senza usare una magnetizzazione netta. In questo contesto, la nuova classe di materiali *FerroElectric Rashba Semi-Conductors* (FERSC) [13] rappresenta una scoperta fondamentale, presentata in una recente pubblicazione di R. Bertacco *et al.*. In questi materiali il campo elettrico agisce sulle correnti di spin tramite *effetto Rashba*, i.e. un k-splitting delle bande di spin. I FERSC presentano un accoppiamento tra effetto Rashba e ferroelettricitá: l'inversione della polarizzazione ferroelettrica causa il ribaltamento dello spin nelle bande. La ferroelettricitá ha inoltre caratteristiche di memoria naturali, perció i FERSC possono essere utilizzati in memorie magnetiche a completo controllo elettrico.

Questo lavoro di tesi é stato svolto per un anno al centro L-NESS ed é principalmente focalizzato sullo studio e sulla caratterizzazione del *Tellurato di Germanio* (GeTe). Il GeTe é un semiconduttore che, secondo calcoli teorici, dovrebbe appartenere alla classe di materiali FERSC. Noi abbiamo verificato le proprietá teoriche del GeTe tramite studi di fotoemissione e misure di trasporto. Una parte del lavoro presentato in questa tesi é stato dedicato alla preparazione della superficie ed allo studio per spettroscopia a raggi X (XPS). Quindi, misure Angle-Resolved Photoemission Spectroscopy (ARPES) sono state effetuate al sincrotrone Elettra (Trieste) grazie alle quali la struttura a bande é stata osservata per la prima volta, e misure ARPES risolte in spin sono state eseguite al sincrotrone PSI (Villigen). La caratterizzazione elettrica dará interessanti informazioni riguardo al drogaggio ed al tipo di portatori tramite misure di effetto Hall. Il comportamento ferroelettrico é stato misurato con Piezo-Force Microscopy (PFM). Inoltre, la crescita del ferro sul GeTe verrá analizzata per verificare la fattibilitá di dispositivi su FERSC. Per la prima volta, questa tesi offre una caratteriz-

zazione esaustiva del GeTe in termini di struttura a bande e caratteristiche di trasporto.

Un punto fondamentale per le applicazioni spintroniche sui semiconduttori é un tempo di vita non trascurabile dello spin, dal momento che necessita di essere trasportato e manipolato. Nel corso di questo lavoro di tesi, é stato studiato l'*effetto Hanle* su germanio, dalla cui analisi é possibile dedurre il tempo di vita dello spin. Questa analisi ha lo scopo di acquisire il necessario know-how per una futura misura di tempo di vita sul GeTe tramite effetto Hanle.

La tesi é divisa in quattro capitoli:

- **Capitolo 1: Introduction to Semiconductor Spintronics**. Sono presentatialcuni importanti risultati della Spintronica classica. L'effetto Hanle viene descritto in quanto il tempo di vita di spin é fondamentale per i dispositivi spintronici.

- **Capitolo 2: Spin-Orbitronics**. É l'introduzione al nuovo paradigma per superare la classica Spintronica di Mott: é possibile rivoluzionare i dispositivi sfruttando l'accoppiamento spin-orbita nei materiali senza usare FM. Si descrive la scoperta e le proprietá della nuova classe di materiali FERSC. Inoltre, lo Spin Hall Effect (SHE) sará trattato in quanto strumento fondamentale per dispositivi spin-orbitronici.

- **Capitolo 3: Experimental Techniques**. Sono presentate le tecniche principalmente utilizzate durante il lavoro di tesi. In particolare si parlerá di: (i) tecniche per la preparazione di campioni e la crescita di eterostrutture (chemical wet etching, LASSE, MBE, magnetron sputtering); (ii) fotoemissione e diffrazione di elettroni per la caratterizzazione della qualitá delle eterostrutture (XPS, LEED, ARPES); (iii) tecniche per fabbricare e misurare dispositivi (litografia ottica, effetto Hall ed effetto Hanle).

- **Capitolo 4: Investigation of Germanium Telluride**. É dedicato all'attivitá sperimentale svolta durante il lavoro di tesi sul GeTe. I campioni studiati sono stati cresciuti da R. Calarco e collaboratori al Paul Drude Institut (PDI) di Berlino. Questo capitolo tratta l'ottimizzazione della preparazione di campioni con buone caratteristiche di superficie (nella sezione 4.3) per poter svolgere studi spettroscopici

e crescite di eterostrutture. Sono stati fatti esperimenti di Angle-Resolved PhotoEmission Spectroscopy (ARPES) (nella sez. 4.5) nella beamline APE al sincrotrone Elettra per investigare la struttura a bande. Descriviamo la caratterizzazione elettrica del GeTe (sez. 4.7). Inoltre, uno studio preliminare dell'effetto Hanle su germanio sará in grado di porre le basi per una futura misura di tempo di vita dello spin nel GeTe.

In questo lavoro di tesi per la prima volta si verificano le proprietá basilari del GeTe (il materiale per cui l'acronimo FERSC é stato creato): se le previsioni teoriche verranno confermate (come si é cominciato a fare in questa tesi) ci possiamo aspettare che il GeTe avrá un impatto eccezionale nel contesto dell'elettronica di spin.

Preface

The thesis' experimental work has been performed at the NaBiS (NanoBiotechnology and Spintronics) group in the L-NESS center of Polo Regionale di Como of Politecnico di Milano. The group coordinator is Prof. Riccardo Bertacco and during this project I have been followed by Dr. Matteo Cantoni and by Dr. Christian Rinaldi.

The research to which this work pertains concerns spin electronics (or "Spintronics"), in particular semiconductors' Spintronics. It is a branch of spin electronics that is considered relevant because it provides the integration of spin functionalities in materials (i.e. IV group semiconductors and III-V alloys) with a large field of commercial applications.

The insertion of the spin's degree of freedom in electronics permits the implementation of new logical functions based on quantum computer. The *Giant Magneto Resistance* (GMR) and the *Tunnel Magneto Resistance* (TMR) are two good examples of spintronic devices and are based on the Mott paradigm: the change of resistance depends on the relative orientation between magnetizations of two ferromagnetic (FM) layers. FM metals are not suitable for high density integration because of stray fields and because of they usually require magnetic fields to reorient their magnetizations. To overcome this issue, in the last years Spintronics has been evolving towards an electrical control of the magnetization, avoiding magnetic fields. One possibility is by ferroelectric/ferromagnetic coupling: controlling the FE polarization it is possible to induce a change in the FM magnetization [15]. Otherwise, Spin Transfer Torque (STT) [16] can rotate the magnetization of a FM layer through the injection of a spin current.

On the other end, even if the issues concerning metals can be solved in

these ways, recovering the semiconducting functionality is important for the control of resistivity by varying the doping level or by the field effect (as exploited in the MOS-FET).

An unconventional approach to overcome these issues is the *Spin-Orbitronics*, recently identified by Albert Fert (Nobel prize for Physics in 2007),that exploits the spin-orbit coupling (SOC) to modify the spin properties in materials without using a net magnetization. In this framework, a relevant discovery has been the novel class of *FerroElectric Rashba SemiConductors* (FERSCs) [13], presented in a recent publication of R. Bertacco *et al.*. In these materials, the electric field acts on the spin currents through the *Rashba effect*, i.e. the k-separation of spin bands. FERSCs present a coupling between Rashba effect and ferroelectricity: the ferroelectric polarization inversion causes the total reversal of the spin within the bands. The ferroelectricity has also an intrinsic memory behaviour, thanks to the remanence polarization, therefore FERSCs can be implemented in magnetic memories with full electrical control.

This thesis work has been carried out for one year at L-NESS center and is mainly focused on the *Germanium Telluride* (GeTe) study and characterization. GeTe is a semiconductor that, according to theoretical calculations, should belong to FERSC class of materials. We are going to test the theoretically predicted physical features of GeTe through photoemission and transport measurements. A part of the work reported here was dedicated to the surface's preparation procedure and to the X-ray Photoemission Spectroscopy (XPS) study. Then, Angle-Resolved Photoemission Spectroscopy (ARPES) measurements were performed at Elettra (Trieste) synchrotron where band structure has been observed for the fist time and spin-resolved ARPES measurements were carried out at PSI synchrotron (Villigen). The electrical characterization will provide interesting information about the doping level and the type through Hall effect measurements. The ferroelectric behaviour was investigated by Piezo-Force Microscopy (PFM). The iron growth on GeTe will be also analysed in order to test the feasibility of devices based on FERSCs. This thesis presents for the first time an exhaustive characterization of Germanium Telluride thin films in terms of band structure and transport features.

The spin lifetime in semiconductors needs to be large enough in order to permit spin transport and manipulation. For this reason, Hanle effect mea-

surements in germanium were performed spin lifetime was obtained in order to acquire of the necessary know-how and prepare for future measurement on GeTe.

The thesis is divided in four chapters:

- **Chapter 1: Introduction to Semiconductor Spintronics**. Some of the most important results of classic Spintronics (based on the Mott paradigm) are presented. Since the spin lifetime is a key parameter of spintronic devices, the Hanle effect is described.

- **Chapter 2: Spin-Orbitronics**. Introduction of a new paradigm that goes beyond "classical" Mott Spintronics: it is possible to build revolutionary spintronic devices based just on spin-orbit coupling (SOC) in materials, without the necessity to use FM materials. Among them, we describe the discover of the completely novel FerroElectric Rashba SemiConductors (FERSC) and the properties of Germanium Telluride. Furthermore, the Spin Hall Effect (SHE) is treated as a milestone for spin-orbitronic devices.

- **Chapter 3: Experimental Techniques**. It treats the principal experimental instruments and techniques employed during the thesis work. In particular, we describe: (i) the techniques/systems for sample preparation and heterostructures growth (chemical wet etching, LASSE UHV system, MBE, magnetron sputtering); (ii) photoemission and electron diffraction techniques to characterize the quality of thin films and heterostructures (XPS, LEED, ARPES); (iii) the techniques to fabricate and measure devices (optical lithography, Hall effect and Hanle effect).

- **Chapter 4: Investigation of Germanium Telluride**. Experimental activity performed on GeTe in the thesis. The samples studied were grown by Calarco's group at Paul Drude Institut (PDI) in Berlin. This chapter treats the optimization of samples surface preaparation (sec. 4.3) in order to employ GeTe spectroscopic studies and heterostructure growth. Deep Angle-Resolved Photo-Emission Spectroscopy (ARPES) studies (sec. 4.5) have been performed at APE beamline in the Elettra synchrotron to investigate the band dispersion of the valence band. We describe the electrical characterization of the material (sec. 4.7).

Furthermore, a preliminary study of Hanle effect on Germanium have been performed (in section 4.8) in order to measure spin lifetime in a reference well-know material, paving the way to a future application to GeTe.

For the first time, in this thesis work the basic features of *Germanium Telluride* (the first material for which the acronym FERSC has been coined) are verified: if the theoretical predictions will be confirmed (as partially done in this thesis), we should expect that the GeTe will have an exceptional impact in the Spintronics framework.

Chapter 1

Introduction to Semiconductor Spintronics

Electronics evolved with an expectational rhythm since its origin. Needs of storage capability, velocity and low power consumption have been the requirements to respect in order to improve the performance of devices and to limit costs. The use of semiconductors in integrated electronics permitted the fast development of circuits, memories and processors, making the fortune of several industries. The number of transistors per chip was expected to double every year by Gordon Moore in 1965 (*Moore's law*), but this forecast was not satisfied. In fact, in the last two decades progress has slowed down, due to the rising of quantum problems in reduced dimensions.

In this scenery, *Spintronics* was born. The question that afflicted millions of researchers was how to improve electronics' features without encountering miniaturization problems. There was the need to find a new physical property to exploit in order to rise the information content in a current. The answer to the question was spin. Electrons (and generally carriers) have a natural magnetic momentum, described by spin. This momentum interacts with magnetic field and, under particular conditions, with electric field, thus it is manipulable. Its *up* or *down* nature intrinsically contains the bit concept and perfectly adapts to an electronic application.

In 1936 Mott proposed the *two channels model* for spin transport: the two possible electron spins' states (”up” or ”down”) are independent and can be considered as two different channels. The demonstration of this con-

cept's validity was provided in 1988 by Fert and Grunberg. They discovered the *Giant Magneto Resistance* (GMR) effect [8] and gave the start to great interest in the applications of spins in electronics. The basic idea behind the classic Spintronics (also called *Mott Spintronics*) consists in changing the conductivity of a particular structure by modifying the relative orientation of two FM layers. This means that the logical bit of information is enclosed in the magnetizations' configuration of a FM-based structure.

The problems of spin-based electronics can be divided in four classes: injection, transport, detection and manipulation. For example, the spinFET (which will be treated in sec. 1.5.1) is a transistor that operates with spin polarized currents. Its realization needs to consider the problem of *injecting* spins into the semiconductor from a ferromagnetic electrode, the spin *transport* into the channel and the *detection* at another electrode. Furthermore, a transistor is a device capable of switching its behaviour, therefore a *manipulation* of the spins is necessary for its operation.

Semiconductors were chosen as leading actors for their properties and especially for their integrability with standard electronics. *Semiconductors Spintronics* studies the integration of spin-based structures into semiconductors. In order to obtain a good spin injection rate in semiconductors it is necessary to study the effect on the spins caused by the passage through a ferromagnet-semiconductor interface. Then it is important to understand if a carrier is able to travel into a SC without losing its spin polarization and eventually how the latter can be detected.

1.1 Spin Injection

A source of spins is easily found in ferromagnets. Spintronics in metals has limited attraction because it does not fit with integrated electronics and does not have some interesting features present, on the contrary, in semiconductors, i.e. the possibility of radically changing their electrical features modifying the number of impurities (doping level). Thus, there is the need to take those spins from the FM and inject them into the SC.

In a ferromagnet a spin polarized current is naturally obtained thanks to the bands' energy separation between majority and minority carriers. The

efficiency of the injection into the SC is the bottleneck in the process. Many kinds of interfaces have been proposed, such as ohmic contact or tunnel junction. Here we will deal with some of them and briefly compare them.

The spin injection of carriers in materials can be described by a simple model, elaborated by Mott [17]. This model considers negligible the scattering phenomena between electrons and magnons, capable of flipping the spin. Therefore, the total current is the sum of two independent channels, depending on the opposite spin direction with respect to a common axis. This treatment is called *two currents model* [18].

1.1.1 Current Spin Polarization

In the two currents model framework, a parameter α can express the spin polarization of the current and it is called *spin polarization*:

$$\alpha = \frac{J_{\uparrow} - J_{\downarrow}}{J_{\uparrow} + J_{\downarrow}} \tag{1.1}$$

where the J terms are density currents. The $\uparrow$ refers to the majority carriers and the $\downarrow$ to the minority ones.

Now, consider the case of spin injection from a ferromagnetic material into a non-magnetic one [19]. The spins in the FM are polarized and, when a current is established, polarized carriers are injected into the non-magnetic material, inducing a magnetization, δM, as shown in figure 1.1. δM is the stationary magnetization resulting from the balance between spins injected and removed by relaxation processes (fig. 1.1). The spatial extension of the magnetization in the non-magnetic material is linked to the spin diffusion length in that material. The magnetization value in the non-magnetic material depends on the polarization of the injected current, α.

1.1.2 Spin Injection in Semiconductors

Consider now a semiconductor instead of a non-magnetic material. The current injection can be separated into two channels and the two currents model can be applied [18]. The figure 1.2(a) shows the electrical situation

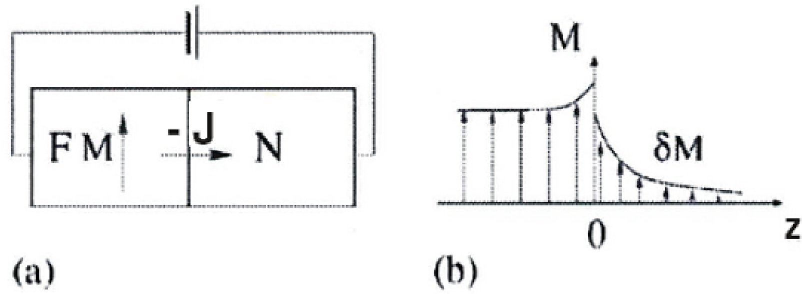

Figure 1.1: (a). Spins injection from a ferromagnet (FM) into a non-magnetic material (N). J is the density of current. (b) Spatial distribution of the magnetization.

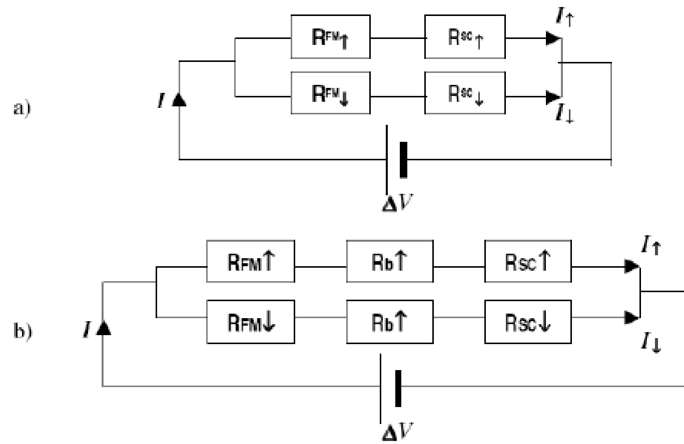

Figure 1.2: Sketch of the electrical situation using the two currents model for (**a**) a FM/SC device or (**b**) a FM/B/SC device.

for a FM/SC junction. Each channel has a total resistance that is the series of the resistance in the FM and the one in the semiconductor. The polarized current can be expressed by:

$$I_{\uparrow,\downarrow} \simeq \frac{\Delta V}{R_{\uparrow,\downarrow}} \tag{1.2}$$

where:

$$R_{\uparrow,\downarrow} = R^{FM}_{\uparrow,\downarrow} + R^{SC}_{\uparrow,\downarrow} \tag{1.3}$$

In semiconductors it is known that $R^{SC}_{\uparrow} = R^{SC}_{\downarrow}$ and that $R^{SC} \gg R^{FM}_{\uparrow,\downarrow}$, therefore:

$$I_{\uparrow,\downarrow} = \frac{\Delta V}{R^{SC}} \Rightarrow \boxed{\alpha = \frac{I_{\uparrow} - I_{\downarrow}}{I_{\uparrow} + I_{\downarrow}} \approx 0} \tag{1.4}$$

The equation 1.4 implies that the semiconductor takes all the potential drop. The resistance for SC is spin-independent, so there is nearly no difference between the two channels and consequently the polarization will be almost zero.

The problem of spins injection in semiconductors had to be solved in order to progress in spintronics techniques. A possible solution was proposed by Rashba [20]: the insertion of a barrier (B) with spin-dependent resistance at the FM/SC interface. This solution exploits the *quantum tunnelling effect*, where a particle tunnels through a barrier that would be classically forbidden.

The conduction is now determined by the density of the states in the FM and SC layers, while the conductivities have smaller effect. This leads to a better efficiency of spin injection in semiconductors [21] because of their large number of empty states available to be filled by electrons coming from the FM metal.

The scheme is represented in fig. 1.2(b). The channels' resistances per unit area of the barrier are $r^B_{\uparrow}$ and $r^B_{\downarrow}$. Therefore, we are introducing an asymmetry of the system with the insertion of two spin-dependent resistances. The asymmetry parameter is called γ and is defined as:

$$\gamma = \frac{r^B_{\uparrow} - r^B_{\downarrow}}{r^B_{\uparrow} + r^B_{\downarrow}} \tag{1.5}$$

The resistance value of the barrier is typically higher than the one of the ferromagnetic layer: $R^B_{\uparrow,\downarrow} \gg R^{FM}_{\uparrow,\downarrow}$. This means that:

$$R_{\uparrow,\downarrow} = R^{FM}_{\uparrow,\downarrow} + R^B_{\uparrow,\downarrow} + R^{SC} \approx R^B_{\uparrow,\downarrow} + R^{SC} \tag{1.6}$$

leading to a current polarization coefficient:

$$\alpha \approx \frac{R^B_{\downarrow} - R^B_{\uparrow}}{2 \cdot R^{SC} + R^B_{\downarrow} + R^B_{\uparrow}} \approx \frac{\gamma}{1 + \frac{2 \cdot R^{SC}}{R^B_{\downarrow} + R^B_{\uparrow}}} \tag{1.7}$$

The polarization has finite value and depends on the asymmetry of the barrier. If $R^B_{\uparrow,\downarrow} \gg R^{SC}$, the α becomes:

$$\alpha \approx \gamma \tag{1.8}$$

The effect of the barrier on spins injection is well described by the *Fert and Jaffrès model* [1]. This allows to obtain the spin polarization of the carriers' population in the semiconductor by calculating $\alpha(z)$, where z is the distance from the barrier. The model exploits the *Boltzmann transport equation* to get the transport properties of the materials. A spin accumulation at the FM/B interface emerges because of the out-of-equilibrium situation. The displacement of the spin populations is described by the splitting of two different electro-chemical potentials: $\mu_{\uparrow}$ and $\mu_{\downarrow}$. The energy distance between them is proportional to the difference of $\uparrow$ and $\downarrow$ populations.

In figure 1.3 different polarization curves are presented. The curve (1) is the polarization for a FM/NM (i.e. Non Magnetic, such as Cu) bilayer. The difference in resistivity between the materials is small, thus the polarization on the non-magnetic side of the interface will be large. The curve (2) represents the case of FM/SC (i.e. the eq. 1.7). The polarization in the semiconductor is almost zero, because its resistance is predominant and spin independent. The last curve (3) shows how the barrier presence changes the polarization in the semiconductor if it is placed between it and the FM.

These results prove that the theoretical limit for spin injection in materials by using a barrier with spin-dependent resistivity is $\alpha = \gamma$ [20]. The question that has to be faced is how to create this barrier. At a

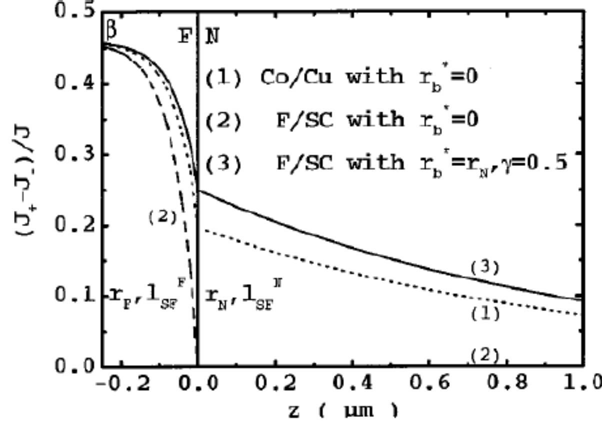

Figure 1.3: Current spin polarization (α) for different interfaces: (1) Co/Cu (FM/NM), (2) Co/SC, (3) Co/B/SC (eq. 1.7) [1].

metal/semiconductor interface a Schottky barrier is typically present. A level of 30% in injection efficiency has been achieved exploiting the Schottky barrier [22]. The problem is that its resistance is usually very large and cannot be easily modified because of the Fermi level's pinning at the interface.

Furthermore, the resistance value can be lowered by high doping level of the semiconductor, but it could form spin flipping centers [23] that reduce the spins' injection efficiency. The best barrier is a very thin layer of insulator between the ferromagnet and the semiconductor. Let's now study the ideal features of a barrier in order to understand the parameters on which a FM/B/SC system should be designed. The polarization at an interface is:

$$\alpha_{interface} \approx \frac{\gamma}{1 + \frac{r_{SC}}{r_B}} \tag{1.9}$$

The equation 1.9 shows that the polarization at the interface is determined by γ and r_B. The optimal conditions are obtained for large r_B and large γ values. A tunnel junction satisfies those properties. For example the aluminium oxide (Al_2O_3) has the values of $r_B = 10^{-10} \div 10^{-4}\Omega m^2$ and $\gamma \approx 0.5$ [24] for injection in Co. The main difference between insulating barriers and Schottky barriers lays in the possibility to tune the $R{*}A$ product within eight orders of magnitude simply by changing the insulator thickness. Another important feature of an interface is the absence of *spin flipping*

events during carriers' crossing into the barrier. In fact, we have assumed a perfect barrier, but the real situation is quite different. Impurities, lattice defects and inter-diffusions cause some spins to invert. The inversion of spins takes majority carriers from the $\uparrow$ channel and transfers them to the $\downarrow$ one. This effect plays against the polarization in the SC and limits the α coefficient. A good interface should have high lattice order and it is fundamental for a high efficiency of injection.

A great innovation in the Spintronics environment was the introduction of MgO as barrier for spin injection [25]. The injection efficiency is granted by its *spin filtering* property of the (100) surface and it gives a polarization up to 50% in Germanium [6]. The spin filtering is given by the bands alignment of MgO. Therefore, the spin injection is largely increased with respect to other insulators.

In this thesis work most devices have been realized with an MgO barrier. It has been grown thanks to Molecular Beam Epitaxy (MBE) technique (see subsection 3.1.2) or magnetron sputtering technique (see section 3.2).

There are other ways to obtain injection, but they are characterized by high energies and are not commonly used in devices. For example, it is possible to inject electrons in ballistic regime into a FM/SC junction. The ballistic conduction is characterized by the absence of scattering events that involve electrons for larger distances with respect to the electron common mean free path. This implies very low resistances. In this way, electrons are injected without modifying their energies.

Otherwise hot carriers can be used: electrons with larger energy than the Fermi level can pass over the barrier. The difference with the tunnelling mechanism is that in this case the conduction occurs over the barrier, while in the precedent case it occurs across the barrier. The spin selection is due to the different mean free path of the two spin channels.

The presence of the barrier for spin injection is not necessary if ferromagnetic semiconductors are used. The problem with this kind of materials is that their critical temperature is up to now lower than room temperature, therefore they are not exploitable for practical applications.

The electric spins detection's conditions are very similar to the ones for

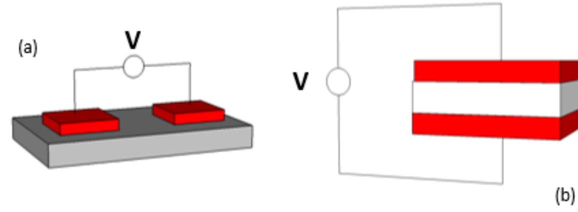

Figure 1.4: Schematic view of (a) the lateral geometry of electrodes and (b) the perpendicular to plane geometry.

an efficient injection. In fact, the spin analyzer will be a ferromagnetic electrode and spin flipping events do not have to occur during the crossing from SC to FM. Even in this case, a magnetic tunnel junction is suggested.

1.2 Spin Transport

In order to operate with spins in semiconductors it is necessary that they keep their polarizations for a finite time (in the range between 10^2 ps and ns). The longer the time, the better the semiconductor will be for spintronics applications.

A spin-polarized carrier in a material can scatter with impurities and defects through spin-orbit interaction. The geometry of devices used in this thesis is called *lateral* (see fig. 1.4(a)): the electrode involved in the injection process lies in same plane as the detecting one. The other possible geometry has the contacts one above the other (back-contact) as shown in fig. 1.4(b).

The parameters for evaluating the transport capability of a material are *spin lifetime* (τ_s) and *diffusion length*)(L_s). The relation between them is $L_s = \sqrt{D_s \tau_s}$, where D_s is the spin diffusion coefficient. The determination of the spin lifetime can be obtained by optical methods or by electric measurements [3]. In this work we will use just electric methods and they will be described in section 1.4.

In a non-magnetic material, the presence of a spin polarization means a non-equilibrium situation. Therefore, the spin population will decrease in

time thanks to *spin relaxation*. It is very important to understand the efficiency of those mechanisms, because it determines the characteristic length and time of a spin current. A material with large value of *spin diffusion length* and large *spin lifetime* is suggested for spintronics applications.

The relaxation event can be interpreted as a result of a variable magnetic field, that originates from different causes. The possible scattering mechanisms are described below.

Elliot-Yafet (EY). Vibrations of the lattice or impurities cause an electric field. The spin-orbit interaction translates the electric field into an effective magnetic field. When the impurities are the origin of the scatter, the number of events is proportional to the impurities' concentration. The effective magnetic field through which the scattering event is interpreted depends on the geometry of the impacts with impurities. Each collision is independent from the others, so the rotations of the spins (ϕ) are not correlated among them. In a III-V semiconductor, the spin relaxation rate for electrons can be expressed by:

$$\frac{1}{\tau_s} = A(\frac{\Delta_{SO}}{E_g + \Delta_{SO}})^2(\frac{E_k}{E_g})\frac{1}{\tau_p} \tag{1.10}$$

where τ_s is the spin relaxation time, τ_p is the time between two scattering events of the electronic momentum, E_g is the bandgap and Δ_{SO} is the valence bands' energetic separation deriving from spin-orbit effect. From eq. 1.10 it is evident that in a material with small gap and large spin-orbit splitting the Elliot-Yafet scattering mechanism has an important influence. This fact has to be taken into account in considering GeTe case.

Dyakonov-Perel (DP). The origin of this scattering mode is the energetic levels' separation induced by spin-orbit interaction into non centrosymmetric materials (such as GaAs, not Si and Ge). The lack of inversion symmetry causes an effective magnetic field that varies with the changing of the momentum direction deriving from a collision. This can be interpreted as a term of the Hamiltonian:

$$\hbar\Omega(\mathbf{p})\mathbf{S} \tag{1.11}$$

The latter equation can be interpreted as the energetic term of a spin $\mathbf{S}$ in an effective magnetic field $\Omega(\mathbf{p})$, where $\Omega(\mathbf{p})$ is a vector depending on the

electrons' momentum orientation. The greatest difference in comparison with the previous case is that the spin rotation does not happen during the collisions, but it is caused by precession between two collisions. In this case, the spin life-time is calculated as:

$$\frac{1}{\tau_s} \approx \Omega^2 \cdot \tau_p \tag{1.12}$$

This mechanism is usually dominant for III-V and II-IV semiconductors as well as for FERSCs that will be treated in sec. 2.3.

Bir-Aronov (BAP). This scattering mechanism is typical for p-type semiconductors. It consists in exchange interaction between electrons' and holes' spins. In this case, the rate is proportional to the holes' concentration. That is why the process is dominant in p-doped semiconductors and should be consider also for Germanium Telluride.

Hyperfine interaction with nuclei spins. Nuclei have a spin and form a disordered lattice in the material. Electronic spins interact with the effective magnetic field generated by nuclei and this interaction is random. For this reason the relaxation rate is usually considered negligible compared with the other events.

Holes' spins relaxation in VB. The relaxation is due to the small energetic splitting between the *heavy holes* band and the *light holes* band. The relaxation time in this case is really short, in fact $\tau_s \approx \tau_p$. It is really difficult to keep a non-equilibrium polarization of spin-polarized holes.

1.3 Spin Manipulation

There are many ways to manipulate the spin in semiconductors. In this thesis we will speak about two of them: *Larmor precession* and *spin Hall effect*.

Here we give a brief outlook about their main features.

Larmor precession An external magnetic field exerts a torque on the magnetic moments of electrons (or holes). This torque is

$$\mathbf{\Gamma} = \boldsymbol{\mu} \times \mathbf{B} = \gamma \mathbf{J} \times \mathbf{B} \tag{1.13}$$

where $\boldsymbol{\mu}$ is the magnetic dipole moment, $\mathbf{B}$ is the external magnetic field, $\mathbf{J}$ is the angular momentum vector and γ is the *gyromagnetic ratio* that represents the proportionality coefficient between the magnetic moment and the angular momentum.

The equation 1.13 defines the motion of the angular momentum in a magnetic field. The result is that $\mathbf{J}$ precesses around the field axis with angular frequency [26]

$$\omega = -\gamma B = \frac{egB}{2m} \tag{1.14}$$

where ω is the *Larmor frequency*, the gyromagnetic ratio has been expressed by $-\frac{eg}{2m}$, e and m are respectively mass and charge of the particle and g is the g-factor.

Spin Hall effect The Spin Hall effect (SHE) will be thoroughly treated in section 2.4. Here we are going to deal with the possibility to exploit the effect in order to manipulate spin.

The effect induces a spin accumulation on the lateral surfaces of a sample crossed by a current. The physical basis of SHE is the *spin-orbit coupling* (SOC) [11].

The manipulation of spins can be performed by changing the spin-orbit interaction locally in the material, for example thanks to strain in particular materials [27]. A similar process exploits the extrinsic mechanism that induces SHE.

Otherwise, in the case of Germanium Telluride the SOC should be modified by the application of a voltage (as described in sec. 2.3), allowing the control of the spin-orbit interaction.

In figure 1.5 the spin Hall effect transistor by Wurderlich et al. [2] is presented. It consists in a Hall bar in which a spin polarized current is induced by the illumination with a circular polarized light. The current

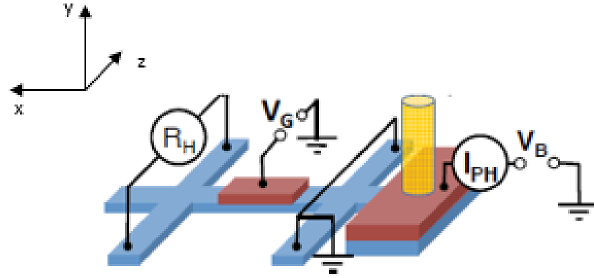

Figure 1.5: Schematic view of the spin Hall effect transistor designed by Wunderlich et al. [2]. The basic idea is that a circular polarized light hits the sample, inducing a spin population in the Hall bar. The gate voltage V_G is capable of controlling the precession of the spins and changing the R_H value.

(along x direction) is splitted in the z direction (if the spin current has a non-zero spin polarization along the y direction) depending on the spin ('up' or 'down') through SHE. The gate voltage generates an effective magnetic field along z thanks to the spin-orbit coupling in the material. The magnetic field causes the spins to precede and modifies the Hall resistance (represented by $R_H = V_H/I_{PH}$) measured orthogonally to the Hall bar. A more precise explanation will be provided in section 2.4.

1.4 Spin Lifetime Measurements

In spintronics the coherence of a spin current in a semiconductor is fundamental. This fact implies that the time interval between two scattering events (each of them causing the spin flipping) should be as high as possible. The parameter expressing this material's feature is called *spin relaxation time*. In the last few years, semiconductor Spintronics research has focused its attention on the identification of the best materials and, in doing this, has developed many experimental techniques capable of deducing spin lifetime. Optical methods are able to excite spin polarized electrons in semiconductors and to evaluate their spin lifetime. Here we will instead talk about pure electric investigations. There are mainly two methods to deduce the spin lifetime: the *four terminals* and the *three terminals* geometries of contacts. In both cases, the relation between a measured quantity and the

spin lifetime can be measured by the *Hanle effect*, a physical phenomenon that will be described in the following paragraph (1.4.1). The two different options will also be analyzed and treated in detail.

Furthermore, a four terminals geometry allows to determine the spin lifetime through a *non-local resistance* measurement. This argument is exposed in the subsection 1.4.4.

1.4.1 Hanle Effect

Let's now consider a tunnelling structure composed by a ferromagnet with in-plane magnetization, an oxide (generally MgO) and a semiconductor substrate. As previously seen, a barrier ensures a high degree of spins injection in semiconductors. What will be the effect on spins population of a magnetic field applied in the out-of-plane direction? To answer this question we should consider the Larmor precession. The electron's spin interacts with a magnetic field resulting in a gyroscopic motion of the spin. Therefore, there are many conflicting effects in determining the spins population: injection (sec. 1.1), precession, relaxation (sec. 1.2) and diffusion.

To express a concentration of electrons, in bands theory the *electrochemical potential* (μ) is used and corresponds to the Fermi energy at $0K$. In fact, its energetic distance from the conduction band of a semiconductor is related to the number of carriers. In the two channels model (section 1.1) the carriers are in a quasi-equilibrium state: the two channels do not interact in a brief time interval, thus they can refer to two different electrochemical potentials: $\mu_\uparrow$ and $\mu_\downarrow$. Therefore, spins polarization in a semiconductor can be expressed by the difference between the spin electrochemical potentials $\Delta\mu$. The effect of an out-of-plane field can be described by a Lorentzian line-shape:

$$\Delta\mu(B) = \frac{\Delta\mu(0)}{1 + (\omega_L \cdot \tau_s)^2} \tag{1.15}$$

where τ_s is the spin lifetime and ω_L is the Larmor frequency. The expression 1.15 is valid just in the absence of diffusion or drift. As we will see, in our case drift is negligible. On the contrary, diffusion should be considered.

The spins injected into the semiconductor diffuse away from the point of

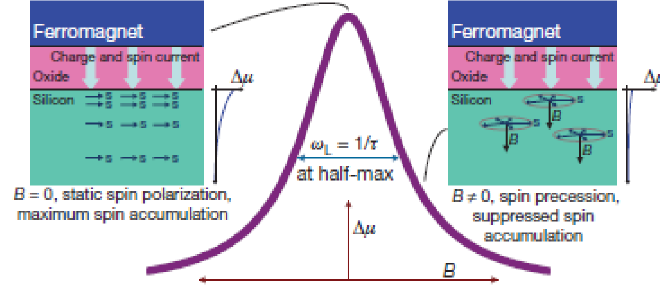

Figure 1.6: Schematic view of the Hanle effect with and without an out-of-plane magnetic field. The connection between the Lorentzian line-shape and the spin lifetime is evidenced. Figure from ref. [3].

injection and often this situation is described by a one-dimensional diffusion model. It has been shown that a fitting that considers this model is better than the Lorentzian one (eq. 1.15) only for high magnetic fields, otherwise they are almost the same ([3]).

The splitting of electrochemical potentials has been said to be the proof of the Hanle effect presence. The problem is the measuring of this splitting: there is the need to link this feature to a measurable quantity. The polarization of spins populations into a semiconductor causes the majorities carriers' electrochemical potential to increase. The increasing of an electrochemical potential level is related to an applied electric bias. In fact, the voltage difference between two points of the SC with different chemical potentials can be expressed as:

$$\Delta V = \gamma \frac{\Delta \mu}{2e} \tag{1.16}$$

where γ is the tunneling spin polarization of the multilayers structure. So it is possible to understand the $\mu_\uparrow$ energetic position in a point with respect to the energetic position in another one just measuring the voltage difference. The experimental procedures to obtain this result are mainly two and they are going to be treated in the following paragraphs.

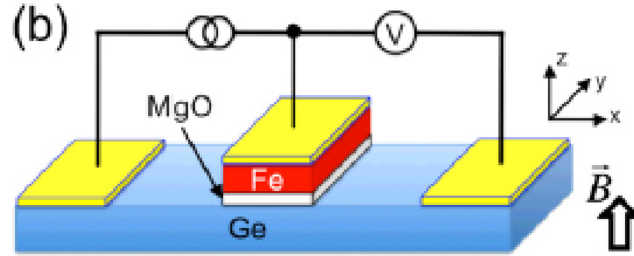

Figure 1.7: Sketch of the three terminals geometry used for spin lifetime measurements in Germanium by Hanbicki et al. [4].

1.4.2 Three Terminals Geometry

The fig. 1.7 shows the three terminals geometry for spin lifetime measurements. In the figure, the central electrode is the only magnetic tunnelling junction because it is the only structure in the geometry that needs to inject/detect spins. A spin current is generated between this electrode and another one, thanks to the ferromagnetic upper layer. The other electrode has the function of reference for the measured voltage, since in that position there is no spin polarization, so the electrochemical potentials $\mu_\uparrow$ and $\mu_\downarrow$ are degenerate. The central electrode has to inject and to detect spins at the same time. Even if the Lorentzian line-shape was said to be a good fit for the Hanle effect, we can now consider the diffusion in order to develop a better physical model. The spins injected at the interface between semiconductor and barrier diffuse away in the three directions. Their number decays with increasing distance, with a *spin diffusion length* (L_{SD}). In a time interval the spins injected diffuse under the electrode and suffer the precession caused by the magnetic field. The measured voltage is function of the whole spin population under the central electrode and even of the diffused carriers.

The main problem with three electrodes geometry is the roughness of the surface. If the spin lifetime in the bulk is looked for, the roughness of a surface can be regarded as not determinant. However, a rough surface causes an inhomogeneous magnetic field that modifies the spin polarization in the semiconductor, as shown in figure 1.8.

Therefore, the spin lifetime is underestimated with respect to the expected one. However, the result is correct just in the proximity of the

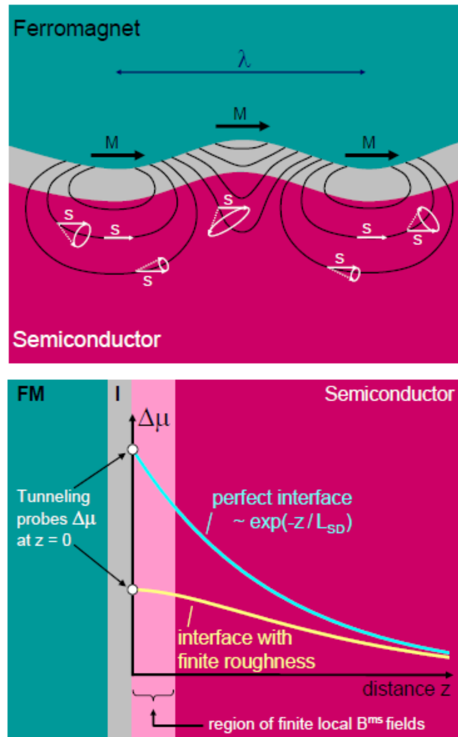

Figure 1.8: (**a**)Inhomogeneous magnetic field caused by a sinusoidal roughness profile with wavelength λ. The precession of spins due to interaction with the field is represented and modifies the original in-plane magnetization of the injected spins. (**b**)Trend of $\Delta\mu$ spin accumulation for a rough interface compared to a perfect one. The decreasing due to a rough interface is evident. See ref. [5]

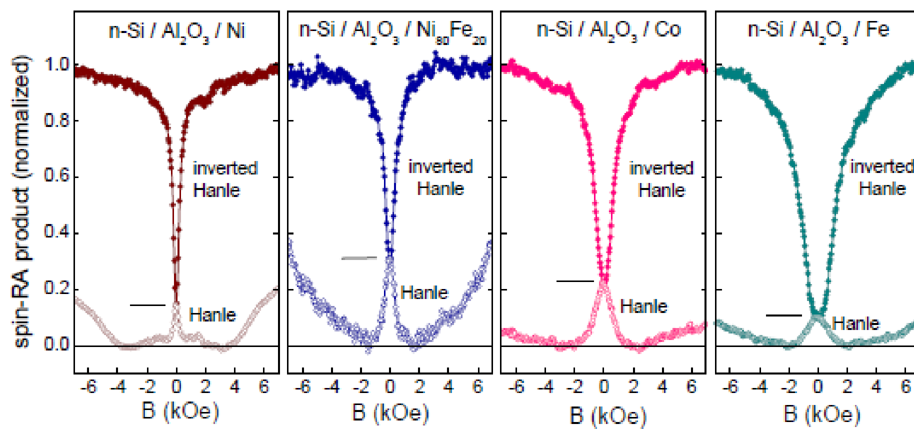

Figure 1.9: Inverted Hanle and Hanle signals for different surfaces [5].

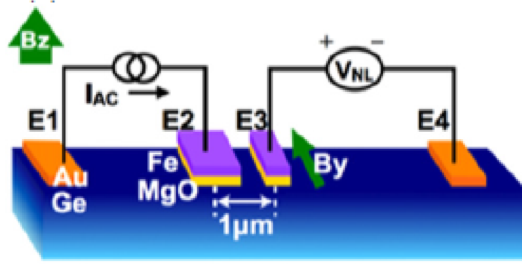

Figure 1.10: Scheme of the four terminals geometry for non-local spin lifetime measurements on Germanium. The figure is taken from Chang et al. [6].

interface and it is not compatible with the lifetime in the bulk of the semiconductor. The intensity of this effect is evaluated by the *inverted Hanle effect* that is experimentally performed as Hanle measurement but with an in-plane applied field. The physical concept is simple: suppose that the external field is zero, thus the spins precess with the axis determined by the local magnetostatic field, causing the spin polarization to decrease. If an in-plane magnetic field is present, then the total field will be $B^{ext} + B^{ms}$. The external field is in the direction of magnetization and suppresses the precession. For large values of magnetic field, the spin polarization in the semiconductor is maximized. In figure 1.9 inverted Hanle signal and Hanle signal are presented for different interfaces.

The set-up exploited for three terminals Hanle measurements is presented in section 3.8.

1.4.3 Four Terminals Geometry

The four terminals geometry is presented in figure 1.10. Here the electrodes involved in injection and detection of spins are two: the central ones. Therefore, they are multilayered structures with tunnel junctions.

The mechanism of the Hanle effect in this case is not straightforward and the measurement is called *non local*. Spins are injected through the application of a current between one reference electrode and a central one; then a voltage is measured between the remaining electrodes. This implies that the spin polarization taken into account is the one under the second central electrode. In fact, the spins population has to travel from the injec-

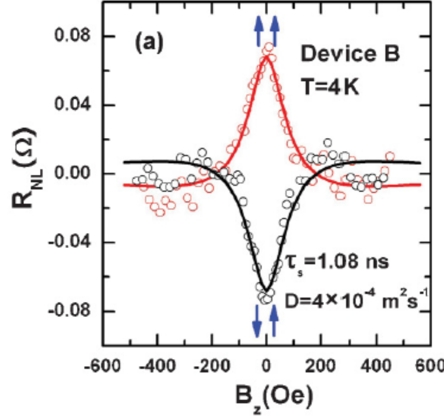

Figure 1.11: Non local resistance measured in slightly n-doped Germanium by Zhou et al. (ref. [7]):1-D diffusion model fittings for parallel and anti-parallel orientations of the electrodes' magnetizations.

tion contact to the detection one through the diffusion transport. Diffusion has to be integrated into the Hanle effect model: a *one dimensional spin diffusion model* is usually adopted to fit the measured curve, as shown by Zhou et al. [7]. It is possible to measure a non local resistance (defined as the non local voltage V_{NL} divided by the ac modulation current I_{ac}, see fig. 1.10):

$$R_{NL} \propto \pm \int_0^\infty \frac{1}{\sqrt{4\pi Dt}} exp[-\frac{L^2}{4Dt}] \cos(\omega_L t) exp(-\frac{t}{\tau_s}) dt \tag{1.17}$$

where D is the diffusion constant, τ_s is the spin lifetime and $\omega_L = g\mu_B B_z/\hbar$ is the Larmor frequency. The sign of the non local resistance depends on the relative magnetizations between the injection and detection electrodes: + for parallel, − for anti-parallel magnetizations.

An example of the measured curve is shown in fig. 1.11.

1.4.4 Non-Local Resistance

Consider the four terminals geometry in figure 1.10. The measurement's set up is the same as the Hanle effect in four terminals geometry, except for the external magnetic field direction. In fact, this time the field is B_y in fig. 1.10 instead of B_z.

The physical concept of spin diffusion has already been presented in subsection 1.4.3. The spin diffusion current can be expressed by [28]:

$$I_s = I_s(0)exp(-x/L_s) \tag{1.18}$$

where $I_s(0)$ is the current injected at the E2 central electrode (see fig. 1.10), L_s is the spin diffusion length and x is the distance between the central electrodes. The expression of the current at the E2 electrode is $I_s(0) = (1/2)P_sI$, where P_s is the effective polarization of the FM above E2 and the factor 1/2 is a consequence of the isotropic spin diffusion in the non-magnetic material.

The non-local voltage (V_{NL}) is connected with the difference of chemical potentials under the contacts E3 and E4. The non-local output resistance is

$$R_{NL} = \pm\frac{1}{2}P_S P_D R_S \exp^{-x_D/L_S} \tag{1.19}$$

where P_D and x_D are respectively the polarization and the distance from the injection electrode of the detection electrode and $R_S = L_S/\sigma A$ is the spin resistance of the non-magnetic material. The (+) and (−) signs correspond to parallel and anti-parallel configurations of the E2 and E3 magnetizations.

If many structures like the one in fig. 1.10 are fabricated with different x_D, information on P_s, P_D and L_S can be deduce from the measured R_{NL}.

The E2 and E3 electrodes have different geometries. This implies that the electrodes have different magnetic shape anisotropy, therefore their coercive fields differ.

The sweep of the in-plane magnetic field causes the change in the relative alignment of E2 and E3 (for example from parallel to anti-parallel) and therefore the change in the non local resistance, as shown in fig. 1.12.

By changing the distance between the central electrodes it is possible to obtain the trend of ΔR_{NL}. This is an exponential decay with characteristic length equal to the spin diffusion length, from which the spin diffusion time can be deduced ($L_S = \sqrt{D\tau_S}$).

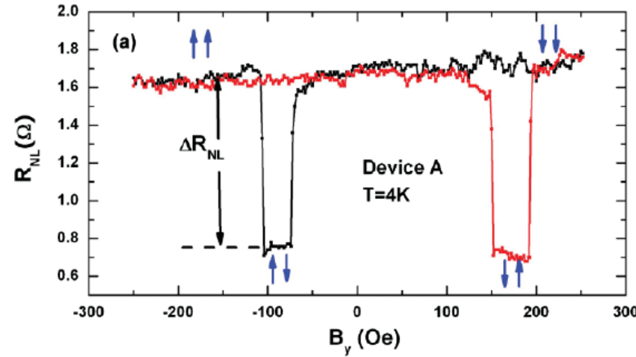

Figure 1.12: Non local resistance measured at 4 K in a four terminals device by Zhou et al. [7]. The blue arrows indicate the magnetization orientations.

1.5 Classical Spintronics Devices

During Spintronics history, a lot of devices have been developed and have got application in industries. The first and maybe the most important effect is the *Giant Magneto-Resistance* (GMR) [8] discovered by Albert Fert and Peter Grünberg in 1988; in 2007 the two scientists won the Nobel prize for physics. Until then, only the anisotropic magneto-resistance (AMR) was known: it consists in a resistivity's change in a magnetic layer due to a rotation of the magnetization direction.

Fert saw a 50% change with magnetic field in the electrical resistance of a multilayer structure of Fe/Cr [8]. It was an amazing value if compared to the 3% of AMR. Fert and Grünberg realized they were observing a completely new kind of effect.

Another effect that changes the Spintronics' history is the *Tunnel Magneto-Resistance* (TMR). This mechanism has been known since 1975 [29] but its application in devices is recent (2004 [30]). More details about its history and properties are described in the TMR paragraph.

GMR The understanding of this phenomenon can be reached by considering the carriers' spin-dependent scattering with the magnetic sub-lattice of the crystal. In fact the carriers' scattering rate depends on the relative orientation of the spin with respect to the ferromagnetic magnetization: it is weaker for a parallel orientation, and it is stronger for an anti-parallel

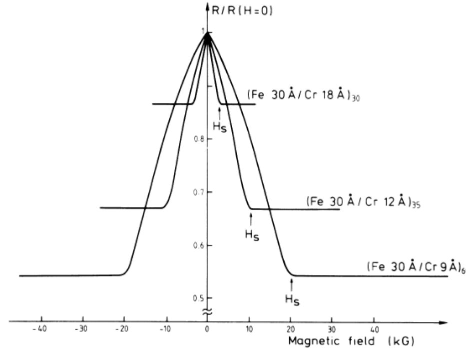

Figure 1.13: Resistance (with respect to zero-field value) of three Fe/Cr superlattices with different non-magnetic thicknesses at 4.2 K. Current and applied field are in the same plane of the layers [8]

orientation. This means that the resistance value will be higher for minority carriers, i.e. the particles with spin orientation opposite with respect to the layer magnetization.

The effect is maximized if a non-magnetic layer is sandwiched between two ferromagnetic ones. This can be done in two configurations, depending on how the current flows: in-plane or out-of-plane. The different structures are called CIP (Current-In-Plane) or CPP (Current-Perpendicular-to-Plane). The understanding of the phenomenon is reachable using the *two channels model* that is described in section 1.1.

The complete treatment is called *Valet-Fert model*: in 1993 Albert Fert and Thierry Valet explained the giant magneto-resistance starting from the Boltzmann equation of diffusion [31].

The intensity of the effect can be expressed as

$$GMR = \frac{R(0) - R(H_s)}{R(0)} \tag{1.20}$$

where H_s is the saturating field capable of aligning the two layers' magnetizations and reducing the resistance.

The fig. 1.14 illustrates the application of GMR effect in a spin-valve. At zero magnetic field, the orientation between the layers' magnetizations is anti-parallel, meaning a high value of resistance ($R(0)$ in eq. 1.20). When

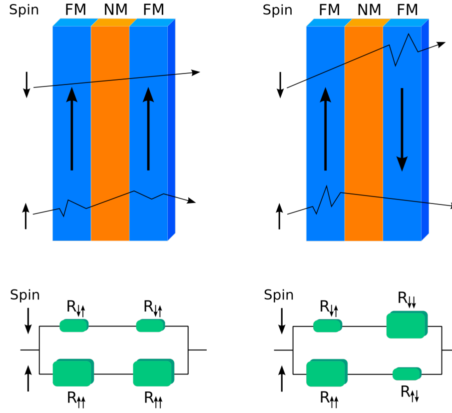

Figure 1.14: Spin-valve based on the GMR effect. The left image represents the case of applied field (H_s in eq. 1.20); the right one is the case without applied field.

the magnetic field is increased to the saturation value (H_s), the relative orientation becomes parallel and the resistance turn to low value ($R(H_s)$).

In this way, a device in which the switching of the resistance is consequence of an applied magnetic field has been realized.

TMR When the non-magnetic layer is an insulator, the *Tunnel Magneto-Resistance* (TMR) effect occurs. The structures in which this effect arises are called *Magnetic Tunnel Junctions* (MTJs): they are composed by two FM layers separated by an insulating one.

The TMR value is defined as:

$$TMR = \frac{R_{ap} - R_p}{R_p} \tag{1.21}$$

where R_{ap} is the electrical resistance in case of anti-parallel alignment for the ferromagnets' magnetizations and R_p for parallel magnetizations.

Since its discovery (by Julliere in 1975 [29]), it has not attracted much attention because of the limited change in resistance (only 14%). Great enhancement of its performances was predicted with the use of MgO as insulating barrier by Butler et al. in 2001 [32] and it was experimentally observed by Bowen et al. in the same year [33]. In 2008 Ikeda et al. realized CoFeB/MgO junctions capable of reaching over 600% TMR at room

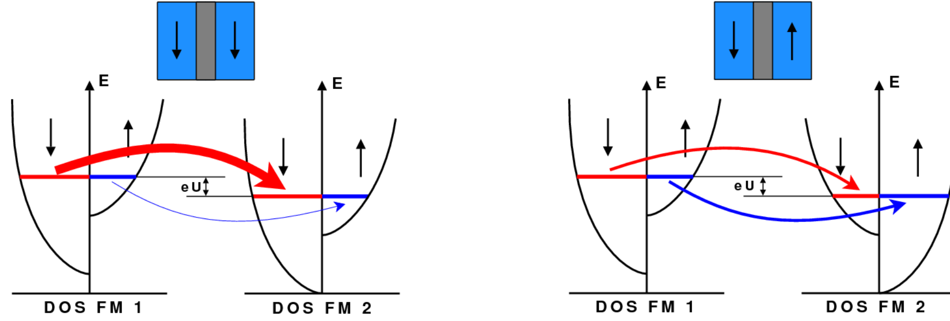

Figure 1.15: Two-currents model applied to the TMR case. The resistance of the parallel case is smaller than the anti-parallel case because the DOS in the first ferromagnet granted a large number of electrons and the second FM has a large availability of states.

temperature [34].

The physical explanation of the TMR effect was given by Julliere [29] through the analysis of the FM layers' spin polarizations. The scheme in figure 1.15 shows the working principle.

The polarization can be expressed as

$$P = \frac{D_{\uparrow}(E_F) - D_{\downarrow}(E_F)}{D_{\uparrow}(E_F) + D_{\downarrow}(E_F)} \tag{1.22}$$

where D is the density of states and the convention has been followed according to which $\uparrow$ represents the spins with parallel orientation with respect to the external magnetic field, while $\downarrow$ means spins with anti-parallel alignment. Taking into account the spin polarizations P_1 and P_2 of the two ferromagnetic layers and assuming that the spin does not vary during tunneling, the *two-currents model* can be employed (for further information, see section 1.1) and the TMR can be expressed as

$$TMR = \frac{2P_1P_2}{1 - P_1P_2} \tag{1.23}$$

GMR and TMR applications The main application of GMR and TMR is the *spin-valve*, exploitable both as sensor and as memory element.

A spin-valve sensor is composed by a free ferromagnetic layer, a non-

magnetic layer and a pinned FM layer. The pinning of the latter is usually realized by *exchange bias*, a coupling between a ferromagnetic layer and an anti-ferromagnetic one, that induces an asymmetric shift of the FM hysteresis loop.

A magnetic field interacts with the free ferromagnetic layer and is capable of turning its magnetization without compromising the pinned layer's one. Therefore, the field can modify the relative orientation of the layers' magnetizations and change the resistance of the structure. The reading procedure of the sensor is simply performed by the resistance measuring.

The sensor is implemented in hard disks technology. In fact, in hard disk drives there are many opposite magnetic domains, each of them associated with one bit (0 or 1) of information. In correspondence with the transition regions (*domain walls*) the magnetic field exits the material. The direction of the field, detectable with a spin-valve sensor, gives the relative orientations of the domains.

Another application of the GMR concept is the *Magnetoresistive Random-Access Memory* (MRAM). The difference with respect to the conventional RAM is that the basic memory element is magnetic instead of an electric charge. The spin-valve is the element of the memory instead of a field-effect transistor.

The reading procedure is simply a resistance measurement: the anti-parallel/parallel configuration has a high/low resistivity. One of these has the logical meaning of $'1'$ and the other of $'0'$.

The writing action is performed by the flow of a current in two write lines. The current induces a magnetic field that is able to change the magnetization of one magnetic layer, therefore it is tuning the spin-valve state.

The problem concerning the induced field's writing technique is that it is difficult to limit the magnetic field effect on just one bit when the miniaturization takes place. In fact, the magnetic field is a long range field that decreases as $1/r^2$, therefore it is hard to localize the field's effect on just one memory element.

The new procedure exploits the *spin transfer torque* (STT): spin-polarized electrons are injected into the FM layer developing a torque on the magnetic momenta [9]. The interaction originates from the angular momentum exchange among the electrons injected by the MTJ and the electrons present

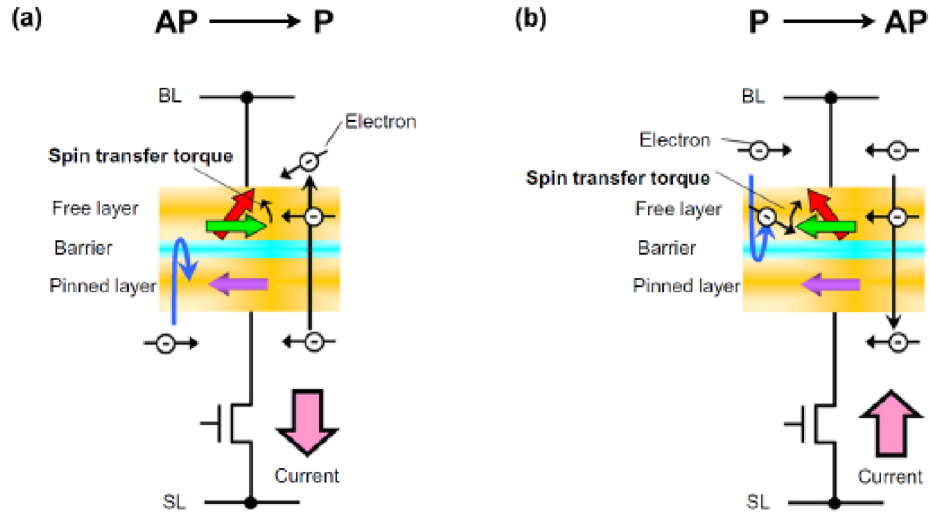

Figure 1.16: STT switching processes: from anti-parallel (AP) to parallel (P) (**a**) and from P to AP (**b**) [9].

in the layer. We need to distinguish the two writing phases: the switch of the free layer from anti-parallel (AP) to parallel (P) with respect to the pinned layer's magnetization and the opposite transition. In doing this, we refer to fig. 1.16.

In the AP/P switching, the electrons should flow from the pinned layer to the free one, as shown in fig. 1.16a. The current is spin-polarized and is injected into the free layer. When the injected spins reach a threshold value, the magnetization of the free layer is switched.

The P/AP switching (fig. 1.16b) is performed when the current passes from the free layer to the pinned one. Even this current is polarized and the majority spins easily flow towards the pinned layer. The minority spins, instead of passing through the barrier, are reflected and return into the free layer. This spin-polarized current exerts a STT on the free layer magnetization and, once a threshold level is reached, is able to switch it.

The main advantage of MRAM with respect to standard RAM is its non-volatility. Unfortunately, its working needs high current densities to achieve the STT effect and the power absorption is nowadays quite high.

One of the most promising application in Spintronics is the *spinFET*. It

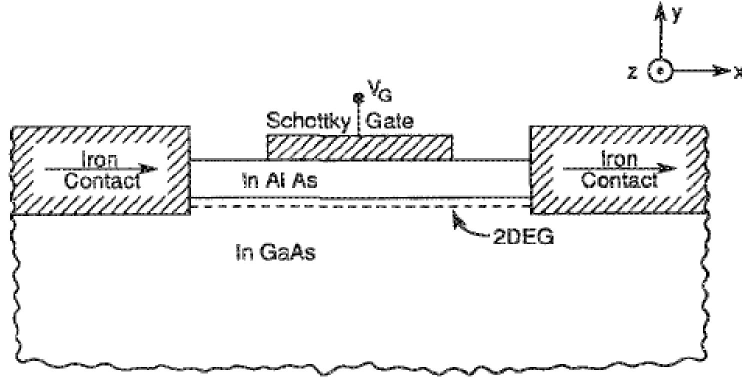

Figure 1.17: The original Datta and Das concept of the spin-FET

realizes the implementation of the spin functionalities in the basic logical element for the electronics, the Field-Effect Transistor. A working device has not been reached yet, but in sec. 2.5 a solution will be proposed.

1.5.1 The Datta and Das SpinFET

The *spinFET* (i.e. spin Field Effect Transistor) was proposed by Datta and Das in 1990 [35] and consists in a modified transistor capable of exploiting the magnetic properties of carriers. The innovative idea of Datta and Das was to create an electronic analog of the electro-optic modulator.

An electro-optic modulator is a device that is used to modulate the light intensity transmitted through a material by rotating the polarization of the incident light, depending on the value of the electric field applied through a gate. The incident linearly polarized light is rotated in the crystal and analyzed by using a linear polarizer (analyser) after the rotation.

The concept of the spinFET is based on this structure and it is shown in figure 1.17.

The basic spinFET's operation is the injection of spins from a FM electrode into a semiconducting channel (its features will be presented in the following) where precession occurs and, finally, the detection by another FM electrode. The low/high resistance state depends on the relative orientation between the carrier's magnetic moment (μ_s) and the magnetization of the detecting electrode.

The injection and detection of spins are obtained with two ferromagnetic

electrodes. The channel of the transistor must have a spin splitting of energetic levels (in order to favour the transport of one spin population) and a narrow gap (for lower resistivity). In the original concept the material was a 2DEG (*2 D Electron Gas*) because it presents a spin splitting without any magnetic field. Inversion asymmetry contributes to the zero-field spin splitting. If an electric field perpendicular to the plane (y direction) is present, in the effective mass Hamiltonian of the material there will be a *Rashba* term corresponding to eq. 2.5. Another way to express the interaction term in our specific case is:

$$H_R = \eta(\sigma_z k_x - \sigma_x k_z) \tag{1.24}$$

where η is a coefficient linked to α (eq. 2.6).

Since in thin films the carriers are flowing along x but not along z, the Rashba Hamiltonian in eq. 1.24 can be simplified as

$$H_R = \eta \sigma_z k_x \tag{1.25}$$

Let's assume the injection of spins in the negative x-direction, as shown in fig. 1.17. The spins can be expressed by the eigenvalue (*spinor*):

$$|\downarrow>_x = \begin{pmatrix} 1 \\ -1 \end{pmatrix} = \begin{pmatrix} 1 \\ 0 \end{pmatrix} - \begin{pmatrix} 0 \\ 1 \end{pmatrix} = |\uparrow>_z - |\downarrow>_z$$

Therefore, we are expressing the x-polarized spin through a linear combination of positive and negative z-polarized electrons.

The two spin components propagate with different wave-vectors since their energies are split in according with the spins' projection along the Rashba field direction. The energy levels can be expressed as:

$$E_{+zpol} = \frac{\hbar^2 k_{x1}^2}{2m^*} - \eta k_{x1} \tag{1.26a}$$

$$E_{-zpol} = \frac{\hbar^2 k_{x2}^2}{2m^*} + \eta k_{x2} \tag{1.26b}$$

Having two different wave-vectors (k_{x1} and k_{x2}), two electrons with opposite spins accumulate a phase difference along the channel (obtained by considering $E_{+zpol} = E_{-zpol}$):

$$\Delta\theta = (k_{x1} - k_{x2})L = 2m^*\eta L/\hbar^2 \tag{1.27}$$

where L is the channel's length.

The parameter η is the spin-orbit coupling coefficient and depends on the external electric field. This means that the gate voltage V_g is capable of modulating the phase difference and hence the transmission of the channel. Materials with η value large enough to introduce significant phase shift are good candidates for a spin-FET application.

The detecting electrode has an in-plane magnetization (see fig. 1.17), therefore the transmission of the spin current is determined by the projection along the x direction of the spins at the end of the channel. The final spin state is:

$$e^{ik_{x1}x}\begin{pmatrix}1\\0\end{pmatrix} + e^{ik_{x2}x}\begin{pmatrix}0\\-1\end{pmatrix} = e^{ik_{x2}x}\begin{pmatrix}e^{i\Delta\theta}\\-1\end{pmatrix}$$

Therefore, when $\Delta\theta = 2k\pi$ (where k is an integer number), the spin projection along x will be $|\downarrow>_x$ and the system will be in the high transmission (low resistance) state. On the contrary, if $\Delta\theta = (2k+1)\pi$, the spin projection will be $|\uparrow>_x$ and the system will be in the low transmission (high resistance) state.

Chapter 2

Spin-Orbitronics

2.1 Introduction

The framework presented in the previous chapter draws the state of the art in semiconductors Spintronics. Ferromagnetic materials are the fundamental elements in a spintronic device, but they have limits. In fact, magnetic stray fields do not permit high density integration and often metals are not suitable for the growth on semiconductors.

One way to avoid the inclusion of FM metals into devices (keeping the spin functionality) is to put ferromagnetic impurities within the semiconductor lattice. Diluted magnetic semiconductors have been studied in the past decades but it is quite accepted that they can operate only below RT (since a significant magnetic exchange energy implies a vary small band gap [36] [37]), therefore their implementation in devices is unimaginable.

The classical Spintronics is based on the *Mott paradigm*, according to which the logical function is implemented into the relative orientation of FM layers, would no longer be valid. In fact, in the *two currents model* framework the resistance depends on the layers' magnetizations relative orientations.

An innovative task would be achieved by the generation, manipulation and detection of spin population within a single, not FM semiconducting material. In doing this, there are two main possibilities. An interesting approach to both the spin and the SC functionality has been proposed and investigated by Jungwirth *et al.* [38]: since in magnetic ordered materials the spin-orbit effects depend on m^2 instead of m (where m is the magnetic

momentum of the single atomic site), it is possible to use *antiferromagnetic* (AFM) semiconductors as base materials for Spintronics applications.

In this work we discuss an alternative approach exploiting not FM or AFM materials, but just the spin-dependent effects generated by *spin orbit interaction* in a novel class of materials. This event would mean a fundamental change in the basis of Spintronics. The study of the spin orbit interaction and its possible applications was called *Spin Orbitronics* by Albert Fert, Nobel Prize for Physics in 2007.

S. Picozzi et al. [39] recently proposed a new class of materials: the FerroElectric Rashba SemiConductors (FERSCs) (see sec. 2.3). Because of the lack of inversion symmetry in these materials, spin-orbit coupling (SOC) can cause the *Rashba effect* (see sec. 2.2). The effect consists in the k-dependent spin splitting of the bands in some regions of the reciprocal space. FERSCs are very promising because they present an interesting coupling between ferroelectricity and bulk Rashba effect: a reversal in the ferroelectric polarization causes the spin directions in each sub-band to reverse, allowing electrical non-volatile control.

In this thesis we will study *Germanium Telluride* (GeTe), a very well known material (with the addition of Sb) in the context of phase change memories, but just now discovered to belong to FERSC class of materials [13]. The argument will be treated in detail in section 2.3.

The implementation of these new materials in devices should require different approaches with respect to classical Mott Spintronics. The section 2.4 will be dedicated to the *Spin Hall Effect* because it grants the spin manipulation that will be exploited in the devices' operation. In sec. 1.5.1 three novel spintronic concepts of device will be presented and described. They have in common the presence of a gate: this electrical contact permits the switching of ferroelectric polarization and the consequent spin texture inversion.

Another innovation linked to the FERSCs implementation is the possibility of a *totally semiconductors-based Spintronics.* In fact, the complete electrical control of the spin population in the material permits to avoid the implementation of FMs. A concept device will be treated in sec. 1.5.1.

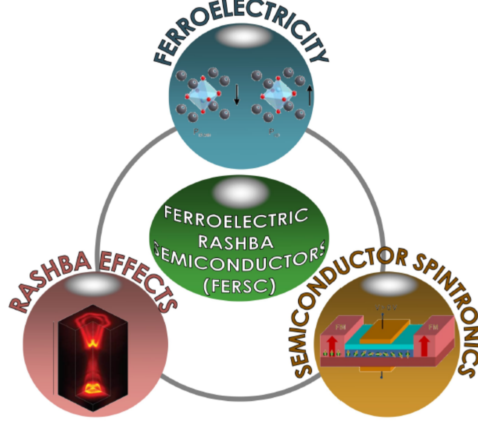

Figure 2.1: Sketch representing all the effects and technology that are merged together in FerroElectric Rashba SemiConductors [10].

2.2 Anatomy of the Rashba Effect

The Rashba effect is a main character in the Spin Orbitronics framework. It is a momentum-dependent splitting of spin bands, originating from a symmetry's break of the system (such as two-dimensional systems).

The effect can be taken into account adding a Rashba term to the system Hamiltonian. This Rashba Hamiltonian can be calculated in a phenomenological way introducing a effective electric field written as

$$\mathbf{E} = E_0 \hat{z} \tag{2.1}$$

that gives the break of symmetry along the $\hat{z}$ direction.

It is possible to consider this electric field as an effective magnetic field through the relation

$$\mathbf{B} = \frac{1}{c^2}(\mathbf{v} \times \mathbf{E}) \tag{2.2}$$

where c is the speed of light in vacuum, $\mathbf{v}$ is the speed of the particle and $\mathbf{E}$ is the electric field. The potential energy (Zeeman term) of a particle with magnetic moment μ within the effective magnetic field B is:

$$H_{SO} = -\boldsymbol{\mu} \cdot \mathbf{B} = \frac{g\mu_B}{2c^2}(\mathbf{v} \times \mathbf{E}) \cdot \boldsymbol{\sigma} \tag{2.3}$$

where $\mathbf{p}$ is the particle's momentum, $\boldsymbol{\sigma}$ is the Pauli matrix vector and the

magnetic momentum of the electron μ equals to $-g\mu_B\boldsymbol{\sigma}/2$ (μ_B is the Bohr magneton and g is the *g-factor* of the electron). Considering the relation $\mathbf{p} = m\mathbf{v}$ between the particle's momentum p and the particle's velocity v (where m is the effective mass particle) and eq. 2.1 for the effective electric field $\mathbf{E}$, the eq. 2.3 can be expressed as:

$$H_{SO} = \frac{gE_0\mu_B}{2mc^2}(\mathbf{p} \times \hat{z}) \cdot \boldsymbol{\sigma} = \frac{gE_0\mu_B}{2mc^2}(\boldsymbol{\sigma} \times \mathbf{p}) \cdot \hat{z} \tag{2.4}$$

where the invariation under circular shift of the three operands ($\mathbf{p}$, $\hat{z}$ and $\boldsymbol{\sigma}$) in the triple product of vectors has been used.

The physics of the Rashba effect is already contained into eq. 2.4. A complete quantum mechanical treatment based on the $\mathbf{k} \cdot \mathbf{p}$ theory leads to a similar Rashba Hamiltonian with a different and correct multiplicative pre-factor called α_R (*Rashba coefficient*):

$$H_R = \alpha_R(\boldsymbol{\sigma} \times \mathbf{p}) \cdot \hat{z} \tag{2.5}$$

The intensity of the Rashba effect is quantifiable through the α_R coefficient (see section 2.3): the bigger it is, the larger the k-splitting will be. A schematic view of the Rashba splitting is shown in figure 2.2. The Rashba effect strength is also evaluated by analysing the intensity of either one out of the other two following parameters: (i)k_R, i.e. the momentum offset of the band's minimum from the symmetry point; (ii)E_R, i.e. the energy difference between the band's minimum and the symmetry point. The relation among Rashba coefficient and the other parameters is:

$$\alpha_R = \frac{2E_R}{k_R} \tag{2.6}$$

The fascinating feature of Rashba effect has been theoretically presented by Edelstein in 1990 [40]. He reported that a current in a Rashba material is capable to unbalance the spin populations by selecting a particular momentum direction. In fact, the presence of an electric field induces a concentration of more electrons with the wave-vector's sign in accordance with the current. In a Rashba semiconductor the choice of a momentum corresponds to the choice of a spin direction, therefore the result is a polarized current: in GeTe (see sec. 2.3), electrical currents in the proper crystallographic directions are partially spin-polarized, with the possibility

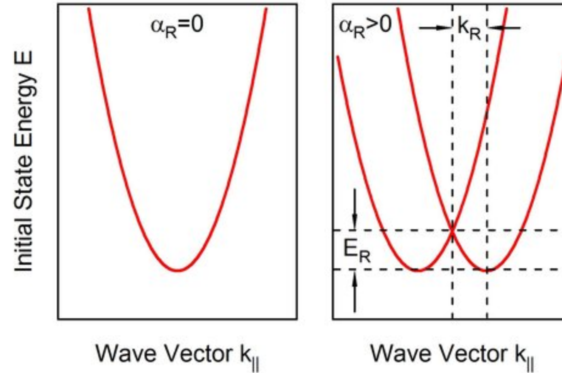

Figure 2.2: Rashba effect. The α_R parameter indicates the intensity of the effect.

to avoid spin injectors and using directly the FERSC as a source, modulator and analyzer of spin-polarized currents (as will be described in sec. 2.5). This phenomenon is called *Edelstein-Rashba effect* and it is one of the main reasons for the particular attention paid to Spin Orbitronics.

The interest in Rashba effect for spintronics lays in the possibility of manipulating the spin without using any magnetic field. For this reason, great attention is focused on those materials on which new kinds of spintronic devices with memory properties can be designed.

2.3 FerroElectric Rashba SemiConductor: GeTe

Recently, D. di Sante, R. Bertacco *et al.* [13] have carried out some theoretical calculations on Germanium Telluride and have deduced a very interesting behaviour.

This material is a semiconductor that theoretically presents a ferroelectric behaviour and a giant bulk Rashba splitting. In order to describe all those features a new class of materials is proposed: FERSC [10]. The abbreviation means *Ferro Electric Rashba Semi Conductors.* The main feature is the coupling between the ferroelectricity and the spin-orbit induced by Rashba effect.

Germanium Telluride is non-centrosymmetric crystal: it stabilizes in a rocksalt structure with the Ge and Te ions slightly displaced form the ideal sites along the (111) direction [13].

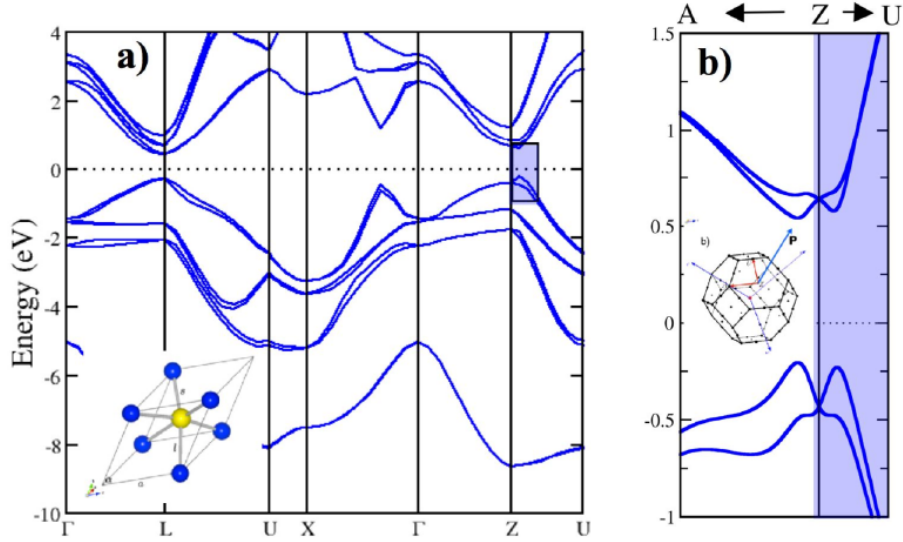

Figure 2.3: Band structure of GeTe (a). The figure (b) shows a magnification around the Z point. The zero of the energy scale is given by the predicted Fermi level.

First principles' simulations on Germanium Telluride via density functional theory (DFT) have shown a giant spin splitting in **k** on the direction perpendicular to the ferroelectric polarization. The bulk Rashba effect derives from the GeTe lack of inversion symmetry. Ge and Te ions displace from their ideal rocksalt along the [111] direction and this causes the ferroelectric behaviour.

A Rashba splitting has been found from calculations and it strength is particularly high aroung the Z point in the reciprocal space, corresponding to the center of the hexagonal face of the first Brillouin zone (fig. 2.3(a)). The panel (b) of fig. 2.3 is a zoom of the band structure around the Z point, for two relevant high symmetry directions ZA and ZU. From this plot, the splitting is evident to be anomalously large for holes around valence band maximum.

The intensity of the k-splitting due to Rashba effect is quantifiable through the eq. 2.6. In Germanium Telluride the calculated k_R value is equal to 0.094 Å^{-1}, E_R is 227 meV and α_R is 4.83 eVÅ for holes. The Rashba coefficient value is enormous if compared to literature. In fact, a

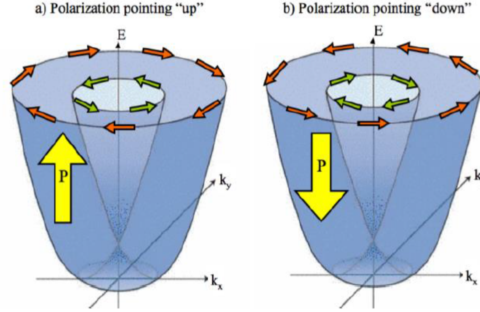

Figure 2.4: The inversion of electric polarization causes the entirely spin texture to flip.

giant bulk Rashba effect has been observed only in bulk *BiTeI* [41], but it has limited features with respect to GeTe. In fact, BiTeI is a very conductive material (because of the high doping level) and has no ferroelectric behaviour, thus the Rashba control must be performed with the application of an electric field.

A really interesting fact is that, by switching the ferroelectric polarization, it is theoretically possible to get a full reversal of spin texture (see fig. 2.4). The switch of ferroelectric state involves the inversion of Ge-Te relative displacement.

The ferroelectric behaviour is associated with the displacement between Ge and Te sublattices that is expressed through the ferroelectric order parameter τ (in lattice parameter's units). The connection between the ferroelectricity and the Rashba splitting is given by fig. 2.5.

This feature permits its implementation in a spin-FET device with *non-volatile channel*, as it will be presented in sec. 2.5.

Germanium Telluride is a test case to develop a proof-of-concept of FERSCs in Spin Orbitronics. The future of this field will consist in the research of new FERSC materials with improved properties. A "perfect" FERSC should have the following features:

- a strong and stable ferroelectric behaviour, in order to have memory properties;

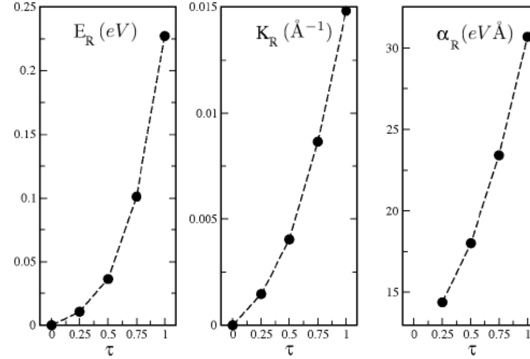

Figure 2.5: Rashba parameters E_R, k_R and α_R as a function of the GeTe ferroelectric order parameter τ.

- a band gap which is large "enough" in order to better control the transport properties of the material;
- a large spin-orbit coupling, that means large Rashba effect.

The band gap of a material plays a crucial role in defining these properties. A small gap implies a larger spin-orbit coupling, but a large gap causes a higher resistivity. In other words, the research of FERSC materials has to find the best compromise on the energy gap extension.

The basic characterization of our GeTe samples is performed through many techniques. The Rashba features will be investigated with spectroscopic methods, such as ARPES (see section 3.4) and spin-resolved ARPES.

The *Hall effect* (as presented in section 3.7) will be used in order to determine the doping level in our samples.

The current spin polarization will be looked for with Spin Hall effect measurements (see sec. 2.4).

2.4 Spin Hall Effect

The Spin Hall effect (SHE) was predicted by Dyakonov and Perel in 1971 [42]. It was named that way by Hirsch in 1999 [11]. The effect consists in the spin accumulation on lateral surfaces in a material in which a longitudinal current is present. The spin polarization is opposite in the two faces and flips when the current is reversed.

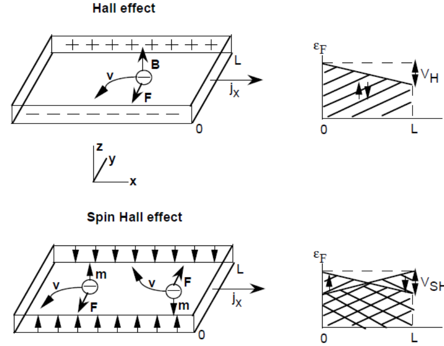

Figure 2.6: The carriers involved are electrons. The first image presents the Hall effect, where the Lorentz force generates charge imbalance. In the case of SHE, the V_{SH} voltage has opposite sign for spin up and down electrons [11].

The Spin Hall effect is a fundamental ingredient for the realisation of the devices described in sec. 2.5.

The SHE is related with the *anomalous Hall effect* [11]. The latter is present in ferromagnets and it can be expressed by the Hall resistivity (transverse electric field per unit longitudinal current density):

$$\varrho_H = R_0 B + 4\pi R_s M \tag{2.7}$$

where R_0 is the Hall coefficient, R_s is the anomalous Hall coefficient, B is the magnetic field and M is the magnetization. The second term in the equation 2.7 stands for the transverse force experienced by spins when they are moving in a longitudinal electric field. In ferromagnets the current is composed by spins, so the spins' imbalance turns into a charge imbalance, easily detectable by a voltage potential. In many ferrromagnets this contribution is dominant with respect to classical Hall effect.

The R_s coefficient probably originates from skew scattering by impurities and phonons and 'side jump' mechanism [11].

In paramagnetic materials (such as semiconductors) the current is composed by mixed spins, because no net magnetization is present. A net spin imbalance derives, but no charge accumulation does, as shown in figure 2.6. The absence of charge accumulation equals to no transverse voltage.

In some paramagnetic materials, this effect is able to cause a transverse voltage, with a mechanism similar to anomalous Hall effect. When a spin polarized current is flowing into the semiconductor and the spins are splitted, the spins accumulated on one side are more numerous that the others, therefore a charge accumulation happens and a transverse voltage is detectable. There are two possible mechanisms that generate a spin current [27].

One is called *extrinsic* and is connected with any kind of potential that prefers to scatter a spin population rather than the other. Usually, it can be understood as the result of a *spin-orbit scattering*. If the material in which the current is flowing has spin-orbit coupling, an unpolarized electron beam will suffer a potential that induces a spin polarization.

The other possibility is an *intrinsic* SHE. It is present only in systems with spin splitting that depends on electron's wave vector k (such as Rashba semiconductors, see section 2.3). In that case, an electric field automatically selects a spin population and polarizes the current.

The spins now suffer the Lorentz force between their magnetic moment and the charge current: they are scattered in different directions depending on the spin sign.

In anomalous Hall effect, the transverse potential drop can be calculated as:

$$V_H = 4\pi R_s L j_x n_\uparrow \mu_B \tag{2.8}$$

where R_s is the anomalous Hall coefficient already seen in eq. 2.7, L is the width of the sample, j_x is the longitudinal current density, μ_B is the Bohr magneton and $n_\uparrow$ is the spin up density of electrons.

Hirsch [11] demonstrated that the spin Hall voltage drop can be calculated in a very similar way as:

$$V_{SH} = 2\pi R_s L j_x n \mu_B \tag{2.9}$$

in which n is the total conduction electrons' density. The equation 2.9 shows the difference of potential detectable at the sides of a Hall bar when a density current j_x flows and it is valid both for intrinsic and for extrinsic SHE.

There are two main ways to detect V_{SH} [11]. The first one measures the magnetization at both sides of the slab in which the current flows. It can be done thanks to optical methods, such as *Magneto Optic Kerr Effect* (MOKE) as successfully performed by Kato et al. [27]. By employing this method it is difficult to distinguish the contribution on the magnetization induced by SHE and the one induced by the magnetic field generated by the current. In fact, the current forms an out-of-plane magnetic field with opposite direction in the two halves of the slab.

Another way to obtain the V_{SH} is to detect the transverse spin current. This is performed by simply measuring the voltage drop at the two sides of the slab. It is possible to obtain a correct measurement only if the width of the slab (L in the formulas) is: $L < L_s$, where L_s is the spin diffusion length in the material.

2.5 GeTe-based Concept Devices

The main features of FERSCs have been treated in sec. 2.3. Its ferroelectricity can be exploited as element for a non-volatile memory. Furthermore, the connection between ferroelectric polarization and spin texture permits the electrical manipulation of spins.

In this section three different solutions will be presented, starting from the spinFET and concluding with a totally electrically controlled spintronic device.

SpinFET The FERSC-based spinFET is sketched in figure 2.7. In this device there are three memory elements: two ferromagnetic electrodes and one GeTe channel. The memory feature of the channel is connected to its ferroelectric polarization, that is changeable by the application of a gate voltage V_g.

The injected spins are manipulated by an effective magnetic field produced by the ferroelectric magnetization and controlled by the gate voltage. The origin of the effective magnetic field is the Rashba effect (see sections 2.2 and 1.5.1). If we refer to the relationships seen in the Datta and Das model section 1.5.1, it is possible to express the differential phase shift of

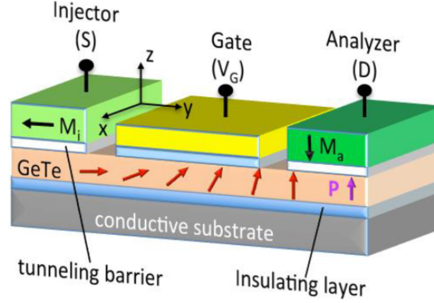

Figure 2.7: Non-volatile spinFET device concept. Gate voltage and back contact allow the switch of the ferroelectric polarization.

the spinFET shown in fig. 2.7. Now, if a phase shift of $\pi/2$ is imposed, the channel length will be

$$L = \frac{\pi}{2} \frac{\hbar^2}{m^* \alpha_R} \tag{2.10}$$

in which the relation $\alpha_R = 2\eta$ has been used. The rotation of $\pi/2$ is preferred to the total spin-flip (rotation of π) because it is easier to obtain but it does not compromise the spin-FET functionality.

The innovation in this concept device lays in the channel's memory: the GeTe-based spinFET is capable of reading and writing a non-volatile electrically controlled memory. It is a great advantage with respect to the previous memory technology, because it permits to manipulate a magnetic feature (spin) without magnetic fields. The controller of the channel's memory behaviour is an electric field, that is simpler to create and manage if compared to a magnetic field. Furthermore, magnetic electrodes can be manipulated by a magnetic field and allow other series of combination with channel state: this permits many logical combinations that are summarized in tables 2.8.

For example, look at the first line of table 1 in fig. 2.8, according to which the spins are injected in the horizontal direction. The GeTe channel has a voltage bias that gives an energetic advantage to the spin "up" (along the out-of-plane direction) carriers with respect to the spin "down" ones. At the detection electrode, the spin majorities are spins "up". These are majorities also into the detection channel: therefore, the system is in the low resistance state. Now, consider also the lines of table 2 in fig. 2.8: the

Table 1

M_i	M_a	$P(V_G)$	$R_e(V_{out})$	Spin rot.
←	↓ (0)	↑ (1)	L (0)	→ ↗ ↑
←	↓ (0)	↓ (0)	H (1)	→ ↘ ↓
←	↑ (1)	↑ (1)	H (1)	→ ↗ ↑
←	↑ (1)	↓ (0)	L (0)	→ ↘ ↓

Table 2

M_i	M_a	$P(V_G)$	$R_e(V_{out})$	Spin rot.
→	↓ (0)	↑ (1)	H (1)	← ↙ ↓
→	↓ (0)	↓ (0)	L (0)	← ↖ ↑
→	↑ (1)	↑ (1)	L (0)	← ↙ ↓
→	↑ (1)	↓ (0)	H (1)	← ↖ ↑

Figure 2.8: Table of truth of a GeTe-based spinFET. Different rows correspond to different combinations of electrodes' magnetizations and channel polarization. The high (low) resistance state H (L) refers to a logic state 1(0).

switch in the magnetization of one electrode causes the logic function to invert, exactly as a change in the voltage bias. It is possible to implement the logic function *and* between the magnetization of one electrode and the gate voltage (with the convention expressed in fig. 2.8) as in the third line in table 1.

Edelstein-Rashba spin transistor *Edelstein-Rashba effect*, as mentioned in sec. 2.2, is one of the main causes for the interest in Spin Orbitronics.

The concept device is shown in fig. 2.9. The FERSC has been opportunely oriented in such a way to have in-plane spin polarization of the current along the channel direction.

The Spin Hall effect (see sec. 2.4) causes a spin accumulation in the up-down sides of the structure (see red and blue arrows in fig. 2.9); therefore there is spin (and charge) accumulation under the magnetic analyzer. The spins' orientation with respect to the FM magnetization determines the high/low value of resistance.

The ferroelectric polarization can be controlled by the gate voltage: switching the FE polarization inverts the spin of the polarized current in the FERSC channel. This means the switching of the resistance exiting from

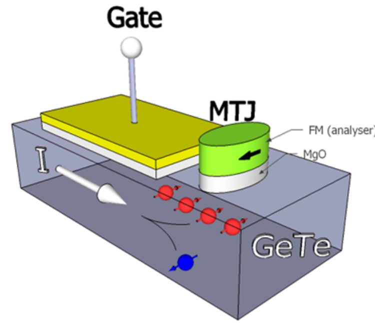

Figure 2.9: The FERSC channel generates an in-plane spin-polarized current and a spin and charge accumulations in the up-down directions. Switching the ferroelectric polarization corresponds to a switching in the resistance state, because the spins change their orientation with respect to the FM magnetization.

the MTJ. The transistor can be interpreted as a MTJ where one electrode is substituted by FERSC.

This device geometry realizes a transistor in which no magnetic field is needed. The magnetic element is used as analyzer, while the injector is removed.

It should be noticed that the inversion of the FM magnetization has the same effect as the inversion of the FE polarization.

This kind of device is really interesting from the MRAM applications (see sec. 1.5) point of view. Everspin (www.everspin.com), the MRAM sector leader, has recently begun to sale the new *Spin Transfer Torque* (STT) MRAMs (their operation is described in sec. 1.5). Germanium Telluride permits the injection of spins into a FM layer exploiting the Spin Hall effect, without the necessity of high currents.

Spin Hall Transistor without ferromagnets An electric current flowing along a FERSC channel oriented in a particular symmetry direction will be spin-polarized in the out-of-plane direction. The right-left scattering due to SHE (sec. 2.4) produces spin and charge accumulation at the lateral sides of the device, as shown in fig. 2.10(a). The measured lateral voltage is therefore function of the ferroelectric polarization controlled by the gate voltage. Both the writing (through the gate voltage) and the reading (through the lateral voltage) actions do not need magnetic fields, paving the way to a

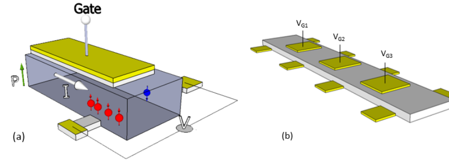

Figure 2.10: (a) An out-of-plane spin polarized current is formed in the FERSC channel. The gate voltage determines the FE polarization and therefore the spin orientation. Due to the SHE, a spin and charge right-left accumulation occurs determining a lateral voltage. The switching of the polarization implies a change in sign of the lateral voltage. (b) Sketch of the multi-gate (3) Spin Hall Transistor.

totally electrically controlled Spintronics.

This kind of device can be interpreted as a non-volatile memory element. A possible application concerns the realization of many gates and many lateral contacts, aligned on a FERSC channel, as sketched in fig. 2.10(b). Through the passage of a current, the lateral voltage of a single structure can be interpreted as the reading of a bit of information. Each of the different sections of the channel represents the bit of a non-volatile fully electrical memory.

In a very long-term vision, the same geometry can be applied to the magnetic domain walls handling. In fact, when two subsequent gates have opposite biases, the spins that constitute the current have to rotate their polarization direction to continue their trip in the next domain with opposite polarization. In doing this, a domain wall is formed and can be handled through the modification of the gate voltages.

Chapter 3

Experimental Techniques

3.1 LASSE: LAyered Structures for Spin Electronics

The aim of Spintronics is to design structures capable to control and handle carriers' spins in materials. In doing this, much effort has been spent by research and industry in the last few years resulting in the development of structures composed by layers of different materials, often in the dimensions of few nanometers and/or with reduced dimensionality (i.e. nanowires, quantum dots). These structures are called heterostructures. The process of growing a multilayer is complex because it is necessary to achieve good interfaces between layers. A good interface must be clean and with a high lattice order, so as to ensure the crossing of carriers avoiding scattering events (see section 1.1). There are many processes capable of growing multi-layers on semiconductors. For example, *sputtering* is a technique consisting in the ejection of atoms from a target as consequence of physical impacts with ions and the attachment on the sample. In the *evaporation* process, the molecules come from a hot crucible warmed by an electrons beam. This kind of process is used in the contacts' deposition (usually in gold) and it has very high deposition rate. In many cases it could be necessary to control the thickness of a layer with the precision of nanometers. It is performed thanks to a particular evaporation process called *Molecular Beam Epitaxy* (MBE). Substantially, it consists in an evaporation with a very low rate, that permits an epitaxial growth and a direct control of the stoichiometry,

as described in sec. 3.1.2. This technique has been used in this thesis for the growth of iron on Germanium Telluride because we aimed to grow an epitaxial film (see sec. 4.6).

LASSE (LAyered Structures for Spin Electronics) permits the growing process of heterostructures with sharp interfaces thanks to a wide vacuum environment, composed by many chambers [43]. It allows growth by MBE and Pulsed Laser Deposition (PLD) and characterization of thin films and heterostructures by spectroscopic techniques (LEED, RHEED, XPS, IPES). The laboratory is placed in the L-ness center in Como and it is employed for Spintronics research by the NanoBiotechnology and Spintronics group (NaBiS). In the course of this thesis work, LASSE has been exploited in many growth processes and many X-ray Photoemission Spectroscopy (XPS) analysis.

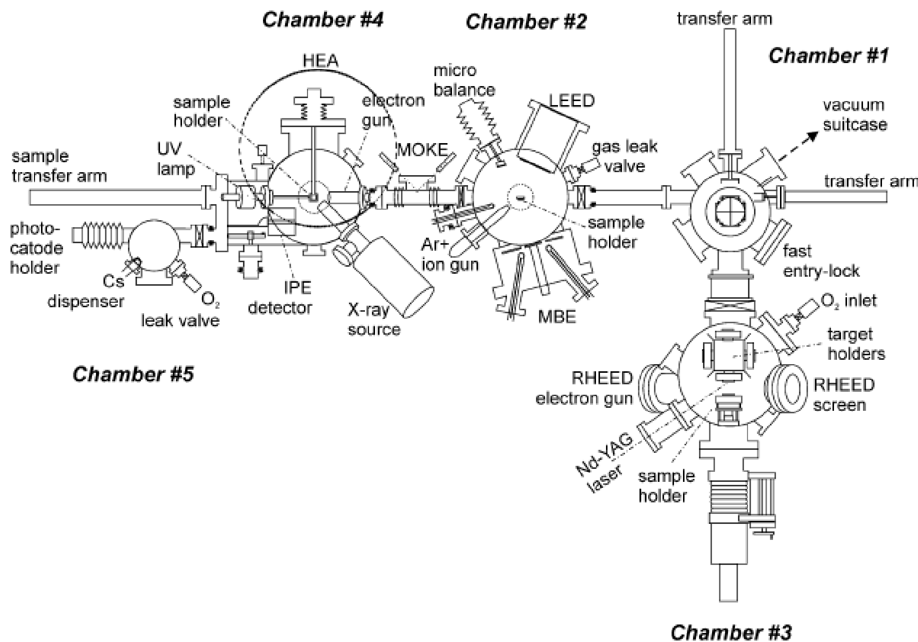

Figure 3.1: Schematic plain view of LASSE.

3.1.1 Structure

The figure 3.1 shows the LASSE structure in which it is possible to distinguish the 5 chambers that compose it. They are the *Introduction Chamber*(IC), the *Sample Preparation Chamber* (SPC), the *Measurement Cham-*

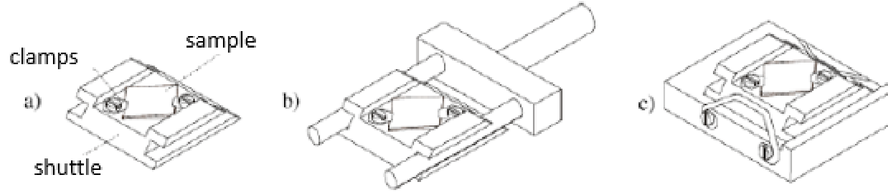

Figure 3.2: Sketch representing (a) the shuttle on which the sample is mounted on, (b) the fork and (c) the sample holder.

ber (MC), the *Photocathode Preparation Chamber* (PPC) and the *Pulse Laser Deposition Chamber* (PLDC). The last one is used for the pulsed laser deposition and will not be treated here. The PPC is employed for Inverse PhotoEmission Spectroscopy (IPES); this kind of probing technique will not be used in this thesis work, therefore the PPC structure will not be analyzed.

The sample is mounted on a shuttle and it is inserted into the *Introduction Chamber* (IC). The movement from IC to other chambers is allowed thanks to mechanical arms controlled from the outside by magnetic manipulators. The shuttle matches a fork assembled at the end of the arm (see figure 3.2); once arrived in the chamber of destination, the shuttle is released on a sample-holder mounted on a manipulator with five degrees of freedom (x, y, z, θ and ϕ). A similar movement permits the handling of a sample always keeping ultra high vacuum condition. In fact, every chamber is equipped with many pumps capable of pressures from 10^{-10} to 10^{-7}mbar. The contamination of a surface is proportional to the pressure of the surrounding environment, therefore this mechanism helps the surface cleanness. The other parameter involved in the surface's contamination is the time: the number of contaminants hitting the surface is related to $p \cdot t$, where p is the pressure and t is the time during which the sample is exposed at that pressure. The best thing to do is then to keep the sample in the lowest pressure environment for the minimum time possible.

Introduction Chamber(IC). The Introduction Chamber (1 in fig. 3.1) allows the insertion of the sample holder in LASSE. This zone is designed to support a rapid change in pressure. In fact when charging of a sample in LASSE is required, the pumping stage of the chamber is closed and the

pressure is raised to the atmospheric level through the flow of N_2. This flow has the further advantage to passivate the walls. Then it is possible to open the porthole and insert manually the sample by placing it on the arm fork.

The pressure range of the chamber moves from atmospheric level to 10^{-8} mbar thanks to the combined effect of a rotative pump and a turbo pump. This value is sufficient to allow the transfer to the SPC chamber without compromising its better vacuum level ($\sim 10^{-10}$ mbar).

Sample Preparation Chamber (SPC). The use of this chamber (2 in fig. 3.1) is necessary in every process connected with the preparation of the sample surface and the deposition of layers by *Molecular Beam Epitaxy* (MBE).

A turbo pump ensures about 10^{-10} Torr, a pressure suitable for a clean surface. It is possible to remove the contaminants in two ways: by sputtering or by annealing. Sputtering is a technique that consists in striking the sample with energetic Ar^+ ions. It may damage the surface, so a following annealing is suggested.

Annealing of a sample is useful to recover the surface order and to desorb some contaminants (especially water), which are two fundamental conditions for the growth of a heterostructure conserving the crystalline order of each layer and the sharpness of the interfaces. The sample is warmed by a current flowing in a filament placed behind the holder. There are up to seven crucibles or rods (as Fe, Mgo, Co, Pd, Au) that allow growing different materials through Molecular Beam Epitaxy (MBE). The simultaneous presence of a growth and a cleaning equipment in the same chamber enables to achieve clean interfaces without moving the sample.

The crucibles are kept at low temperatures by a refrigerant system, so it is possible to grow layers in ultra high vacuum (UHV): usually during deposition the pressure is lower than 5×10^{-10}mbar. The deposition rate is controlled by a quartz micro-balance. This procedure is adopted every time that a thin films deposition is needed.

Measurement Chamber (MC). In the *Measurement Chamber* (4 in figure 3.1) the characterization of the sample surface is obtained by electron spectroscopy. It is possible to perform *X-ray Photoemission Spectroscopy* (XPS),

Ultraviolet Photoemission Spectroscopy (UPS), *Inverse Photoemission Spectroscopy* (IPES) and *Spin Polarized Inverse Photoemission* (SPIPE). The chamber is in UHV and directly in contact with the SPC.

In XPS, x-rays are created by the flowing of a current in a Mg or an Al filament. The choice of the source depends on the radiation energy and linewidth desired. The Mg-Kα source is centered in 1253.67 eV with a $\Delta E = 0.8eV$; the Al-Kα mean energy is 1487.67 and $\Delta E = 1eV$. The Mg filament has the thinner linewidth of 680 meV, while the Al filament is of 830 meV. For further information about XPS procedure see the section 3.4.

3.1.2 Molecular Beam Epitaxy

During the thesis work, many samples have been grown by deposition in LASSE. The name of the used technique is *Molecular Beam Epitaxy* (MBE) and it will be treated here in detail. The basic concept is to deposit material on a substrate in terms of an atoms' beam. The beam originates from two kinds of Knudsen cells: materials with evaporation temperature lower than the working temperature have rod shape, otherwise they lay in Ta, Mo or quartz crucibles. The evaporation from a Knudsen cell is granted by a thermoionic emitted electron beam from a W filament. The main advantage of MBE consists in the highly quality of the molecular beam: the density of defects of the deposited layers is lower than any other deposition technique. The water-based cooling system and a degas of the filament and the rod (or crucible) are very important for ensuring the quality of the deposited material.

The *deposition rate* depends on both the filament and the rod or crucible conditions. The current in the filament determines the number of electrons emitted by thermoionic effect. Also, the aging of the filament involves a changing in its work function and modifies the electrons emission. The power on the target is controlled manually and it decides how many electrons will hit the material and how their energy will be. Eventually, the quantity of target material contributes to the deposition rate. As told in the previous subsection, a quartz balance is present in SPC. It is capable of determining the deposition rate analyzing the variation in its resonance frequency. The

equation that governs this behaviour is

$$\frac{\Delta f}{f} = -\frac{\Delta m}{m} \tag{3.1}$$

the variation of mass deposited on the balance (that has been previously placed in front of the emission cell) causes a variation of the resonance frequency. From the deposited mass it is easy to determine the deposition rate passing through the density and the sticking coefficient of the material.

3.2 Magnetron Sputtering

In the last few years the industry interest in Spintronics supported the development of cheaper techniques (in terms of time and materials) for the growth of heterostructures. This means that the techniques should have the features of: high deposition rate, high automation level and fine control of the deposition thickness. One of these techniques is deposition by sputtering.

In a sputtering process the deposition of a film is realized through the ejection of atoms from a solid target material due to the bombardment by energetic particles. In this thesis only physical sputtering will be considered, so the main event of the process is the momentum transfer between the incident particles and the target. For most materials the suggested ion beam current is composed by heavy atoms such as argon (Ar) in order to maximize the momentum transfer. In the chamber a gaseous plasma is generated, in our case using Ar gas. The material to evaporate is called *target* and it is charged with negative voltage. The Ar^+ ions are accelerated towards the target, the electrons in the opposite direction and both are capable of ionizing other ions. Thus, the plasma is initialized.

The magnetron sputtering is a particular type of sputtering in which permanent magnets are placed behind the target in order to trap electrons, otherwise these would be capable of hitting the substrate and could cause heating and damaging of the sample's surface. The magnetron sputtering process is depicted in fig. 3.3. In the case of insulating or ferromagnetic layers, some problems can occur. For the deposition of insulators, it is necessary to perform a *plasma-strike* at high Ar pressure in order to set the plasma. Furthermore, a radio-frequency varying bias is preferred to a

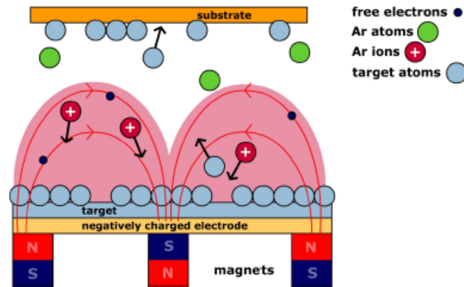

Figure 3.3: Schematic view of the magnetron sputtering process.

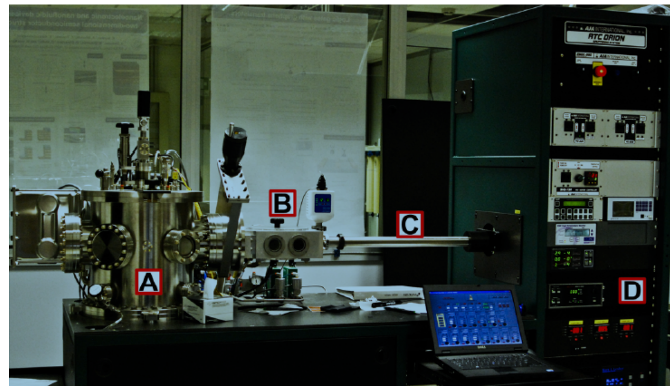

Figure 3.4: AJA ATC Orion sputtering system. A is the deposition chamber, B the load-lock, C the transfer arm, D the generators that power the sources located under the deposition chamber.

d.c. one because it avoids the charging of the substrate. For ferromagnetic materials, their magnetic fields are capable of disturbing the deposition. Especially designed magnets put behind the target solve this problem by counter an opposite magnetic field to the stray field generated by the FM material.

In this thesis work, heterostructures of CoFeB/MgO/Ge have been grown by the *AJA ATC Orion Sputtering System* (see figure 3.4). This system has 10 sources placed in the bottom of the A chamber, each one facing a common focal point. The substrate is mounted on a support with variable height; the deposition position corresponds to the focal point of the sources. It is possible to rotate the sample during deposition in order to obtain uniform films. The sources are covered with pneumatic shutters that permit a fine control of the deposition thickness up to 0.1 nm. The basic pressure in the

main chamber is kept in the 10^{-9} Torr by a cryopump. As shown in fig. 3.4, there is a load-lock chamber pumped by a turbo-pump that permits a rapid insertion of the sample without compromising the main chamber pressure. In fact the transfer between the two chambers that compose the system is done when the load-lock pressure reaches the 10^{-6} Torr range. The control of the entire process is granted by a Labview software: it is possible to program the deposition process in order to obtain high repeatability of the growth. The deposition rates are periodically checked thanks to a quartz balance installed in the main chamber or ex-situ by AFM.

3.3 Low Energy Electron Diffraction: LEED

The atomic order of the surface is very important to obtain a good interface for the spin injection (see section 1.1). One possibility to probe the 2D geometry is the *Low Energy Electron Diffraction* (LEED). It has been performed in LASSE (in particulary in the SPC, ref. 3.1) during the preparation of Ge and GeTe samples.

In 1927 Davisson and Germer demonstrated the low energy electrons elastic scattering and that was the first proof of the electrons' wave nature. In fact, in 1923 de Broglie introduced the *electron's wavelength*:

$$\lambda_e = \frac{h}{p} = (150/E_{kin}(eV))^{1/2} \tag{3.2}$$

If electron kinetic energy E_k lays between 20 and 500 eV, the de Broglie wavelength is comparable to the lattice parameter and the inelastic mean free path (see section 3.4) is lower than $10\mathring{A}$. This implies that the resulting diffraction's figure will be linked to the surface geometry.

A LEED system is composed by an electron gun, an accelerating grid, some retarding grids and a fluorescent screen as shown in figure 3.5. The accelerating grid is brought to a V_0 potential in order to accelerate electrons towards the sample. The electrons that scatter on the sample are reflected back and pass through three or four retarding grids. These grids have the function of filtering electrons, thus some of them need to be at negative bias $-(V_0 - \Delta V)$. The first grid is at ground potential as the sample: in

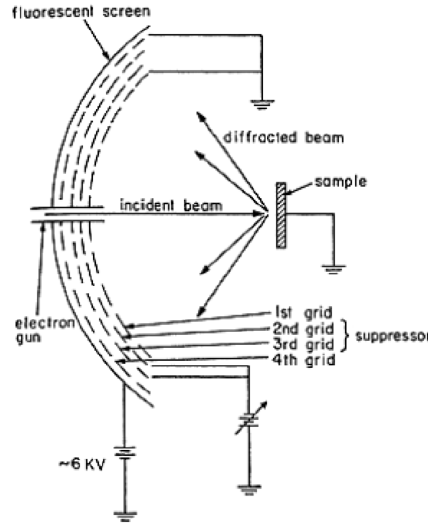

Figure 3.5: Schematic view of the LEED system.

this way a no-field zone is created that minimizes the deflections of the diffracted electrons. The last grid is also grounded in order to avoid the field penetration near the fluorescent screen.

The fluorescent screen has a weak positive potential. Here diffraction spots are projected and it is possible to deduce the surface geometry by applying a simple cinematic model to their spatial distribution. The *cinematic theory* neglects multiple scattering events of electrons.

Further information is given by the intensity of the spots, but its interpretation is possible only with the application of a *dynamic theory*, i.e. considering multiple scattering.

Here we will treat the cinematic model for low energy electron diffraction. We should have the maximum intensity points for:

$$\mathbf{K}_{\|} = \mathbf{k}^{\mathbf{f}}_{\|} - \mathbf{k}^{\mathbf{i}}_{\|} = \mathbf{G}_{\| } \tag{3.3}$$

where $\mathbf{k}^{\mathbf{i}}_{\|}$ and $\mathbf{k}^{\mathbf{f}}_{\|}$ are the wave vectors of the incident electron and of the diffracted one and $\mathbf{G}_{\|}$ is a reciprocal lattice vector. For $\mathbf{K}_{\perp}$ there is no condition. The equation 3.3 is perfectly respected only if one layer is involved in the diffraction. The figure that appears on the screen is the *reciprocal lattice*

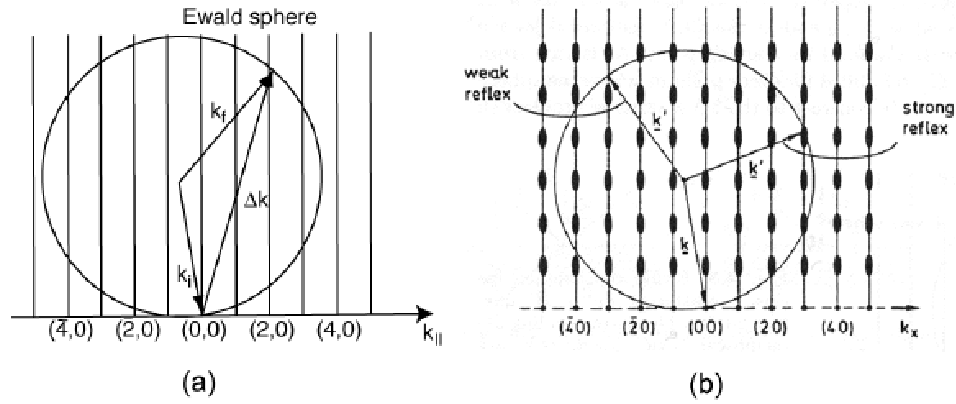

Figure 3.6: (a) Ewald sphere in a 2D lattice electrons' diffraction. (b) Ewald sphere in the case the electrons probe more than one layer. The third Laue condition thickens the rods, modifying the resulting intensity.

image of the surface and each point is a constructive interference between the diffracted electrons.

There is a graphic method to interpret the cinematic theory. It is the *Ewald sphere* construction and it is deducible through the relaxation of the third Laue condition for diffraction.

The Laue conditions for scattering require that the difference between the diffracted wave vector and the incident one in the k-th direction is $\frac{2\pi n}{a}$, where n is an integer number and a is the lattice parameter in the k-th direction.

The scattering from a 2D plane can be interpreted like a scattering from a 3D lattice, where one direction presents infinite period. Therefore, the reciprocal lattice will have no periodicity in that direction, showing lines (called *rods*) instead of points.

In order to obtain the $\mathbf{k_{\parallel}^{f}}$ values the graphic method requires to draw a sphere with $\mathbf{k_{\parallel}^{i}}$ radius. The center of the sphere is determined by pointing the incident vector to the $(0,0)$ (origin) of the reciprocal lattice, as shown in fig. 3.6(a). When the sphere intersects one rod, constructive interference happens.

In a real case, electrons probe many layers, not only the upper one. This means that the third Laue condition is partially satisfied. The result

is shown in figure 3.6(b): the intensity of the rods varies periodically. The thickening of the rod, if intersected by the Ewald sphere, causes the intensity to grow with respect to a thinner point.

The LEED figure does not give just a qualitative information about the symmetry of the surface lattice. The positions of diffracted points are connected with precise locations in reciprocal space. Therefore, the surface reciprocal lattice is "impressed" on the screen and the direct space lattice can be deduced.

In particular, we are interested in the *lattice parameter* of Germanium Telluride. In fig. 3.7 the simplified geometry of a LEED experiment is illustrated. From the Laue conditions, with the incident electron's vector normal to the sample's surface ($k^i_{\parallel} = 0$), the diffracted electron's parallel wave-vector is

$$k^o_{\parallel} = \frac{2\pi}{a} \tag{3.4}$$

where a is the lattice parameter and only the first order of diffraction ($n = 1$) has been considered.

The relation between the kinetic energy and the wave-vector of the diffracted electron can be obtained from

$$E_{kin} = \frac{\hbar^2 k^2}{2m} \Longrightarrow k = \frac{\sqrt{2mE_{kin}}}{\hbar} \tag{3.5}$$

where k is the modulus of the diffracted electron's momentum and E_{kin} is its kinetic energy.

Using eq. 3.5 and expressing the wave-vector's component parallel to the surface, we can obtain:

$$k^o_{\parallel} = ksin\theta = \frac{\sqrt{2mE_{kin}}}{\hbar}sin\theta \Longrightarrow sin\theta = \frac{\hbar}{\sqrt{2mE_{kin}}}k^o_{\parallel} \tag{3.6}$$

where θ is the angle of the diffracted electron's momentum with respect to the surface normal (it is also represented in fig. 3.7).

Referring to fig. 3.7 we can express

$$\frac{r}{R} \simeq sin\theta = \frac{h}{\sqrt{2mE_{kin}}a} \Longrightarrow a = \frac{hR}{\sqrt{2mE_{kin}}r} \tag{3.7}$$

where R is the distance between the sample and the screen and r is

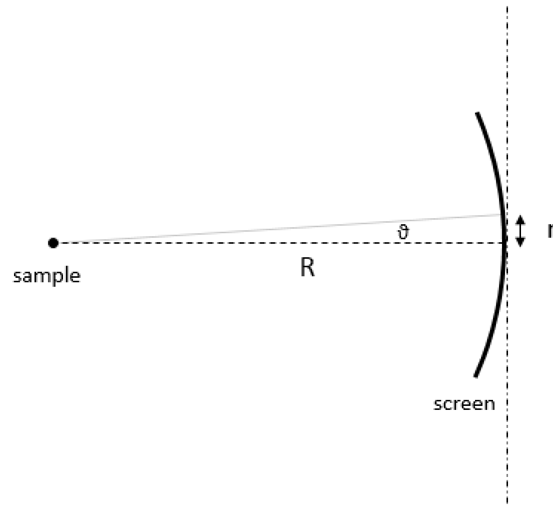

Figure 3.7: Sketch of the geometry of a LEED experiment.

the distance between the diffraction point and the center of the screen. An approximation has been made: in eq. 3.7 the distance between the sample and the diffraction point on the screen has been considered as equal to R, because $R >> r$.

In the Germanium Telluride case, this calculation gives a lattice parameter equal to 4.12 Å.

If a surface does not have a periodical order, the diffracted electrons do not form a diffraction figure. Defects and high temperature increase a background of scattered electrons. In this case, the retarding grids are fundamental to stop the inelastic scattered electrons and to permit the elastic ones to show diffraction.

3.4 Photoemission Spectroscopy

The comprehension of the chemical composition and the band structure of a material can be reached using Photo-Emission Spectroscopy (PES) techniques. The basic concept consists in focusing monochromatic photons on a surface and studying the energies and momenta of emitted electrons. These parameters offer information about the occupied electronic structure of the sample. If we wish to know the unoccupied band distribution (states above

the material Fermi level), an *inverse photoemission spectroscopy* (IPES), that is a time-reversal version of PES, will be necessary.

The importance of PES in this work has mainly two reasons:

- to check the contaminants' presence and position, the material's stoichiometry and the effect of preparation processes on these ones;
- to deduce the thickness of a deposited material.

The development of photoemission techniques has been obtained thanks to the understanding of the *photoelectric effect*. The effect, studied by Albert Einstein in 1905, considers how an incident photon can transfer its energy to an electron that is able to get to the surface and then to be emitted.

Before reaching the surface, the electrons suffer scattering events in the material. The electron that will be analyzed has to be coherent. This means that it must not lose energy and change its momentum, otherwise the information on the electronic structure will be compromised. Therefore a main length on which the electron keeps coherent exists: *Inelastic Mean Free Path* (IMFP). This parameter depends on the kinetic energy of the electron but it is quite independent from the kind of material; in fact a universal curve well describes the IMFP for most materials.

Photoemission spectroscopy has different names depending on the incident photons energy. If the light is ultraviolet (UV), it will be called UPS (*UltraViolet Photoemission Spectroscopy*), otherwise if X photons are used, we will talk about XPS (*X-ray Photoemission Spectroscopy*). The second is mainly used for chemical analysis of surfaces, because of the X-rays' capability of probing the elements' core levels. Studying the peaks' positions it is also possible to understand the oxidation and generally the bonds involved in the material. This use of PES is called *Electron Spectroscopy for Chemical Analysis* (ESCA).

UPS has a different application: its photons are less energetic in comparison with X-rays, so they are able to probe states near the material Fermi level. Moreover, the materials' cross sections around the valence band are larger for ultra-violet light if compared to X-rays, thus the intensity of the VB has higher values. Therefore valence band studies are often performed

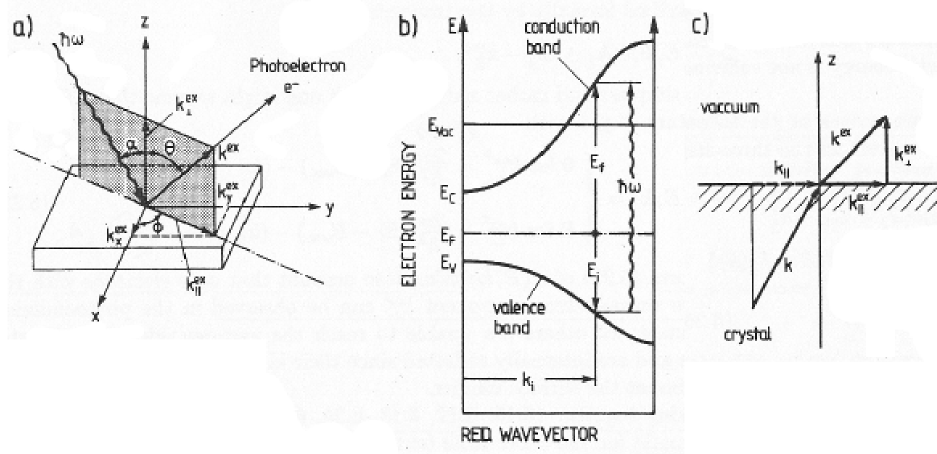

Figure 3.8: Schematic view of a photoemission experiment. (a) Geometry of the problem. (b) Band structure of a semiconductor during a PES experiment. (c) Electron wave-vectors situation: the parallel component $k_{\|}$ conserves while the perpendicular one ($k_{\perp}$) does not because of the symmetry break of the surface.

and permit a mapping of the first bound states, particularly meaningful in bands alignment studies.

3.4.1 Three Steps Model

The photoemission process can be interpreted basically with two different models. The first and most accurate of those is a quantum mechanical treatment of the electron excitation from an initial Bloch state to a final state called *time-reversed LEED state*. It treats the photoemission event as one single step. The second possibility is to consider the photoemission as a combination of three different events. The model that provides this interpretation is called *three steps model* and, although it is less precise than the first model, it is simpler and more intuitive. In the present thesis the latter model will be explained.

The steps involved are the following:

1. Optical Excitation of the electron.

2. Propagation of the electron towards the surface.

3. Emission.

The independent treatment of the three conditions leads to a simple factorization of the corresponding probabilities into the photoemission current formula.

Optical excitation. The first step simply respects the *golden Fermi rule* for optical transitions:

$$\begin{aligned} W_{fi} &= \frac{2\pi}{\hbar} | < f, k_f | H' | i, k_i > |^2 \delta(E_f(k_f) - E_i(k_i) - \hbar\omega) \\ &= \frac{2\pi}{\hbar} m_{fi}^2 \delta(E_f(k_f) - E_i(k_i) - \hbar\omega) \end{aligned} \tag{3.8}$$

In the equation, the probability of the transition is the combination between the matrix element and the energy conservation, that is taken into account by the delta function. In a first approximation vertical transitions are considered: it means that the photon momentum is negligible compared with the electron one so the initial and final momenta are the same. The matrix element contains the perturbation operator H': it is given by the momentum operator ($\boldsymbol{p}$) and the vector potential $\boldsymbol{A}$ of the electromagnetic wave in dipole approximation:

$$H' \simeq \frac{e}{m} \mathbf{A} \cdot \mathbf{p} \tag{3.9}$$

The electron participating to the photo-current has to fulfill two more conditions: a final energy E above the vacuum level (E_{vacuum}) and a momentum in the outgoing direction from the surface (ie $k_\perp > 0$). The internal photo-current density is therefore the sum of all the occupied internal states and the unoccupied external ones:

$$I^{int}(E, \hbar\omega, \mathbf{k}) \propto \sum_{fi} m_{fi}^2 \cdot f(E_i) \cdot \delta(E_f(k) - E_i(k) - \hbar\omega) \delta(E - E_f(\mathbf{k})) \tag{3.10}$$

where $f(E_i)$ is the Fermi distribution for the particle at the initial energy. Note that the probability of the unoccupation of the external states is taken equal to one because above the vacuum level only free electron states are considered.

Propagation to the surface. A lot of the excited electrons undergo inelastic scattering into the material. In those events they lose the information

about their initial electronic level E_i, therefore they should not be considered in the photo-current. Such electrons form a continuous background in the spectrum, which is called *true secondary background.* There is a connection between the probability of inelastic scattering and electron *inelastic mean free path* (IMFP, λ). A phenomenological formula leads to the definition of the *transport probability* $D(E, \mathbf{k})$ as:

$$D(E_{kin}, x) = e^{-x/\lambda(E_{kin})} \tag{3.11}$$

where x is the length that an electron has to travel in order to reach the surface.

Transmission through the surface. The third step is a scattering problem of Bloch electron state in a surface-atom potential with translational symmetry that is parallel, but not normal to the surface. The same conclusions are obtained considering a matching between an internal Bloch wave function and an external free-electron wave function.

Because of the 2D translational symmetry, a *quasi-conservation* of the electron momentum is present; the component of the momentum parallel to the surface is conserved:

$$\mathbf{k}_{\parallel}^{\mathbf{ex}} = \mathbf{k}_{\parallel} + \mathbf{G}_{\parallel} \tag{3.12}$$

For the external electron, the $k_{\parallel}^{ex}$ value is determined by the energy conservation:

$$\hbar\omega = E_f - E_i = E_{kin} + \phi + E_B \Longrightarrow E_{kin} = \hbar\omega - \phi - E_B \tag{3.13}$$

with $\phi = E_{vac} - E_F$, which is the work function of the solid and E_B as the binding energy referred to the Fermi level. Knowing some experimental parameters the external momentum is entirely determined:

$$k_{\parallel}^{ex} = \sqrt{\frac{2m}{\hbar} E_{kin}} \sin\Theta = \sqrt{\frac{2m}{\hbar}(\hbar\omega - \phi - E_B)} \sin\Theta \tag{3.14a}$$

$$k_{\perp}^{ex} = \sqrt{\frac{2m}{\hbar} E_{kin}} \cos\Theta = \sqrt{\frac{2m}{\hbar}(\hbar\omega - \phi - E_B)} \cos\Theta \tag{3.14b}$$

The transmission through the surface is well described by a *transmission rate*, $T(E, \mathbf{k})$, that is not zero only for electrons with positive $k_{\perp}^{ex}$.

Considering each step, an expression for the external emission current is obtained:

$$\begin{aligned} I^{ext}(E, \hbar\omega, \mathbf{k}_{\parallel}^{\mathbf{ex}}) &= I^{int}(E, \hbar\omega, \mathbf{k}) D(E_{kin}, x) T(E, \mathbf{k}) \delta(\mathbf{k}_{\parallel} + \mathbf{G}_{\parallel} - \mathbf{k}_{\parallel}^{\mathbf{ex}}) \\ &\propto \sum_{fi} m_{fi}^2 \cdot f(E_i(\mathbf{k})) \cdot \delta(E_f(k) - E_i(k) - \hbar\omega) \delta(E - E_f(\mathbf{k})) \\ &\times \delta(\mathbf{k}_{\parallel} + \mathbf{G}_{\parallel} - \mathbf{k}_{\parallel}^{\mathbf{ex}}) D(E_{kin}, x) T(E, \mathbf{k}) \end{aligned} \tag{3.15}$$

3.4.2 Angle Resolved Photoemission Spectroscopy

The electronic distribution in the reciprocal space is fundamental to understand the electronic properties of a material. There is a particular photoemission technique able to solve the *dispersion relation* (i.e. $E(\mathbf{k})$) known as *Angle-Resolved Photoemission Spectroscopy* (ARPES).

As seen in equations (3.12) (3.14), it is possible to deduce the $k_{\parallel}$ from the external momentum component value. For bulk band structure, we should face the problem of determining the internal $k_{\perp}$ component because it is not conserved.

Let's focus on the case of normal emission ($k_{\parallel} = 0$). It is convenient to assume a *free electron parabolae* final states' distribution:

$$E_f(k_{\perp}) \simeq \hbar^2 \frac{k_{\perp}^2}{2m^*} \tag{3.16}$$

In the vacuum, the kinetic energy is given by

$$E_k = \hbar^2 \frac{k_{\perp}^{ex2}}{2m} = \hbar^2 \frac{k_{\perp}^2}{2m^*} - V_0 \tag{3.17}$$

Band structure calculations can be now exploited to substitute the simpler E_f expression and so a trial-and-error procedure could be performed to deduce $E_i(k_{\perp}) = E_f(k_{\perp}) - h\nu$.

The angle-resolved PES is often used with UV sources. This range of wavelength permits a deep analysis near Fermi level. In fact, the ARUPS (Angle-Resolved UV Photoemission Spectroscopy) is performed when the valence band structure is particularly interesting.

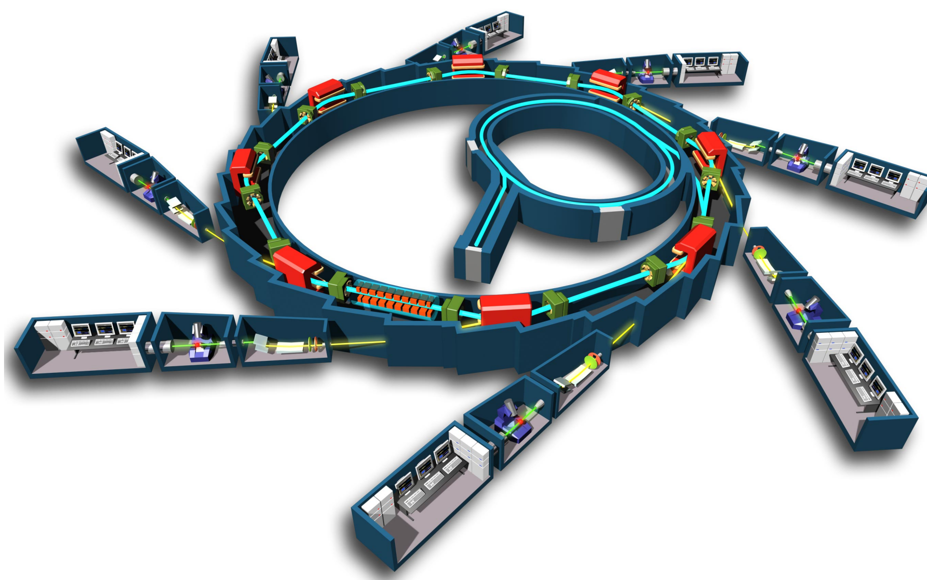

Figure 3.9: Scheme of a synchrotron as light source. It is possible to distinguish the booster, the storage ring and some beamlines.

As it has been already underlined, an ARPES measurement is capable of give a material's bands structure. A condition to have a good dispersion relation is the monochromaticity of the incident photon. A light source that grants the more monochromatic light in X-ray range of the spectrum is the synchrotron.

3.4.3 Synchrotron Light Source

The synchrotron is a particular kind of cyclic particles accelerator in which a magnetic field is synchronized with a particles beam of increasing kinetic energy. A synchrotron light source is formed by a *storage ring*, where the kinetic energy of the particles is kept constant. Here the electromagnetic radiation is generated. Then this radiation is used in different *beamlines*, i.e. different experimental stations tangent to the storage ring. The entire structure has to keep ultra high vacuum conditions (UHV) in order to avoid collisions with gas molecules and to preserve the number of electrons.

Synchrotron radiation is produced when electrons travelling at relativis-

tic speeds are deflected in magnetic fields. The fields are produced by three types of magnets: (i)bending magnets for the deflection of the electrons into a circular path; (ii)quadrupoles magnets for the focusing of the beam (for high energy electrons, magnetic fields are more efficient for the manipulation of the beam); (iii)sextupoles for the compensation of aberrations and small adjustments. The wavelength of the light is tunable by changing the magnetic field.

The electrons have to be accelerated before the injection in the storage ring. This is performed with the help of a Linear accelerator (LINAC). A ceramic disk emits electrons and then they are accelerated through various radio-frequency stages.

The beam is now transported to the *booster*. This is a simple synchrotron that acts as intermediate stage. Once the electrons reach the requested energy, they are extracted and transferred to the storage ring.

In the storage ring, the energy and the current of the beam are limited by the radiofrequency power and the thermal load in the vacuum chamber due to synchrotron radiation.

For the issuing of this thesis, part of the job has been performed at the Elettra synchrotron in Trieste, where the standard values of beam energy and current are 2 GeV and 310 mA or 2.4 GeV and 150 mA.

An important parameter for the synchrotron radiation is the *emittance*: it is defined as the area occupied by the beam in the phase space. This area should be as small as possible.

The energy spent in the radiation must be compensated into the storage ring. *Radio-frequency cavities* have to keep only electrons with energy within a given acceptance. The cavities operate at 500 MHz (in the case of Elettra light source) and accelerate only electrons arriving at the right time, while all the others are lost. This implies that the beam current will be separated in bunches, as shown in figure 3.10.

The beamline where part of this work was performed is APE. The abbreviation means Advanced Photoelectric Effect and it is a facility for spectroscopies from two distinct beamlines: polarized radiation in the ultra-violet range (low-energy line) and soft X-ray range (high-energy line) of the spec-

Figure 3.10: Beam train seen on an oscilloscope. The figure is taken from the Elettra lightsource site(www.elettra.trieste.it).

trum. In chapter 4 the results obtained from the low-energy line experiments will be presented.

3.5 Wet Etching

In the thesis work, the Germanium Telluride samples were grown by at Paul Drude Institut (PDI) by R. Calarco and co-workers. The samples were capped with silicon nitride (Si_3N_4) to avoid the exposure of the material to the atmosphere (in particular for the oxidation) and keep the Germanium Telluride surface clean. Silicon nitride is typically used as capping layer and can be chemically removed by some aggressive solutions (i.e. HF or hot H_2SO_4).

One of the solution able to etch the Si_3N_3 is hydrogen flouride (HF) and it was used in our preparation process. The procedure consists in the immersion of the sample in a solution of diluted 5% HF: this results in an etching rate of about 2 nm/min as confirmed by AFM analysis (see section 4.3.1).

Experimentally an over-etching proved to be necessary for a complete removal of Si_3N_3, otherwise residual capping layer would remain on the surface. The capping layer's thickness of our samples ranges from 6 nm to 40 nm.

This procedure is called *wet etching*. It is performed in clean room and requires several safety precautions because of the hazard of the HF. The bechers, tweezers and everything that comes in touch with hydrogen

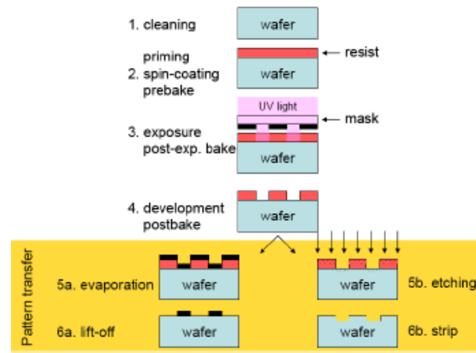

Figure 3.11: Schematic view of the steps in a direct photolithography process.

flouride must be in Teflon to avoid their etching. In order to work with HF it is necessary to wear thick gloves extended, glasses to protect the eyes and the procedure must be performed under the hood.

The sample that needs to be etched has to be immersed in the HF solution and it has to be kept in movement. This shrewdness permits a continuous regeneration of fresh solution on the surface, allowing the etching rate not to decrease.

3.6 Optical Lithography

In order to obtain a spintronic device, the design of particular physical structures is fundamental. After the growth of a multilayer by MBE or sputtering, functional geometries have to be fabricated on the sample surface. Optical lithography transfers a bi-dimensional pattern from a template to the sample. This process exploits the change in solubility of a polymer, called *photoresist*, in response to an UV illumination. The mask's image is thus transfered to the sample surface in terms of alternation of soluble and unsoluble zones. The figure 3.11 briefly shows the phases involved in the process.

The following step of the procedure is the *development*; it consists in removing the soluble resist by immersing the sample into a particular solution, called *developer*. In this chapter the direct optical lithography process will be described in every step, then the inverse lithography will be briefly treated.

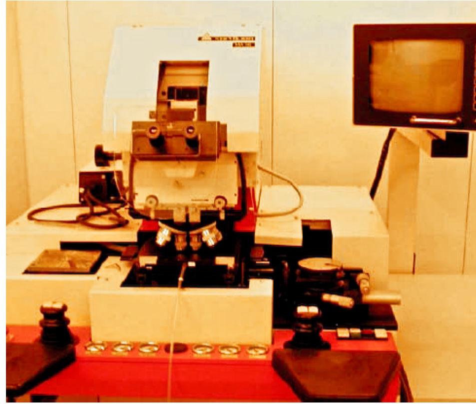

Figure 3.12: Karl Suss MA56 mask aligner.

3.6.1 Direct Photolithography

The direct photolithography process can be separated into different steps.

1. **Cleaning the sample** The sample surface is dirty with many contaminants, such as organic impurities and water. The common procedure to get a clean surface consists in an acetone bath and, if necessary, ultrasounds treatment. An isopropanol wash is suggested to remove acetone, allowing the good adhesion of the resist.

2. **Deposition of the photoresist** The resist is deposed via *spin coating*: the resist (in liquid state) is put on the sample and the former rotates at high speed (5000 rpm). At this point, the photoresist is uniformly distributed on the sample surface but it is still liquid. A soft baking at 110°C of about one minute is performed. It grants adhesion and texture of the resist.

3. **Exposure** A UV illumination is capable of changing the solubility of the photoresist by modifying the chemical bonds in the resist. The desired pattern is realized on the sample through a mask; the former is composed by a glass substrate and a Cr pattern, that absorbs the radiation.

   The alignment of the mask is made by a Karl Suss MA56 mask aligner (figure 3.12) that permits both the contact and the proximity printing. The UV lamp exploits the Hg I line (365 nm) and generates a radiation's intensity of about $12mW/cm^2$. In this thesis work the resist

employed is AZ5214E, a positive resist, which means that the exposed zones will be much soluble. On our Germanium surfaces the exposure time is about 10 s. In other cases the optical lithography could cause diffraction problems, when the minimum dimension is comparable with the wavelength. Here we are treating structures with minimum dimensions in the order of tens microns, thus the diffraction does not constitute a limit.

4. **Development** It is the crucial step of the entire lithography process. A solvent (AZ726 MIF developer) dissolves only the irradiated resist. The developing time in our case is about 30 seconds. It is a very important parameter because it determines the quality of the structure; usually an overdeveloped pattern is suggested.

5. **Deposition and lift-off** After the development there are two possible steps: one is treated here and concerns a deposition of material; the other one is described at the next point. Additional material can be deposited by sputtering or by evaporation (as in the case of contacts). The material deposes uniformly on the whole surface, but the presence of the resist avoids the direct contact with the sample. The lift-off step consists in removing the resist from the surface thanks to a solvent (AZ100 remover) and, if necessary, through ultrasounds. The resist leaves the surface thus creating zones free of the deposited material.

6. **Etching and stripping** The other possibility is to remove some material from the sample surface. In that case, a beam of Ar^+ atoms is used and its removal action is not selective. Nonetheless, the resist protects the underlying material and permits the surface design. The etching and stripping procedure has been preferred to the deposition and lift-off process in this thesis work.

3.6.2 Inverse Photolithography

Some lithographic steps are designed for image-reversal, a particular technique that permits the inversion of the photoresist solubility. This process has been used for the contacts step of lithography and gives about the same result obtainable with a negative resist. It is also called *image reversal* because it permits to have the negative of the mask design.

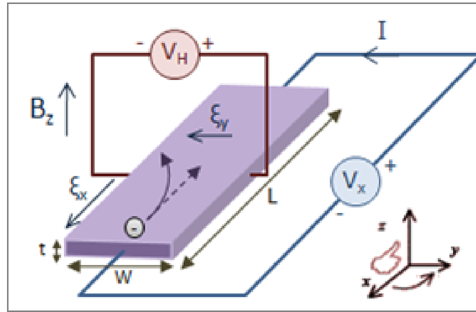

Figure 3.13: Setup for a Hall measurement for electrons. Thanks to Wikipedia for the image.

The first steps are the same as the direct photolithography described above, but between exposure and development there are two additional points:

1. **Reversal baking** This is the critical step of the procedure: a baking of the resist at 117°C for 100 seconds allows the *cross-linking* of the polymeric chains, making the exposed zones unsoluble and insensitive to further exposures.

2. **Flood exposure** The entire sample surface is exposed to the UV light. The minimum dose is $455mJ/cm^3$: a bigger dose than that value does not change the result. Now the zones not enlightened at the first exposure are soluble and are removed in the development step.

3.7 Hall Effect Measurements

On GeTe samples a first electrical characterization has been performed. Hall measurements were done, giving indications about the doping level of the samples.

The *Hall effect* arises when in a conductor the longitudinal flowing of a current causes, through the Lorentz force, the accumulation of charge carriers at the transverse sides of the conductor.

A Hall effect characterization mainly consists in measuring the *Hall coefficient* (R_H). The measurement setup is presented in figure 3.13 with names and conventions that will be used in the current section.

The coefficient is expressed as:

$$R_H = \frac{E_y}{j_x B} = \frac{V_{xy} t}{IB} \tag{3.18}$$

where E_y is the transverse electric field, j_x is the longitudinal current density and the other parameters and variables are presented in fig. 3.13.

If only one type of carrier (electrons) is involved in the transport, the measured transverse voltage will be:

$$V_{xy} = -\frac{IB}{nte} \tag{3.19}$$

where e is the elementary charge and n is the charge carrier density.

Therefore the Hall coefficient becomes:

$$R_H = -\frac{1}{ne} \tag{3.20}$$

From the sign of the coefficient it is possible to determine: (i)the type of carrier involved in the transport; (ii)the charge carrier density.

Up to this point Hall effect in metals has been dealt with. In the case of semiconductors, the Hall coefficient is slightly different from eq. 3.20. In this thesis, the results will show that the doping level of the GeTe samples is very high, and the Hall coefficient keeps the form of equation 3.20.

The system used for its measure is a Cryogenic cryogen-free superconducting cryomagnetic system. It works thanks to a closed liquid helium-4 cycle and permits a direct control of the temperature. The lowest reachable temperature is 1.6 K and the highest magnetic field is 7.5 T.

The sample is formed by GeTe grown on a slightly doped Si(111) substrate and the contacts were realized in silver glue.

The cryostat is used in order to investigate the electrical behaviour at different temperatures (see the figure 3.14).

The measurements are performed in the four points modality: while two contacts are injecting current (through a Keithley 6221 current source), the other two measure a voltage (using a Keithley 2182A nanovoltmeter and/or a 2700 multimeter). This modality implies that the measured voltage drop is caused only by the resistance in the sample and not by the quality of the contacts.

Figure 3.14: Picture of the Cryogenic cryomagnetic system.

Two curves are the main results of the measurements and are acquired concurrently: the V_{xx} curve and the V_{xy} curve. The first one is the resistance of the longitudinal path vs the magnetic field. The second one is the voltage between two pads perpendicular to the current with respect to the magnetic field. The transverse voltage V_{xy} should be zero at zero field; unfortunately the lateral contacts are not perfectly aligned, and a net longitudinal potential drop is always present.

3.8 Hanle Effect Measurements

The Hanle effect and its methods of measurement have been described in section 1.4. Here, the experimental details are presented.

Some Fe/MgO/Ge samples were grown and lithographed for three terminals Hanle measurements. The lithography procedure can be divided into three steps.

1. **Definition of mesa** The first step was the creation of structures in the Germanium substrate on which the devices will be built. This procedure was performed by one direct lithography step and etching.

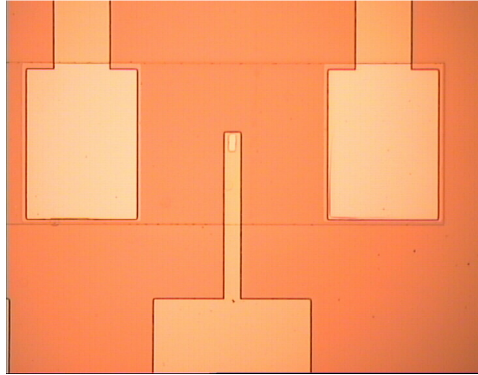

Figure 3.15: Optical microscopy (5 X) image of a three terminals structure.

The purpose is limiting the current flowing inside a volume of known dimensions.

2. **Definition of structures and deposition of silicon oxide** This step defines the real device structure. In fact, the direct photolithography designs the electrodes on the mesa, then an etching digs the mesa until Iron and MgO are present only in these structures. Subsequently, silicon oxide is deposited everywhere. The lit-off procedure permits to remove SiO_2 from the electrodes.

3. **Contacts deposition** An inverse lithographic process designs the contacts. Then the evaporator permits a fast Au contacts' deposition. Gold is in contact with iron on the electrodes, but it is not directly on Germanium, thanks to the silicon oxide. The result of this procedure is presented in fig. 3.15.

These samples were used for three terminals Hanle measurements (subsec. 1.4.2) in a cryostat, in a temperature range from 15 K to 400 K. The set up for this measurement is shown in figure 3.16(a).

The bigger electromagnet in fig. 3.8(a) is water-cooled and is capable of 4000 Oe magnetic fields. It is used for the out-of-plane field, therefore to measure the Hanle effect (1.4.1). The horseshoe-shaped magnet is employed for the in-plane magnetic field and can generate maximum 500 Oe for a limited time. The in-plane field does not have to be as intense as the out-of-plane one, thus the sample is mounted as shown in fig. 3.16(b).

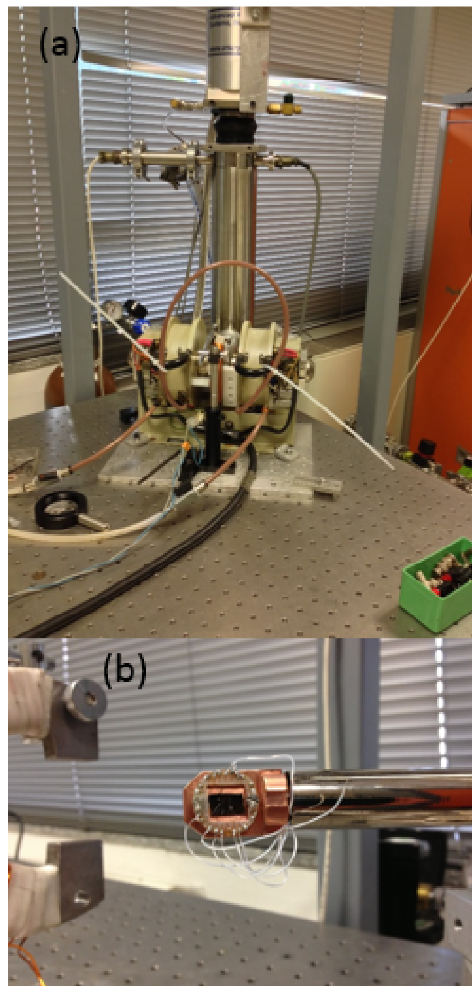

Figure 3.16: (a) Set up used for three terminals geometry Hanle measurements. There are two electromagnets that grant in-plane (inverted Hanle) and out-of-plane (Hanle) fields. **(b)** Particular of the sample mounted in the cryostat.

The current is provided by a Keithley 6221 current source and the non local voltage is measured by a Keithley 2182A nanovoltmeter.

The results of the measurements will be presented in section 4.8.

Chapter 4

Investigation of Germanium Telluride

4.1 Introduction

This thesis aims at showing experimental evidences that can confirm the interesting predicted properties presented in section 2.3. A preliminary study for the implementation of GeTe in basic devices will be also performed. A spin lifetime measurement in germanium through Hanle effect will be described, in order to prepare a future work on Germanium Telluride: measuring the spin lifetime in this material can give an idea about the feasibility of its application in spintronics and spin-orbitronics devices.

The discovery of FERSCs, the growth of GeTe thin films and the study of their properties involved several scientific groups worldwide. S. Picozzi and co-workers (CNR-SPIN, L'Aquila) identified the FERSC new class of materials and performed calculations of the band structure. These calculations will be taken into account in the analysis of the measured bands obtained through ARPES experiments.

The samples were grown by R. Calarco and co-workers in Paul-Drude-Institute (PDI in Berlin). The cooperation with NaBiS group led to the characterization of morphology (by AFM), of the surface quality (stoichiometry, oxigen and carbon contamination) before and after the sample re-preparation in vacuum and of the ferroelectric properties, in order to optimize and improve the growth process.

The samples were capped by Calarco *et al.* with a protective coating of silicon nitrite (Si_3N_4) to keep the surface clean. The capped samples were sent from PDI to the NaBiS group for advanced characterization and realization of devices. We needed first of all to remove the capping layer, prepare the surface through physical and thermal treatments in Ultra High Vacuum (UHV) environment and study the GeTe features through electronic spectroscopies (LEED, XPS, ARPES, spin-resolved spectroscopies) on the resulting fresh and ordered surface. Afterwards, we studied the growth process of heterostructures and finally we realized devices based on GeTe for the electrical characterization.

The surface preparation, the electrical characterization and the iron growth of GeTe samples were performed at L-NESS center in Como. The ARPES measurements were taken at APE beamline in Elettra (Trieste) and the spin-resolved spectroscopies were performed at Paul Scherrer Institut (PSI) in Villigen.

Starting from the theoretical background provided by S. Picozzi *et al.* and the samples grown by R. Calarco *et al.*, the present chapter will describe my thesis work, devoted to:

1. the optimization of the wet etching procedure employed to remove the samples' protective Si_3N_4 capping layer (section 4.3.1);

2. the research and the optimization of a procedure capable of obtaining ordered surfaces to permit the ARPES study and the iron (and MgO in the future) epitaxial growth (section 4.3.2);

3. the ARPES investigation of the Germanium Telluride band dispersion (sec. 4.5), performed at APE (Elettra, Trieste);

4. the investigation of the electrical properties through four probes and Hall effect measurements, to obtain the conductivity, the doping and the carriers type in Germanium Telluride (section 4.7);

5. the demonstration of the growth feasibility and the magnetic characterization of an iron layer on GeTe surface (sec. 4.6);

6. the development of devices and measurements to obtain the spin lifetime in germanium, to be extended in the future to the GeTe case (sec. 4.8).

4.2 Sample Batches

R. Calarco *et al.* (PDI) have provided different batches of GeTe samples, answering to our requests. In fact, our optimization work in preparation procedures, stoichiometric analysis, bands' and electrical properties study has given important indications about the possible improvements of the growing process.

In table 4.1 the three main generations of samples are summarized, with their peculiar features and destinations.

Generation	Main features	Destinations
1	presence of rotationaldomains	ARPES experiments
2	absence of rotational domains	AFM, ARPES, electrical measurements, Fe growth
3	thinner capping layer	Sb content analysis

Table 4.1: Germanium Telluride samples' list of generations.

The first generation is made by pure GeTe (111) grown on highly mismatched Si (111) surface ($\rho \simeq 1-10$ Ω·cm), without any optimization. This is the first attempt to grow GeTe on silicon and the samples are affected by the presence of undesired rotational domains.

The second generation avoids the issue of the first batch using a buffer layer of antimony deposited on the Si(111) surface before the co-evaporation of Ge and Te. This buffer layer prevents the formation of rotation domains. Nevertheless, during the thermal treatment of the GeTe to recover the surface (see sec. 4.3.2), the Sb could diffuse towards the surface (surfactant effect), as will describe in section 4.3.3.

To study the position and the stability of the Sb in the film matrix, a third generation has been produced: the thinnest capping layer permits to investigate this problem without using the wet etching but employing an insitu Ar-ions sputtering, keeping the UHV conditions for the whole process' duration.

4.3 Surface Preparation

All the three generations of samples underwent our procedure. The preparation process is the same for the first two generations but slightly

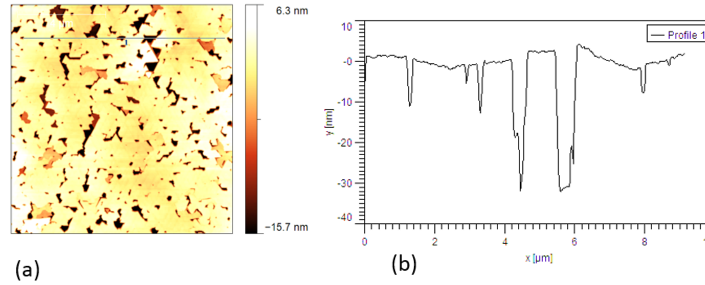

Figure 4.1: (a) 10 x 10 μm^2 AFM images of Germanium Telluride (73 nm) surface with the silicon nitride capping layer (30 nm). The chromatic scale indicates the third coordinate. (b) Surface profile along a line of fig. (a).

different in the third case. The procedure consists in a wet etching for the capping layer's removal, a sputtering for removing the contaminants and an annealing that reduces the oxidation and the carbon content, also recovering the surface order. The third generation does not need to be etched but undergoes the sputtering and the annealing phases only and permits to perform an in-situ XPS depth-profiling of the Sb position.

4.3.1 Capping Layer's Removal

The samples were grown at Paul Drude Institut (PDI) by Raffaella Calarco's group and were capped with silicon nitride (Si_3N_4) to avoid the exposure of the material to the atmosphere (that would lead to the surface oxidation) and keep the Germanium Telluride surface clean.

On the second generation of samples, an analysis through an Atomic Force Microscope (AFM) was performed. The figure 4.1(a) shows the AFM image of a sample with 30 nm Si_3N_4 capping layer on 73 nm GeTe. The surface is not continuous and holes are evident. The panel 4.1(b) shows the depth profile of the sample and permits a dimension evaluation of the holes: some of them are $30 - 40$ nm deep. The silicon nitride layer is bored, therefore is not capable of completely prevent from the surface oxidation and other contaminations.

The procedure capable of removing the capping layer is wet etching and it is described in sec. 3.5. The etching rate is about 2 nm/min, but an over-etching is suggested to remove any residue of Si_3N_4. In the case of a 30 nm capping layer, the sample has to be kept in solution for about 20 minutes.

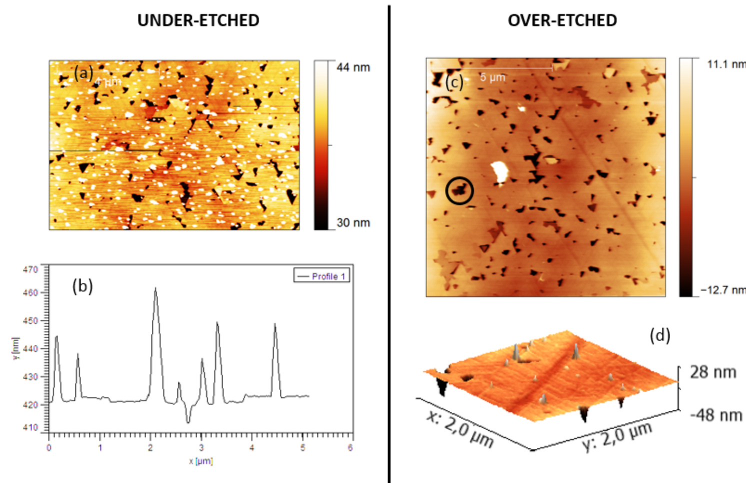

Figure 4.2: AFM imaging on samples with 73 nm of $GeTe$ and 30 nm of Si_3N_4. (a) 10 x 6.5μm^2 image of the surface after 9 minutes of wet etching. The silicon nitride residues are imaged as bright points on the GeTe surface. (b) Depth profile of (a) surface; the RMS value is 6 nm while the flat zones roughness is $0.3 - 0.5$ nm. (c) 10 x 10μm^2 surface image of a sample from the same substrate after a longer wet etching time: 20 minutes almost remove the capping layer. The RMS value is about 4 nm and the one of the flat zones is 0.5 nm. (d) 3D image of the surface corresponding to panel (c).

The wet etching does not affect too much the GeTe layer (we monitored the stoichiometry repeating the experiment with different wet etching times).

AFM imaging was employed to check the surface after the chemical process. The figure 4.2 illustrates the importance of a correct etching process by comparing the surface obtained from two different etching times: the fig. 4.2(a) corresponds to a 9 minutes etching, while the surface in fig. 4.2(c) has been taken after a 20 minutes etching. The first one has residues of Si_3N_4 on the surface, while the second one is almost clean.

The surface in fig. 4.2(c) is not uniform and presents holes with depth of around 40 nm, meaning that the GeTe layer is partially bored. Our hypothesis is that the silicon nitride is present only on the Germanium Telluride and it is not capable of filling the holes in the GeTe layer. In some cases the holes reach the silicon substrate. This fact means that the GeTe layer does not grow layer-by-layer, but it is compatible with layer-plus-islands or islands growth. The optimization of the growth is beyond the work of this thesis and will be done by R. Calarco and coworkers on the basis of the meaningful results of the present work. This will imply the search of different substrates with respect to Si (111) in order to minimize the lattice mismatch (i.e. Si (111) vicinal surfaces or other materials).

A closer look to the resulting surface with the AFM on a smaller area permits to show another important feature of the Germanium Telluride samples' surfaces: as shown in figure 4.3, we can clearly identify domains with a symmetry compatible to the predicted one of the GeTe (111) surface. In fact, the triangular symmetry reflects the one of the hexagonal lattice expected from the crystallographic structure.

4.3.2 Surface Recovery

After the capping layer's removal, a second phase of the preparation is necessary to recover the ideal ordered and clean surface used in theoretical calculation and hence to permit spectroscopic analysis and epitaxial growth of overlayers and heterostructures. To obtain a recipe we performed several studies entirely based on the LASSE system (see section 3.1). Samples are mounted on a Cu shuttle suitable for the insertion in the UHV system.

The preparation procedure has been optimized by X-ray Photoemission Spectroscopy (XPS, see sec. 3.4) and Low Energy Electron Diffraction (LEED, sec. 3.3). The procedure for surface recovery is done by sputter-

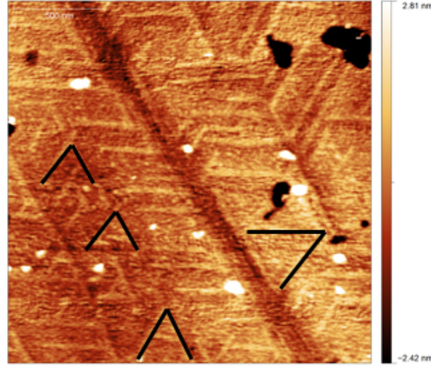

Figure 4.3: 2 x 2μm^2 AFM image of a sample with 73 nm $GeTe$ and 30 nm Si_3N_4 after wet etching. Black lines have been drawn as a guide for the eyes to show the presence of triangular domains.

ing and annealing and each cleaning step is followed by the analysis of the stoichiometry, contaminants and surface quality. To determine the starting point, after the wet etching and the insertion in the UHV environment, we collect the first XPS spectra: the surface presents very high level of carbon (25% with respect to normalized GeTe intensity) and oxygen (55% with respect to normalized GeTe intensity). A lack of germanium is observed with respect to tellurium: $Ge_{0.45}Te_{0.55}$.

Sputtering A sputtering process with Ar$^+$ ions can be used to reduce the carbon and oxygen presence on the surface.

An example of the surface contaminants' analysis by XPS is present in fig. 4.4. In this kind of analysis the Al-Kα line (photon energy: 1486.67 eV) is usually preferred as source instead of the Mg-Kα one (photon energy: 1253.67 eV) because results in a higher intensity.

The C 1s peak is represented in fig. 4.4(c). To evaluate the percentage of C (and other peaks later on), we use a quantitative analysis based on intensity of each peak. The intensity of a core level peak is given by

$$I(E_B) \propto \sigma T \lambda N(E_B) \tag{4.1}$$

where σ is the cross section of the atom at the peak binding energy, T is the transmission of the electron analyzer, λ is the mean free path of

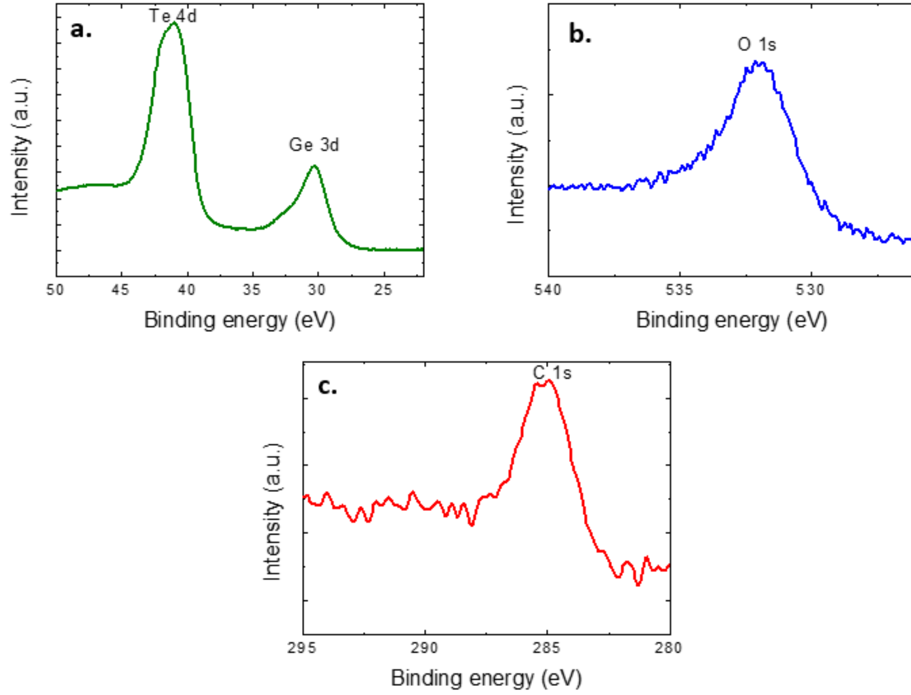

Figure 4.4: XPS (Al-Kα) chemical analysis on GeTe after 30 min of sputtering at 700 eV. The peaks of Te 4d and Ge 3d (a), O1s (b) and C1s (c) are represented. From figure (a) it is possible to deduce the stoichiometry of the sample by evaluating the ratio between the intensity of Te 4d peak and Ge 3d peak, both normalized to their cross sections and transmission coefficients. In this case the stoichiometry is $Ge_{0.47}Te_{0.53}$.

the electron and $N(E_B)$ is the number of states at that particular binding energy. N is the quantity we are interested in and it is the real bit of information to consider in the peaks' comparison.

The carbon and oxygen contamination's percentage is calculated through the ratio

$$\frac{N_{C1s/O1s}}{N_{GeTe}} = \frac{(I/(\sigma T))_{C1s/O1s}}{(I/(\sigma T))_{GeTe}} \tag{4.2}$$

where I are the intensities of the peaks (defined as the integrated area of the measured peaks after background subtraction).

The fig. 4.4(a) shows the Ge3d and the Te4d peaks with binding energies of 30.3 eV and 41 eV, respectively (both peaks are shifted from the

theoretical value by 1 eV, probably because of a charging of the sample). On germanium peak, a shoulder can be distinguished: this effect derives from the partial oxidation of Ge. In fact, the germanium oxides (GeO and GeO_2) are known to form two satellite peaks at higher binding energies with respect to the Ge 3d peak [12]. The chemical shift is due to the change in energy of the core levels in an atom when the latter is involved in a chemical bond.

In fig. 4.4(b) the measured O 1s peak is present at 532 eV binding energy (instead of 531 eV due to the presence of 1 eV shift, as the other peaks). This confirms the high oxidation level of the surface observed in Ge 3d peak (fig. 4.4(a)).

Another evaluation about the oxidation of the surface is performed by the analysis with Mg-Kα line ($h\nu = 1253.67$ eV) of the Ge 3d peak.

Thanks to the higher resolution of the Mg-Kα line with respect to the Al one, it is possible to resolve the three peaks as shown in fig. 4.5. The ratio between the area of the GeO (GeO_2) oxidized peak and the total Ge 3d area gives the percentage of oxidized germanium.

The effect of a sputtering treatment on the contaminants' percentages is presented in fig. 4.6 as a function of the sputtering time. No linear trend is deductible, therefore an etching rate cannot be determined.

The stoichiometry's analysis is performed through the calculation of the ratio

$$\frac{N_{Ge}}{N_{Te}} = \frac{(I/(\sigma T))_{Ge}}{(I/(\sigma T))_{Te}} \tag{4.3}$$

where I_{Ge} is the intensity of the Ge 3d peak and I_{Te} is the one of the Te 4d peak. The XPS peaks are shown in fig. 4.4(a).

The stoichiometry after wet etching is $Ge_{0.45}Te_{0.55}$. The sputtering procedure does not substantially change their relative content (even if a faster rate for Te would be predicted on the basis of the higher cross section for the sputtering, due to the higher atomic number).

The sample's surface is at this point very disordered. Furthermore the sputtering process has led to the thinning of Germanium Telluride layer. This fact has to be avoided, therefore the sputtering time should be minimized. Unluckily, as long as the contaminants' percentages have high values,

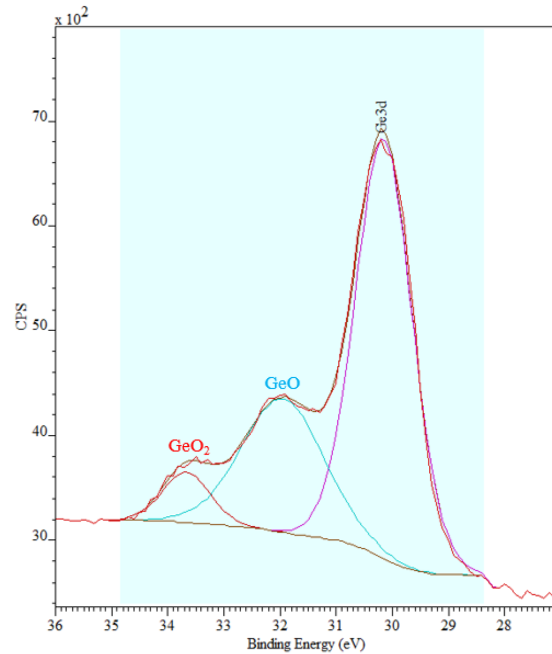

Figure 4.5: XPS (Mg-Kα) Ge 3d peak. The two oxidation states are visible and the peaks are deconvolved. The chemical shifts are 3.2 eV for GeO_2 and 1.6 eV for GeO. The latter shift value differs from the one seen on germanium [12].

sputtering cannot be avoided.

Annealing The *annealing* is a procedure that consists in bringing the sample to high temperature in order to allow contaminants to evaporate and surface order to recover. In fact, the temperature's increase is capable of providing to the contaminants' atoms the kinetic energy required to escape from the surface.

Furthermore, the thermal energy is exploited by the germanium and tellurium atoms to overcome the diffusion barrier and to find the lower energy's configuration, recovering the surface order. An ordered surface is fundamental for:

- **ARPES measurements**: the band structure can be measured only in ordered systems;
- **Fe/MgO growth**: the growth of spin injection (or detection) struc-

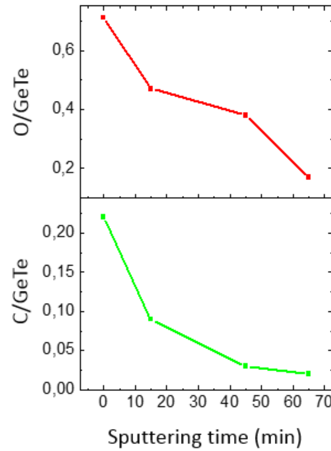

Figure 4.6: Ratio between the intensities (normalized to the cross section and the transmission coefficient) of O 1s and C 1s peaks and the intensity of Ge 3d + Te 4d versus the sputtering time. The sputtering energy is 700 eV and the incident angle is 60°.

tures on semiconductors needs ordered interfaces to permit overlayers to grow epitaxially and to minimize the scattering events that could cause the spins to flip.

Another result of the annealing is the desorption of tellurium and accordingly the stoichiometry unbalances in favour of germanium. Therefore, the annealing optimization should consider:

- the desorption of carbon and oxygen;
- the evaporation of tellurium;
- the surface ordering.

The optimization of the annealing temperature is necessary and has been done while checking the appearance and the quality of the LEED pattern and the stoichiometry as a function of the temperature. The figure 4.7 resumes the result of this optimization plotting on the same graph of the germanium and tellurium intensities and the presence/absence of the LEED pattern versus the annealing temperature.

At 250°C the LEED of Germanium Telluride appears and the stoichiometry is kept around 50%. With the increasing of the temperature, the sto-

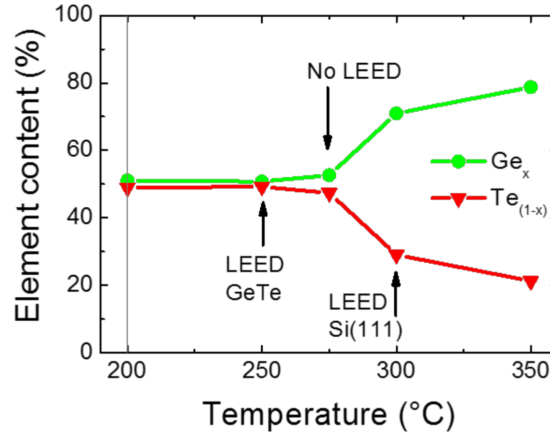

Figure 4.7: From the relative intensity of Te 4d and Ge 3d peaks in the XPS spectra it is possible to obtain the element content (%) within Ge_xTe_{1-x}. The clear tendency is the evaporation of Te that leaves a Ge-rich film.

ichiometry gets worse: at 275°C Te desorbs quickly and the GeTe(111) LEED disappears, while at 300°C a LEED appears again but is the one of the Si(111) surface. In fact, XPS indicates that GeTe is gone and only silicon substrate remains.

The optimum temperature for annealing is therefore 250°C, but the procedure requires much attention because the temperature window in which the LEED can appear with the right stoichiometry is very narrow (less then 30°C).

LEED If the surface has been recovered, the LEED presents a particular pattern (section 3.3). From the LEED figure it is possible to deduce the *Wigner-Seitz* cell of the surface lattice.

The calculated surface lattice is shown in figure 4.8. We considered the lattice of a zinc-blende unit cell and plotted the (111) surface. The theoretical first Brillouin zone [13] (as depicted in the left panel of fig. 4.8) reflects the direct lattice symmetry (the crystal structure has been taken into account without considering the rombohedral distortion of GeTe). From the reciprocal space's image of the surface it is possible to deduce the surface Wigner-Seitz cell. It is hexagonal and the two not equivalent directions are evidenced. The surface Wiegner-Seitz cell's orientation has to be compared with the bulk one: the hexagon on the right side has the same orientation of

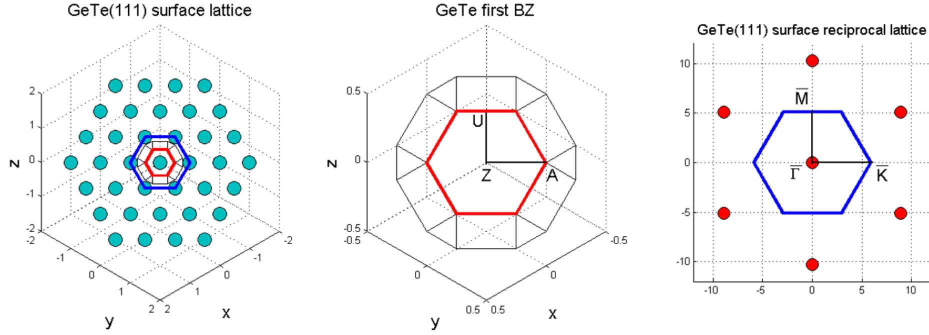

Figure 4.8: From left to right: zinc-blende (111) surface lattice in which the hexagonal symmetry is evidenced; theoretical bulk first Brillouin zone: the (111) surface is in red and not equivalent high symmetry directions ZA and ZU are shown; the surface reciprocal lattice and the deduced Wigner-Seitz cell: not equivalent directions $\bar{\Gamma}\bar{K}$ and $\bar{\Gamma}\bar{M}$ are shown. We underline that the $\bar{\Gamma}\bar{M}$ ($\bar{\Gamma}\bar{K}$) surface direction is equivalent to the ZU (ZA) bulk direction.

the hexagon in central image. This fact implies that the surface $\bar{\Gamma}\bar{K}$ direction overlaps with the bulk ZA direction. It has to be taken into account in the fittings with surface and bulk bands in the section 4.5.

In fig. 4.9 the measured LEED pattern is shown and the Wigner-Seitz cell is deduced. It is important to consider that what is visible from the LEED is the surface cell. In fact, the surface sensitivity of electrons at these energies make them an ideal tool to directly visualize the reciprocal space of the surface 2D lattice corresponding to GeTe(111) surface. The notation for the surface reciprocal lattice is the same as the one in fig. 4.8 and is different from the bulk one.

4.3.3 Antimony Content Analysis

The solution to the rotational domains' problem was obtained by R. Calarco and co-workers thanks to the addition of antimony in the chamber during the growth. The Sb acts as buffer layer in order to favour the growth on the silicon substrate. In fact, the interface between the Si substrate and the GeTe layer is abrupt and does not foster the ordered growth of Germanium Telluride.

This fact can create some complications. First, GeTe can turn into a different material, called GST ($Ge_2Sb_2Te_5$). This material has interesting features (it is studied for the implementation in phase change memories) but

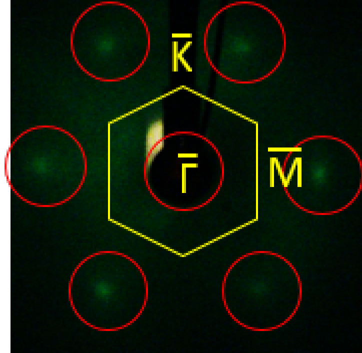

Figure 4.9: LEED diffraction figure on a GeTe sample (taken at 114 eV). The diffraction points are evidenced by red circles and the Wigner-Seitz cell of the surface is illustrated. It is possible to distinguish the two not equivalent directions $\bar{\Gamma}\bar{K}$ and $\bar{\Gamma}\bar{M}$ according to the surface nomenclature.

does not satisfy the properties we are looking for.

An analysis about the content and position of Sb in GeTe samples is important to understand its effects on the devices' physics. This is performed by studying the Sb 3d double peaks (due to the spin-orbit splitting) as shown in figure 4.10.

The third generation of samples (the one with thinner capping layer, see table 4.1) permits to remove the silicon nitride in UHV conditions by sputtering without the need of chemical etching. The procedure consists in series of sputtering processes and photoemission spectroscopies. After every sputtering the surface is checked and the quantity of silicon nitride is estimated by evaluating the resulting intensity of silicon 2p and nitrogen 1s peaks together. When this value approaches the zero, the capping layer has been removed.

The third panel from the top in fig. 4.11 shows the linear trend of the silicon nitride intensity. The initial signal of antimony is not detectable, meaning that the Sb is not present at the surface.

The annealing treatment causes the antimony to rise towards the surface as shown in the first panel of fig. 4.11. This fact implies that there is another condition in determining the annealing process. In fact, the high temperature induces antimony to interdiffuse. Therefore, the annealing is performed at 250°C till the LEED pattern appears, in order to avoid excessive antimony interdiffusion.

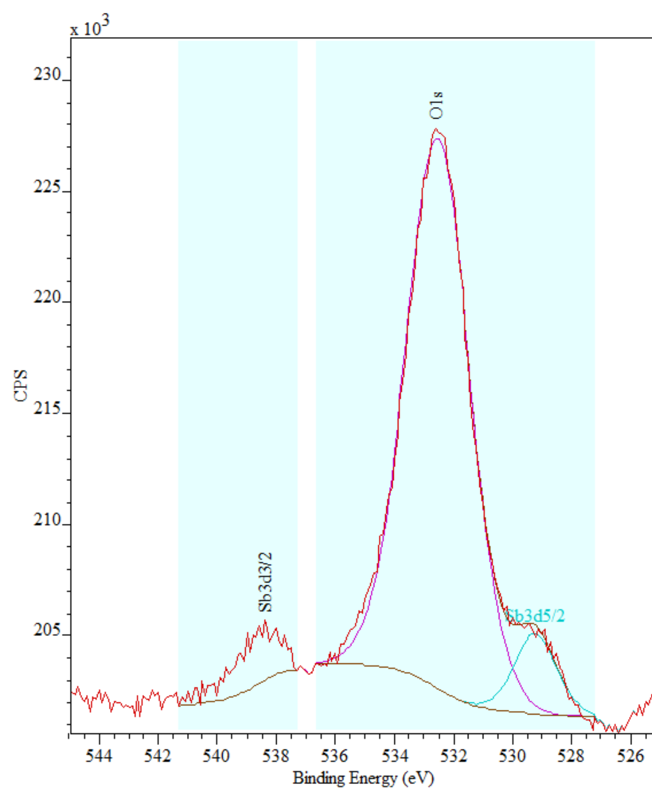

Figure 4.10: O 1s, Sb 3d 3/2 and 5/2 peaks obtained by Mg-Kα XPS analysis on a GeTe sample. The Sb peaks are partially covered by the oxygen one. The percentage of oxidation is about 15% and the antimony contamination is 0.37% with respect to Ge and Te intensities.

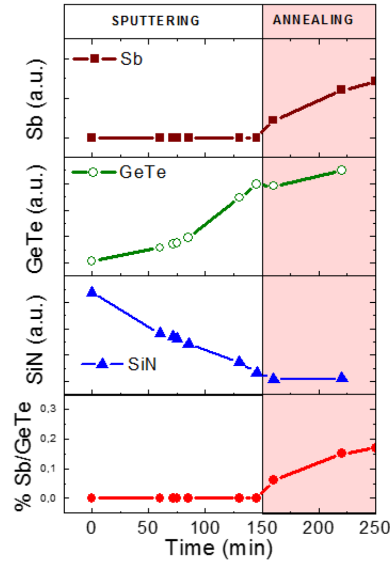

Figure 4.11: Intensity of Sb 3d, Ge 3d + Te 4d, Si 2p + N 1s peaks and percentage of Sb content with respect to GeTe. We gradually removed the Si_3N_4 capping layer (within 150 min of sputtering in UHV) and then we proceeded with thermal treatments in order to obtain a good surface. Only after the annealing at 250°C, a small Sb 3d peak appears in the XPS spectrum. The Sb content is limited to fraction of percent even after very long thermal treatments and always increases with the annealing time (and temperature).

In this analysis another meaningful conclusion can be deduced about the oxidation level. The surface is oxidized even if the capping layer is removed in UHV conditions. This fact is probably due to the very high density of holes in the silicon nitride layer (as seen in fig. 4.1): the capping layer is not capable of covering efficiently the Germanium Telluride substrate, thus the GeTe layer oxidizes in atmosphere.

4.4 Ferroelectric Characterization

A preliminary measurement about the ferroelectric behaviour of GeTe have been performed in parallel to my work. For completeness, and due to the fact that this research is motivated by the potential possibility to drive the Rashba effect using ferroelectric polarization, a hint about ferroelectric measurement is given. A brief study was performed with *Agilent* 5600 AFM on a sample annealed and without capping layer by Prof. Riccardo Bertacco

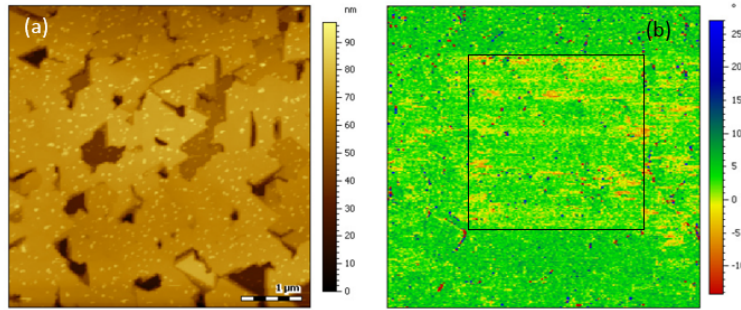

Figure 4.12: (a) Topography of the GeTe surface. Triangular domains and silicon nitride residues can be distinguished (see sec. 4.3). (b) Vertical piezo response phase after the application of 10 V bias to the square drawn in figure.

(NaBiS group).

The *Agilent* 5600 AFM is an Atomic Force Microscopy with Piezo-Force Microscopy (PFM) in order to sense the electric polarization of a surface or to write ferroelectric domains by applying a potential to the tip. The instrument can operate as Current AFM to obtain a map of the surface conductivity.

The figure 4.12(a) shows the topography of the GeTe surface: the surface map is the same as in sec. 4.3. Triangular domains are visible and there are holes in the Germanium Telluride layer. In spite of the preparation process, the surface presents residual Si_3N_4, visible as bright points on the surface.

The surface was scanned in a $3 \times 3 \mu m^2$ square with 10 V bias. Then, the surface was investigated with the PFM and the vertical phase was recorded. The Piezo-Force Microscopy is capable of sensing the ferroelectric polarization of a sample by evaluating the piezo-electric response of the sample. The polarization is measured as a phase difference between the applied voltage and the piezo-electric response. The result for the vertical phase's measurement is presented in fig. 4.12(b). The square is weak but recognizable, implying that a ferroelectric polarization is present. However, the phase does not draw a clear border, probably because more than one ferroelectric domain are present.

These results demonstrate the presence of writeable ferroelectric do-

mains. The most important result is the existence of a saturation value in the ferroelectric loop, that confirms the possibility of polarizing the sample. The polarization of GeTe should be the mean to control the spin texture of bands (see sec. 2.3).

The demonstrated ferroelectricity of the Germanium Telluride implies that the GeTe samples present a natural out-of-plane polarization. This polarization generates an electric field that allows the Rashba effect (see sec. 2.2) to occur and it k-splits the bands without an applied field (sec. 4.5.1). Furthermore, the presence of extended ferroelectric domains causes the k-splitted bands to have a finite spin polarization: it permits to measure a spin polarization of bands in the spin-resolved-ARPES (sec. 4.5.2).

4.5 ARPES on GeTe

In this section the investigation of GeTe bandstructure by means of Angular Resolved Photoemission Spectroscopy (ARPES) is described. The measurements have been performed on the first and the second generation of samples, i.e. both on samples with and without rotational domains. The different generations of GeTe samples have been already introduced in table 4.1.

In the present section, the first generation will be deeply analysed by Angle-Resolved PhotoEmission Spectroscopy (ARPES) (see sec. 3.4.2). Measurements have been carried out at the APE (Advanced Photoelectric Effect experiments) beamline at the Elettra Syncrothron of Trieste (Basovizza) (sec. 3.4.3), thanks to the active collaboration with G. Panaccione, I. Vobornick and J. Fujii.

The results that will be presented were mainly obtained during the beam-time performed in March 2013 on the first generation of GeTe samples. A second beam-time was performed in July on samples without rotational domains: measurements confirmed the conclusions obtained on the first generation. The presence of rotational domain does not affect so much the quality of the band structure (the run on the second batch has the same k and energy broadening of the bands).

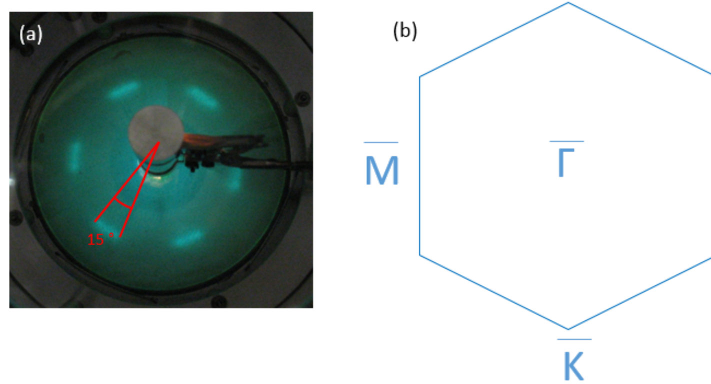

Figure 4.13: (a) LEED pattern of a GeTe sample in which rotation domains' presence is clearly distinguished. (b) First Brillouin zone of the surface reciprocal space corresponding to the LEED of panel (a).

4.5.1 Bands Dispersion Analysis

The surface was prepared as described in sec. 4.3. An annealing was performed until the LEED pattern appeared. The LEED at 92 eV is shown in fig. 4.13(a): the surface does not show any reconstruction but the presence of rotational domains is evident (see sec. 3.3). Each arch at the vertexes of the hexagon has an angular width of $15° \pm 1°$ and is made up of $4-5$ points. The size of the hexagon in the reciprocal lattice is, from a first calculation, 1.76 Å^{-1}, which in case of an hexagonal direct lattice would correspond to a parameter of the hexagon of 4.12 Å($a_{GeTe} = a \cdot \sqrt{2} = 5.83$ Å), in quite nice agreement with the literature (5.99 Å). The presence of rotational domains was noticed even by Calarco's group through X-ray diffraction (XRD) [44]. The XRD measurement gave as result a good epitaxial growth, although there are rotational domains within a 14° angular range, compatible with our LEED results.

Due to the sensitivity of the technique to the surface, the LEED pattern is the image of the reciprocal space of the film surface. So the Wigner-Seitz cell of the GeTe(111) surface can be obtained and is shown in fig. 4.13(c). Nonetheless, looking at the (111) direction, in sec. 4.3.2 the hexagonal Wigner-Seitz cell for the surface has been demonstrated to have the same orientation of the bulk hexagon. Therefore, the $\bar{\Gamma}\bar{M}$ ($\bar{\Gamma}\bar{K}$) surface direction corresponds to the ZU (ZA) bulk one.

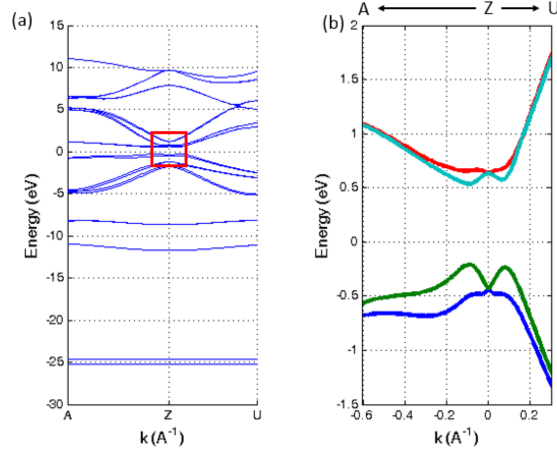

Figure 4.14: Theoretical bulk bands calculated by Picozzi et al. [13]. The fig. (b) is a zoom of the panel (a) in the very proximity of the Z point and around the zero of the energy (the Fermi level of the calculated system).

The bulk theoretical bands predicted by Silvia Picozzi *et al.* [13] near Z point and along ZU and ZA directions are shown in fig. 4.14. The figure 4.14(b) is a zoom that shows the k-splitting of the bands. Further details on theoretical bands are illustrated in sec. 2.3.

The Germanium Telluride band dispersions along ZU and ZA directions are really interesting in order to understand the effective importance of this material. In the following, we will refer to the surface directions $\bar{\Gamma}\bar{K}$ and $\bar{\Gamma}\bar{M}$ instead of the bulk ones ZA and ZU.

As described in sec. 3.4.2, the photons hit the sample that emits photoelectrons. Through the detection as a function of angle, it is possible to connect the angular dispersion with the wave-vector dispersion, thanks to the quasi-conservation of the parallel electrons' momenta.

Referring to figure 4.15 it is possible to express the kinetic energy of the photoemitted electron as:

$$E_{kin} = \frac{\hbar^2 k_{ext}^2}{2m^*} = \frac{\hbar^2 k_{ext,\|}^2}{2m^*(sin\theta)^2} \tag{4.4}$$

where m^* is the efficient mass of the electron and the relation $k_{ext} = k_{ext,\|}/sin\theta$ has been used.

Therefore, the parallel wave-vector is

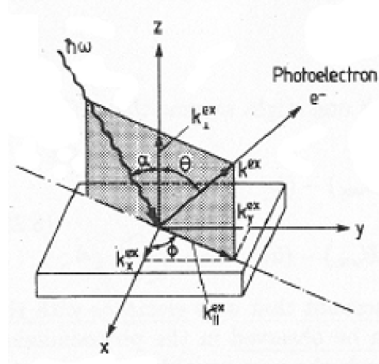

Figure 4.15: Geometry of the ARPES experiment.

$$k_{ext,\|} = \frac{\sqrt{2m^{*}E_{kin}}}{\hbar} sin\theta \tag{4.5}$$

The most interesting part of the bands is the zone around the Z point where bands Rashba splitting is maximum at the top of the valence band. Therefore it is necessary to find the correct photon energy capable of probing this zone.

The normal emitted electrons are required to correspond to the Z point in the Brillouin zone, with $k = (0, 0, k_{\Gamma Z})$. No immediate conservation relation on k_z is valid, as explained in section 3.4.2, because of the unknown value of the inner potential of the crystal. Therefore, it is necessary to measure the band structures at different photon energy. Changing this energy corresponds to sweep in $k_{\perp}$ thanks to the energy conservation; the relation is:

$$k_{\perp} = \frac{\sqrt{2m(E_{kin} - V_0)}}{\hbar} \tag{4.6}$$

where E_{kin} is the electron kinetic energy and V_0 is the inner potential.

Starting from the surface lattice parameter for Germanium Telluride (4.13 Å) it is possible to deduce the ΓZ distance as 0.867 Å^{-1}. A photoemitted electron coming from the Z point must have a perpendicular-to-plane wave-vector that is an odd multiple of the distance $k_{\Gamma Z}$ (a wave-vector that is an even multiple of $k_{\Gamma Z}$ indicates electrons coming from the L point of the Brillouin zone).

The kinetic energy of the emitted electrons can be expressed as

$$E_{kin} = h\nu - E_B - \Phi \tag{4.7}$$

where Φ is the work function (of 4.3 eV), E_B is the binding energy of the electrons and $h\nu$ is the photon energy. If we consider the binding energy of the photoemitted electrons equal to 1 eV (to be confirmed by experimental evidences) and the photon energy equal to 22.2 eV, therefore the kinetic energy is 16.9 eV. Now, the external perpendicular-to-plane wave-vector in eq. 4.6 can be determined supposing a reasonable value for the inner potential (according to S. Picozzi *et al.*): $V_0 = 9$ eV, resulting in 2.61 Å^{-1}.

Three times the calculated ΓZ distance corresponds to 2.6 Å^{-1}, that is almost the same as the $k_\perp$ value for electrons with 1 eV binding energy, an inner potential of 9 eV and photon energy equal to 22.2 eV. This theoretical result will be compared with the experimental one.

The experiment consists in using different photon energies and analysing the electrons that are photo-emitted near the normal direction. Electrons emitted along the normal direction originate from a point of the ΓZ line. The Z point is reached when the valence band is as close as possible to the Fermi level of the film (binding energy $E_B = 0$) because the valence band maximum (VBM) is in Z (see fig. 4.14(a)). The photon energy sweep is presented in figure 4.16: in the colour scale white means high density of states, therefore the bandstructure is resolved on a black background. The Fermi level can be easily distinguished as an abrupt cut of the spectrum at high kinetic energy. In every panel of fig. 4.16 (each one of them corresponds to a particular photon energy), the measured band dispersions are taken along the $\bar{\Gamma}\bar{M}$ direction (see fig. 4.13(c) for a better understanding of the geometry). From figure 4.16, 22.5 eV appears to be the photon energy we are looking for, very similar to the value predicted by theoretical calculations (22.2 eV).

This first analysis already provides important information. The valence band in Z is cut by the Fermi level (see fig. 4.16 for $h\nu = 22.5$ eV), inhibiting the complete vision of the Rashba splitting. This behaviour is probably due to a degenerate p-doping of GeTe (other considerations about the doping level can be found in sec. 4.7).

Furthermore, it is evident that all the pictured bands disperse with the

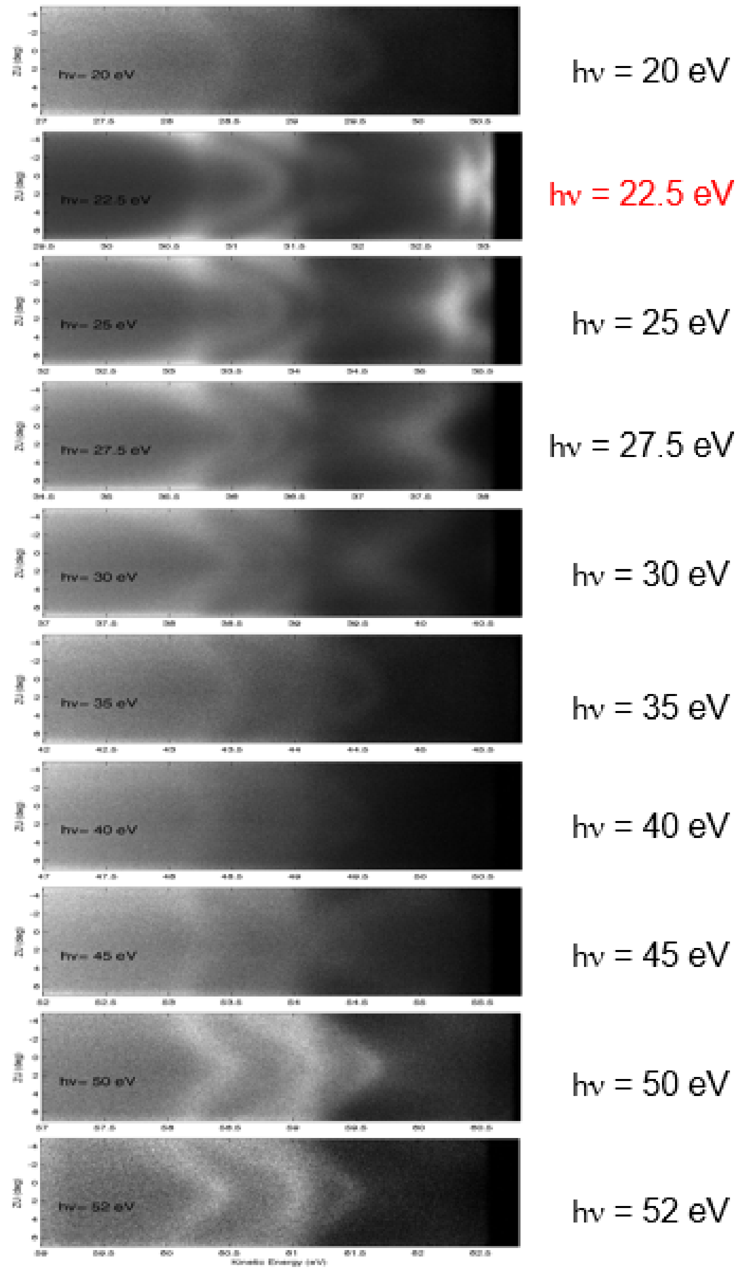

Figure 4.16: Measured band dispersion for a GeTe sample at different photon energies. For $h\nu = 22.5$ eV the maximum of the valence band is as close as possible to the Fermi level of the crystal (corresponding to binding energy $E_B = 0$).

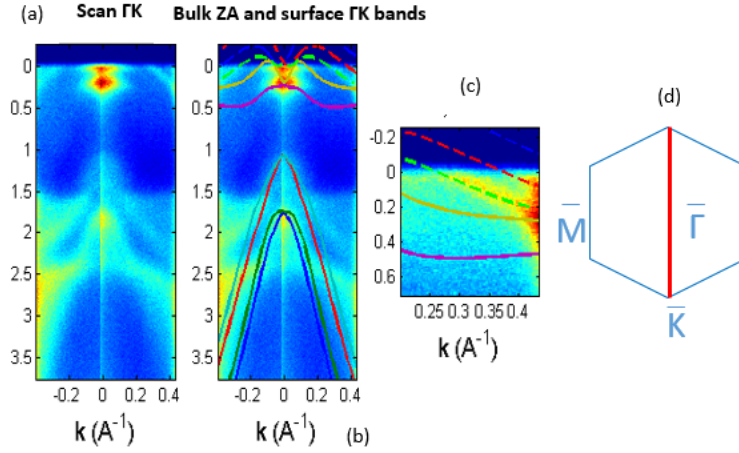

Figure 4.17: (a) Experimental angular dispersion for $h\nu = 22.5$ eV in the $\bar{\Gamma}\bar{K}$ direction. (b) Theoretical surface (dashed line) and bulk (solid line) bands (ZA direction) [13] for GeTe. (c) Enlargement of the surface entering bands that shows the correspondence with theoretical calculations. (d) The red line shows the $\bar{\Gamma}\bar{K}$ direction (on the W.-S- cell) in which the angular dispersion is measured.

changing of the incident photon energy, i.e. they disperse in $k_\perp$. These bands cannot be *true surface states*, the position of which (in terms of binding energy) does not depend on the photon energy, i.e. they do not disperse in $k_\perp$. Therefore the observed bands are *bulk states* or *surface resonance states*. A surface resonance state originates when a surface state, that is function of the only $k_\parallel$ coordinates, cuts a bulk state for a particular $k_\perp$. In this case, the electron of the surface band is able to propagate into the crystal and the resulting state is a mixing of the surface state and the bulk one.

Once the photon energy has been established, the band dispersion around the Γ point has been measured. The resulting angular dispersion along $\bar{\Gamma}\bar{K}$ direction is shown in fig. 4.17(a).

First of all a splitting in momentum seems to appear but the situation is not clear because of the Fermi level cut. Furthermore, there is quite good agreement with the upper surface theoretical bands originating from Te surface states: the panel 4.17(c) shows a detail of the bands' fitting with theoretical calculations for surface states (dashed lines).

In fig. 4.17(b) the bulk states along the ZA direction fit well the deeper

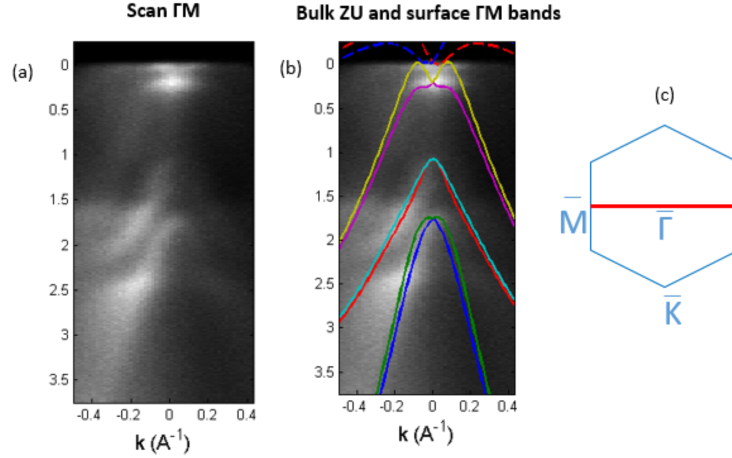

Figure 4.18: (a) Angular dispersion for $h\nu = 22.5$ eV in the $\bar{\Gamma}\bar{M}$ direction. (b) Theoretical surface (dashed line) and bulk (solid line) bands (ZU direction) [13] for GeTe. (c) The red line shows the $\bar{\Gamma}\bar{M}$ direction (on the W.-S- cell) in which the angular dispersion is measured.

bands (blue, green, red and light blue solid lines) but not perfectly the upper states (yellow and purple solid lines). However, in fig. 4.17(c) two weak bands close to the E_F seem to follow the calculated bulk ones (yellow and purple solid lines), although their intensity is much lower with respect to the surface bands.

The band dispersion along surface $\bar{\Gamma}\bar{M}$ direction (bulk ZU) is shown in figure 4.18(a). The $(0; +k_{\|,max})$ zone is darker with respect to the left half of the carpet because the average number of counts has changed, probably due to a calibration problem of the pixels intensities of the CCD camera. This problem can be resolved by exploiting the bands symmetry with respect to the Γ point, therefore by mirroring the left half of the carpet, as shown in fig. 4.19.

We note that the fitting with ZU bulk bands is extremely good, while the upper surface states are not seen because they stay above the Fermi level of the degenerate p-doped GeTe. The good fitting of the bulk bands confirms that the orientation of the W.-S. cell for bulk is the same as the surface one, as already said in sec. 4.3.2. The enlarged band in fig. 4.19 is clearly a bulk state and represents the accordance with theoretical calculations.

In both the $\bar{\Gamma}\bar{K}$ (bulk ZA) and $\bar{\Gamma}\bar{M}$ (bulk ZU) directions, the broaden-

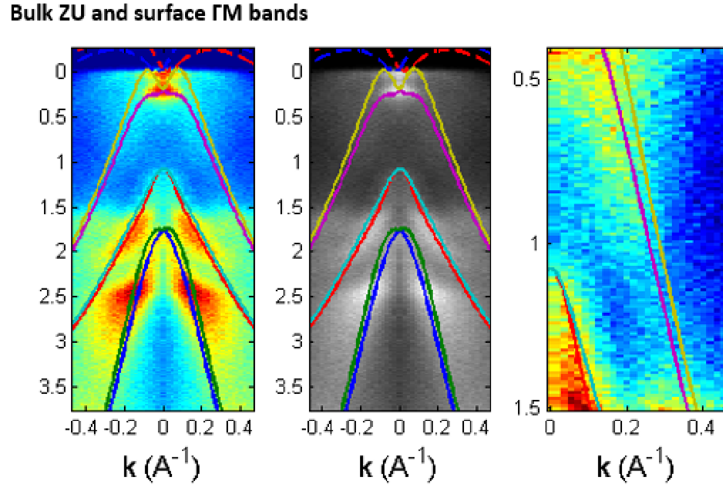

Figure 4.19: Angular dispersion for $h\nu = 22.5$ eV in the $\bar{\Gamma}\bar{M}$ direction. The left half of image 4.18 has been mirrored. The panel on the right shows an enlargement of a bulk band.

ing of deeper bulk bands is probably due to the presence of low dispersing surface states (shown in fig. 4.20). The electrons are not generated from a single atomic layer, but their escape depth permits them to pass through inner layers. The presence of a surface cause the bands to bend, therefore at the depth from which photoelectrons come from, the bands' configuration is different layer by layer. The measured band dispersion is the average value in the out-of-plane direction of the probed band structures.

The whole of the scans collected in an ARPES experiment (a 3D space, counts as a function of energy, ($k_{\Gamma K}$ and $k_{\Gamma M}$)) can be used to plot constant energy maps (*Fermi surface maps*) in the ($k_{\Gamma K}, k_{\Gamma M}$) plane. These maps are pictured in fig. 4.21: they consist in iso-energy cuts of the bands and give an idea about the symmetry of the crystal and the topology of the bands, in particular about the Rashba k-splitting of the bands.

The three energy cuts in fig. 4.21 are taken at different binding energies (0.1 eV, 0.25 eV and 0.4 eV) as shown on the calculated and measured carpets. They present 6-fold symmetry, as predicted from the theoretical band structure of Germanium Telluride. Focusing the attention on panel (a) in fig. 4.21, a hole in the center of the image can be clearly distinguished.

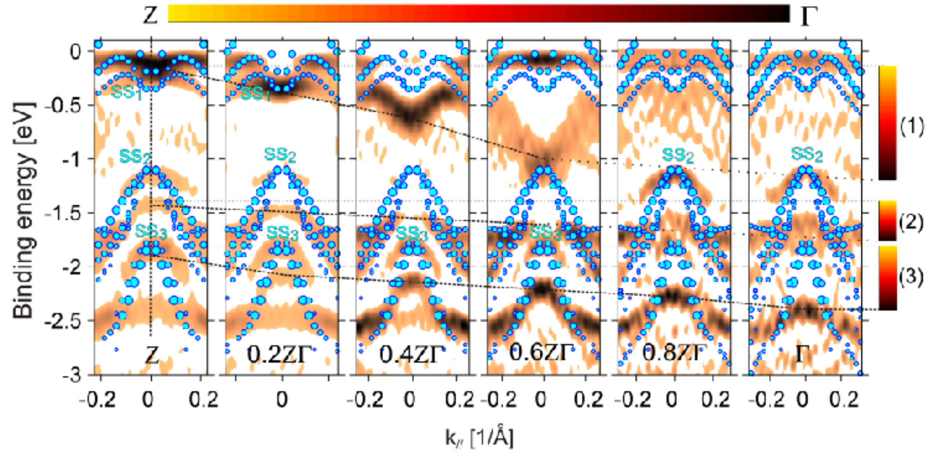

Figure 4.20: GeTe calculated bands through one step photoemission calculations by J. Minar (LMU, Münich) (dots in figure) and measured surface bands (originating from Te states), represented with a second derivative filter. The surface states are shown to disperse changing the position along the ΓZ direction.

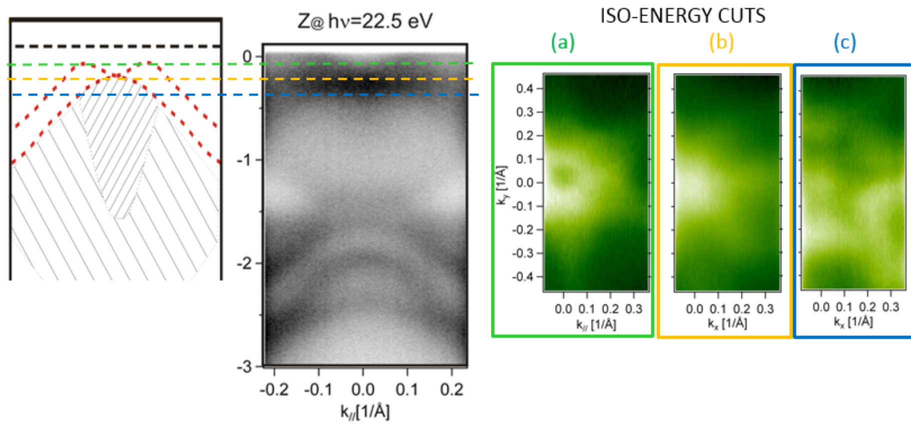

Figure 4.21: Photon energy: $h\nu = 22.5$ eV. Three iso-energy cuts are presented at (a) 0.1 eV, (b) 0.25 eV and (c) 0.4 eV binding energy. The energy cuts are represented as dashed lines on both the calculated and the measured carpet (at APE in July 2013). The band structure in the measured carpet is black on white background.

This feature is due to a k-splitting of the bands, as evidenced in fig. 4.21: the (a) energy cut sees two maxima symmetrically translated with respect to the center in every direction of the reciprocal space. Therefore, an experimental prove of the k-splitting of bands has been presented; the other ingredient for the presence of Rashba effect (i.e. the spin character of the k-splitted bands) will be investigated in the next section.

4.5.2 Spin-Resolved ARPES

An additional beam time on Germanium Telluride performed at Paul Scherrer Institute (PSI) in Villigen (Switzerland), in February 2014, by Dr. Christian Rinaldi (NaBiS) and Dr. Juraj Krempasky (PSI), aimed at resolving the spin character of the bands, in order to obtain a complete experimental proof of the Rashba effect in GeTe. Even if the author did not participate directly to the beamtime, the main and preliminary result is illustrated here to confirm the spin character of the k-splitted bands. In particular, we will show in this section the rotation of the spin around the Rashba field in a constant energy Fermi surface map.

The spin-resolved photoemission spectroscopy is a probing technique capable of measuring the spin polarization of the photo-emitted electrons. It is performed through instruments that can sense the spin polarization of an electron beam. In order to reach this aim, *Mott spin detectors* [45] installed in the hemispherical analyzer at the COPHEE beamline of SLS (Swiss Light Source at PDI) have been employed.

A Mott detector exploits the double scattering experiment proposed by Mott in 1929: through a scattering with a high-Z material (that presents large spin orbit coupling) at high kinetic energies, the scattered beam suffers a spin dependent angular deflection from which the spin polarization can be deduced. In fact, for electron beam's spins perpendicular to the incident plane (i.e. the plane defined by the incident and the scattered electron wavevector) the right-left asymmetry generated by the spin-dependent scattering event is proportional to the initial out-of-plane polarization of the electron beam. In order to sense even the in-plane spin direction, there are typically two detectors at different inclinations. The COPHEE beamline has two Mott spin detectors, each one equipped with gold foils. A scheme of the experimental set-up for spin-resolved ARPES is shown in fig. 4.22. Just one of the Mott detectors was operating in the beamtime period and only the

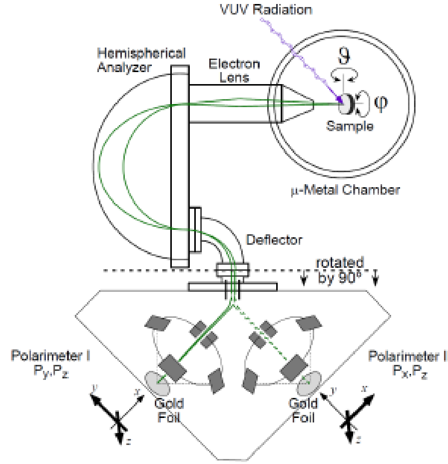

Figure 4.22: Experimental set-up of the COmplete PHotoEmission Experiment (COPHEE) at the Surface and Interface Spectroscopy beamline at the Swiss Light Source. The photoemitted electrons first pass a hemispherical electrostatic analyser and are then accelerated through an electron lens with chopper, onto the Mott detectors. This configuration allows for the simultaneous detection of the binding energy, momentum and all three components of the spin polarization vector of the electron [14].

in-plane spin polarization have been analyzed (the working analyzer is the one on the right in fig. 4.22).

The spin asymmetry can be calculated as

$$A = \frac{N_L - N_R}{N_L + N_R} \tag{4.8}$$

where N_L (N_R) is the number of electrons counted in the detectors in the left (right) side. From the spin asymmetry, the spin polarization can be determined as

$$P = \frac{A}{S} \tag{4.9}$$

where S is the Sherman function [14] that corresponds to the asymmetry that will be measured for a fully spin-polarized electron beam.

The GeTe samples have been demonstrated to have extended ferroelectric domains with a natural out-of-plane polarization in sec. 4.4: therefore the k-splitted bands are predicted to have a finite spin polarization without applying an electric field. Firstly, the experiment consists in the collection

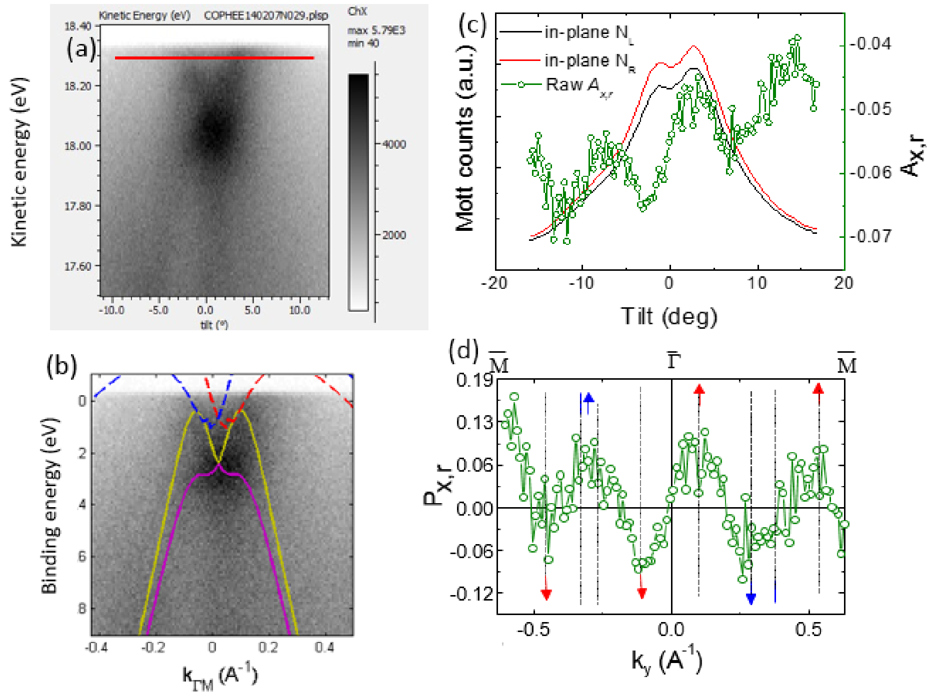

Figure 4.23: (a) Measured carpet along the $\bar{\Gamma}\bar{M}$ direction. The red solid line indicates the kinetic energy of the spin-resolved measurements. (b) Fitting with theoretical surface (dashed lines) and bulk (solid lines) bands along the $\bar{\Gamma}\bar{M}$ direction. (c) Mott counts (left and right) of the in-plane component of the photoelectrons' spins and raw spin asymmetry (calculated as the difference of the Mott counts). (d) In-plane polarization deduced from (c) after background subtraction. The arrows indicate the in-plane spin direction.

of a carpet (band dispersion as a function of k and binding energy) along $\bar{\Gamma}\bar{M}$, shown in fig. 4.23(a). From a comparison between the collected carpet and the ones from previous samples (see sec. 4.5.1) we can state that in this case the preparation of the surface with the annealing leads to a stoichiometry very close to 1:1 with a lower p-doping. In this way, we are able to see/probe a wider part of the valence band (the position of the Fermi level is higher than the VBM), as depicted in fig. 4.23(b).

According to the bands fitting in sec. 4.5.1, we are investigating both the surface bands and the bulk bands. In this section, we will firstly focus our attention on surface bands crossing the Fermi level. We fix the photon energy to 22.5 eV and collect electrons at $E_{kin} = 18.3$ eV, as illustrated in fig. 4.23(a) (red line cutting the carpet at zero binding energy). We analyse with Mott detectors the spin of photoemitted electrons as a function of the emission angle. In fig. 4.23(c), the red and black solid lines represent the counts on the right and left channels of the Mott detector for in-plane component of the spin. Instead, the green line indicates the spin asymmetry ($A_{x,y}$, see eq. 4.8), i.e. the difference between the left and the right counts. After proper background subtraction to the raw asymmetry $A_{x,y}$, we end up with the spin asymmetry illustrated in fig 4.23(e). These results confirm the presence of in-plane spin polarization due to Rashba effect in surface states of Germanium Telluride.

In figure 4.24 is illustrated the result of the in-plane spin population in Germanium Telluride. The x and y axis are the tilt and the polar angle respectively (ϕ and θ in fig. 4.22), while x_{Mott} is the axis on which the Mott detector project the in-plane component of the spin (the positive or negative spin polarization in the lateral panels of fig. 4.24 are determined by their direction with respect to this axis). Let's focus the attention on the point 1 in fig. 4.24. The Mott detector see the projection of the in-plane spin component along its axis (x_{Mott} in figure) and read a positive value. According the Hamiltonian (eq. 2.5) the Rashba energetic term is proportional to $(\boldsymbol{\sigma} \times \mathbf{k}) \cdot \hat{z}$ and has its minimum value when $\boldsymbol{\sigma} \times \mathbf{k}$ is orientated in the negative direction of the z axis. Therefore, the spin and the wave-vector of the electron have to be perpendicular: the positive value of the in-plane spin component detect by the Mott analyzer determines uniquely the in-plane spin direction for the point 1 as the one shown in fig. 4.24. This analysis is valid for other points on a circumference in the reciprocal

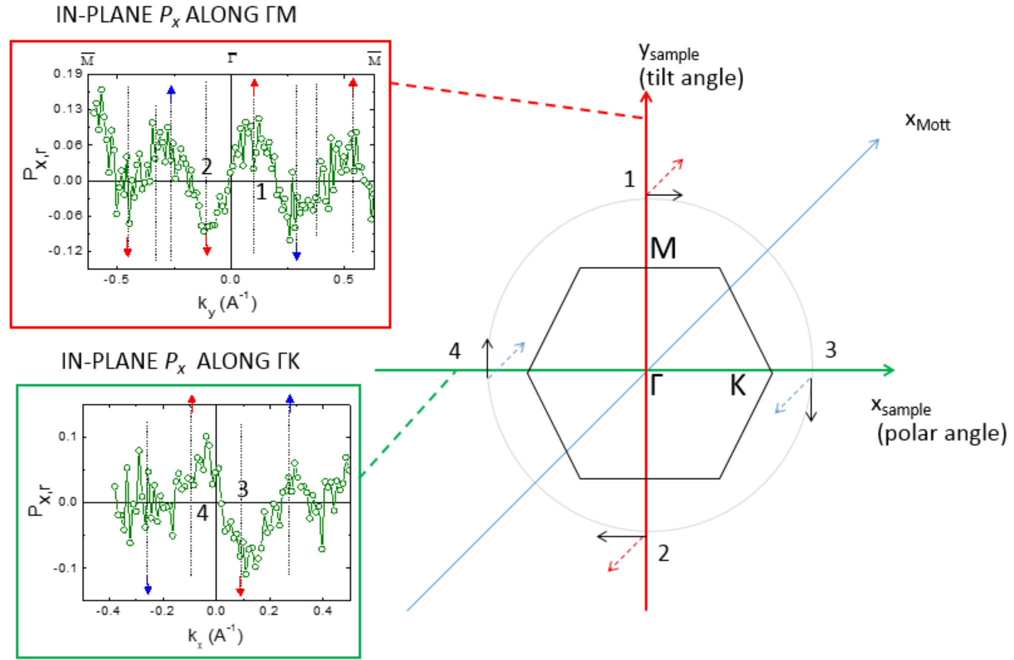

Figure 4.24: Summary image of the spin-resolved PES in GeTe at 18.30 eV kinetic energy, with 22.5 eV photon energy. The in-plane spin asymmetry measured with a single Mott can already demonstrate the rotation of spin in the iso-energy cut of the surface states that are crossing the Fermi level.

space (as the one in fig. 4.24): the spin have a different orientation in each point, and two opposite momenta must have two opposite spins. Therefore, a rotation of the spin in the Fermi surface map has been observed.

In conclusion, the theoretical surface states well fit the measured bands and a surface Rashba effect seems to be present. The rotation of the surface spins has been observed and is compatible with the predicted Rashba theory, confirming the spin character of the bands for Germanium Telluride. The bulk bands need to be investigated to evidence Rashba splitting. A preliminary analysis (data not shown) at $E_B = 5$ eV already reveals the presence of the spin rotation even for bulk bands. Therefore GeTe presents a clear bulk Rashba effect.

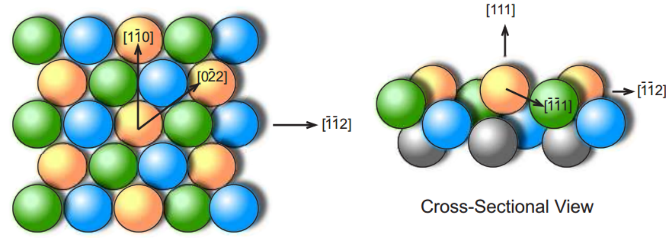

Figure 4.25: Iron b.b.c. (111) surface (by E. Hasselbrink, Universität Duisburg-Essen): the hexagonal structure can be distinguished.

4.6 Fe Growth on GeTe Surface

The fabrication of a spintronic device based on Germanium Telluride (and FERSC, in general) could face the growth of ferromagnetic layers on its surface. For example, the spinFET concept in sec. 2.5 needs two FM electrodes on the GeTe channel, with an insulating barrier in between to solve the problem of conductivity mismatch in spin injection in case of low doped GeTe [21].

In LASSE (see section 3.1) the iron growths has been performed by Molecular Beam Epitaxy (sec. 3.1.2). Our main intent was to prove the feasibility of an epitaxial growth and to check the orientation and the quality of the Fe layer grown onto GeTe.

GeTe has a rock-salt structure (slightly deformed) and in the (111) direction presents a 6-fold symmetry [13]. Iron is a body-centered cubic system (b.c.c.) with a lattice parameter $a = 2.87$ Å. However, we would like to understand how the growth of iron can take place on the GeTe(111) hexagonal surface, for which the in-plane lattice parameter is $a_{GeTe,\|} = 4.12$ Å. We notice that the (111) plane of the BCC lattice shows the same hexagonal symmetry (see fig. 4.25) and the in-plane lattice parameter ($a_{Fe} \cdot \sqrt{2} = 4.06$ Å) is very close to the one of the FERSC. Fe (111) can hence growth on GeTe (111), owning the same symmetry and with a relatively small (+1.5%) lattice mismatch ($\epsilon = (a_{GeTe} - a_{Fe})/a_{GeTe}$), resulting in a tensile strain on the thin film.

Fe is grown by MBE on the GeTe(111) freshly and well-ordered surface, prepared by wet etching and UHV annealing at 250°C, as described in sec.

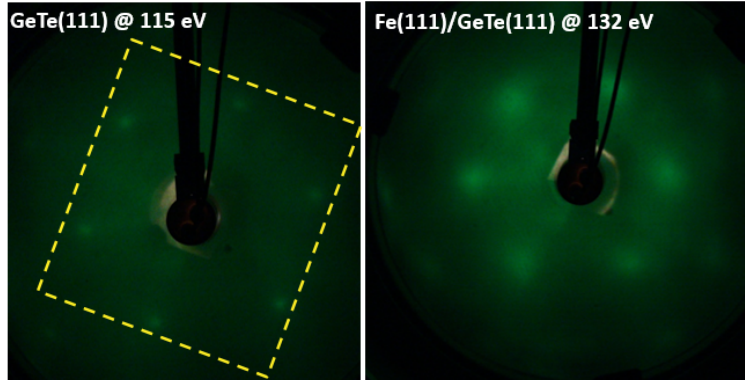

Figure 4.26: Comparison between the LEED figures of a GeTe sample virgin (left) and with 2.5 nm Fe (right). In the image on the left the dashed line shows the sample profile.

4.3.2. The evaporation rate was about 3 Å/min. After the deposition, an annealing for 20 min at 250°C is necessary to obtain a LEED pattern from the iron layer. Fig. 4.26 shows in panel (a) the LEED pattern of the GeTe(111) surface and in panel (b) the pattern after iron growth and annealing. The presence of the iron LEED pattern confirms the epitaxial growth of Fe on GeTe.

A sample was grown with 2.5 nm Fe on GeTe (second batch, see tab. 4.1). The Germanium Telluride surface was prepared by the capping layer removal through wet etching (sec. 4.3.1) procedure and annealing treatment (at 250°C, see sec. 4.3.2).

The obtained LEED pattern has been shown in fig. 4.26 and presents hexagonal symmetry. Then the sample was analysed with a Vibrating Sample Magnetometer (VSM), that is an instrument capable of measuring the magnetization versus applied magnetic field of a material. The VSM measurement (of the coercive field in function of the in-plane angle) in figure 4.27 shows the in-plane magnetization with a trace of 6-fold symmetry.

On the basis of the work of Cantoni *et al.* [46], we tried to demonstrate the possibility of obtaining particular magnetic anisotropies suitable for the implementation in spintronic devices by the surface preparation process. Therefore, a 60° sputtering procedure (the ions beam hits the surface sample

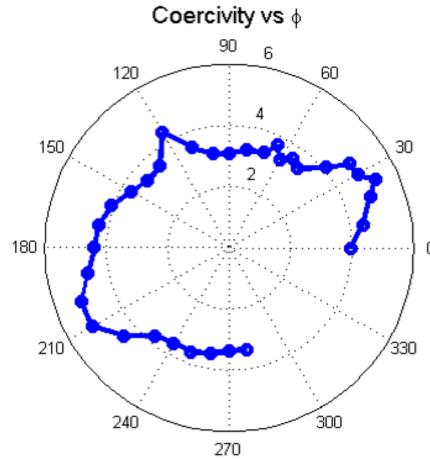

Figure 4.27: Polar plot of the coercive field of Fe(2.5nm)/GeTe. The uniaxial anisotropy is not present if the sputtering at grazing incidence is not employed to clean the surface.

with a 60° inclination with respect to the surface plane) was implemented in the surface preparation of another Germanium Telluride sample. The sputtering process is capable of creating a step surface, vicinal to the (111) plane. This generates an uniaxial anisotropy, imposed to the iron 6-fold symmetry [47]. The 2-fold symmetry emerges from VSM measurement in fig. 4.28, where θ is the in-plane angle with respect to the cleavage direction. From fig. 4.28(a) it is possible to deduce the magnetic behaviour of the Fe layer, because one direction shows a more "squared" hysteresis loop, corresponding to the *easy axis* [26]. The easy axis direction is perpendicular with respect to the step direction [47].

The fig. 4.28(b) shows the polar plot of the magnetization remanence. It is perfectly in agreement with the hysteresis loops shape analysis and recognises $\theta = 0°$ as the easy axis while $\theta = 90°$ represents the hard axis of magnetization.

In my thesis I have demonstrated that it is possible to prepare good GeTe (111) surfaces and to epitaxially grow iron thin films on top of it, paving the way to FERSC based spintronic devices (leading to spin injection, spin detection and spin-transfer torque experiments). Moreover, we demonstrate that a clever use of sputtering can be exploit to engineer the anisotropy of magnetic layers onto the FERSC surface.

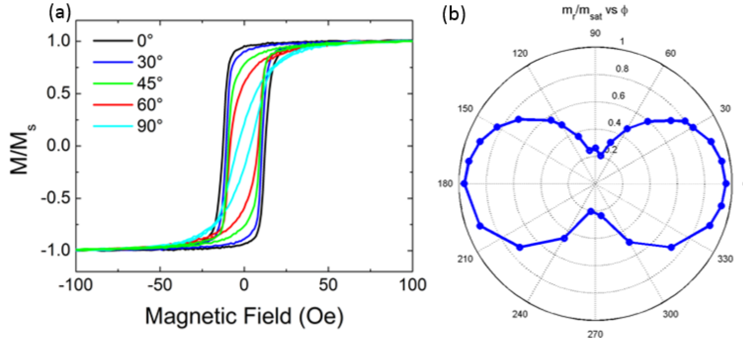

Figure 4.28: (a) Hysteresis loop for the Fe(2.5nm)/GeTe sputtered (60°) sample with the magnetic field applied at an angle θ with respect to the cleavage side. $\theta = 0°$ represents an easy axis, while $\theta = 90°$ is a hard axis. (b) Polar plot of the magnetization remanence. A uniaxial anisotropy is present along the cleavage side (0°).

The possibility of engineering 2-fold symmetry in iron thin layes grown on FERSCs can be exploited in the device realization. In fact, a patterned layer with different anisotropy's axes can be imagined, where the domains react differently to a magnetic field in a given direction. Furthermore, the Germanium Telluride, through its spin currents, is capable of injecting spins into electrodes (through spin Hall effect, see sec. 2.5); the effect on the iron magnetization will be different depending on the magnetic anisotropy direction with respect to current and magnetic field.

4.7 Hall Measurements

The ARPES results in sec. 4.5 have already given information about the Fermi level position, from which the kind of carriers and the doping level can be deduced.

As discussed in section 3.7, the Hall effect can give both information, through analysis of the longitudinal and transversal voltages in function of the external out-of-plane magnetic field.

A GeTe sample (65 nm GeTe on slightly p-doped silicon substrate that belong to the second generation in tab. 4.1) was prepared as described in sec. 4.3 and was exposed to air without capping layer. Furthermore, the GeTe thickness is assumed not to change significantly upon sputtering and annealing.

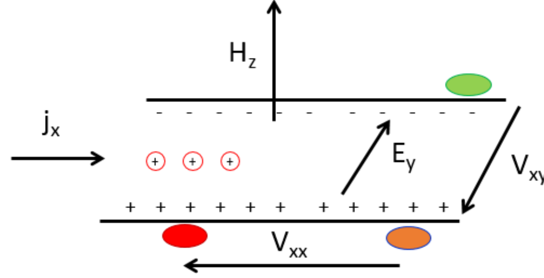

Figure 4.29: Sketch of the Hall effect measurement. The current is considered as composed by holes only.

The Hall contacts were fabricated through silver paste and their dimensions (1×1 mm^2) are much smaller than the sample's ones. Then, the sample was mounted into the Cryogenic cryostat (1.6 K minimum temperature, 7.5 T maximum magnetic field, see sec. 3.7) with the normal to the sample's surface oriented as the cryostat's magnetic field axis. The current value was fixed and the magnetic field's sweep was performed.

Two curves were considered: V_{xx} and V_{xy}. The measuring geometry is shown in fig. 4.29.

The longitudinal resistance is defined as $R_{xx} = \frac{V_{xx}}{j_x}$ for every magnetic field value. At 1.6 K, the silicon substrate is definitely insulating, then the current flows only in the Germanium Telluride layer. From the R_{xx} value, it is possible to obtain the resistivity of GeTe: $\rho_{GeTe} \approx 5 \cdot 10^{-4}\Omega$cm. At room temperature (RT, 300 K), the silicon resistivity is $\rho_{Si} = 1 - 10\Omega$cm, according to the substrate's datasheet. The R_{xx} value does not change much, suggesting that the current is still flowing only in the GeTe layer. In fact, the high conductivity of Germanium Telluride is due to the high doping level (to be confirmed by the following measurements) with respect to the substrate; a high doped semiconductor has a resistivity behaviour with temperature similar to a metal. This means that the conductivity of the GeTe layer remains approximately constant, allowing us to neglect the current's flow in the substrate.

Now, we focus on the R_{xy} curve. ARPES data (section 4.5) suggest a picture where the Fermi level lies inside the valence band. Therefore, holes are considered as the main carriers involved in the current. This assumption

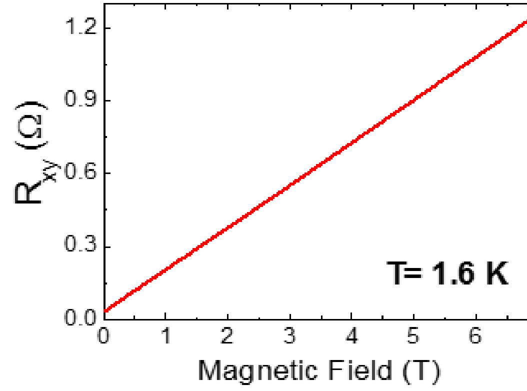

Figure 4.30: R_{xy} vs (positive) magnetic field at 1.6 K. The result is a straight line with positive slope.

will be verified in the following.

Refer to the vectors' directions shown in fig. 4.29. It is possible to define a *transverse resistance* as $R_{xy} = \frac{V_{xy}}{j_x}$. With increasing out-of-plane magnetic field in the geometry considered above, the positive charged carriers should accumulate on one side and the V_{xy} value should increase. In other words, if the situation depicted in figure 4.29 were true, the $d(R_{xy})/dH$ would be positive.

The measured curve is presented in fig. 4.30. The slope is positive, thus the conduction seems to be driven mostly by holes. On the contrary, if the current were composed by electrons, the accumulation of charge would be opposite with respect to the case depicted in fig. 4.29, therefore the slope $d(R_{xy})/dH$ would be negative.

The Hall coefficient R_H is expressed through the equation

$$R_H = t\frac{dR_{xy}}{dH_z} = \frac{1}{pe} \tag{4.10}$$

where t is the maximum depth in which the current flows, e is the electron charge and p is the holes' concentration. p is exactly the doping level we are looking for.

The coefficient 4.10 is the expression used in the metals' case. Germanium Telluride is a strongly doped semiconductor in which the conduction is determined mainly by just one kind of carriers. From eq. 4.10, the doping level can be determined as $p \approx 5 \cdot 10^{20} cm^{-3}$. The large holes' concentration

validates the approximation in eq. 4.10.

Both the data (resistivity from R_{xx} and doping level from R_{xy}) indicate that Germanium Telluride is almost "metallic". Furthermore, the electrical transport has been demonstrated to be performed by holes.

4.8 Spin Lifetime in Germanium

To acquire the necessary know-how to measure the spin lifetime in semiconductors, part of my thesis work has been devoted to the realization of non-local measurements on standard Ge as a reference case. The choice of the CoFeB/MgO/Ge system has been done to exploit the long-term knowledge of this system in the NaBiS group [48] [49].

In the future, the same kind of investigation will be performed on FERSCs (in particular on GeTe).

Two kinds of measurements are performed on germanium samples:

- *non-local* measurements, in order to determine the spin diffusion length in the semiconductor;
- *Hanle effect* measurement, in order to obtain spin lifetime in three terminals geometry.

The sample was grown by magnetron sputtering (see section 3.2) following the recipe: 50 W soft etching on germanium, 500°C annealing, MgO deposition (2.5 nm), 500°C annealing, CoFeB deposition (10 nm), 200°C annealing and tantalum deposition (20 nm, as a capping layer). 2.5 nm MgO have been demonstrated to be the optimized value for the realization of tunnelling contacts [50]. In fact, around this thickness the $R \cdot A$ value grants the maximum tunnelling efficiency.

The lithography (see sec. 3.6) we performed consists in a four terminals geometry of contacts for both non-local and Hanle measurements (as described in sections 1.4.4 and 1.4.3).

On the micro-fabricated sample we performed:

1. non-local measurements at room temperature in four terminals geometry;
2. a spin lifetime characterization in temperature through Hanle effect measurements in three terminals geometry.

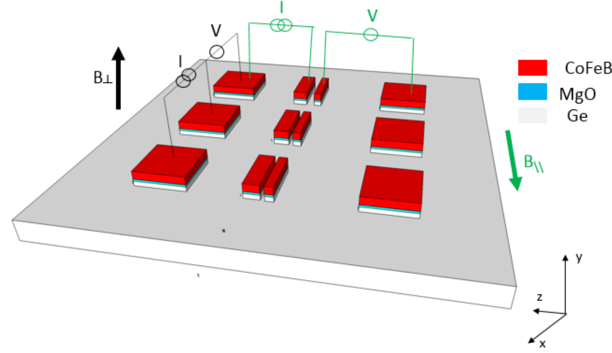

Figure 4.31: Map of CoFeB/MgO contacts on Ge. The arrangement for non-local measurements is shown in green, while the three terminals arrangement is shown in black, as used for Hanle effect measurements.

The spin lifetime and the spin diffusion length at room temperature has been compared (through the diffusion constant) between them and with the findings of Rinaldi *et al.* [49], confirming a 100 ps of spin lifetime for electrons at room temperature.

The geometry was adapted for both the measurements by considering only some terminals as shown in fig. 4.31.

Four terminals non-local measurements Non-local measurements at room temperature are performed in the four terminal geometry reported in fig. 4.31, according to the concept described in sec. 1.4.4. The lithography on the sample defines different structures (each one formed by four terminals) that differ among them only for the distance between the central electrodes.

Sweeping the magnetic field permits to obtain the ΔV_{NL} values. The fig. 4.32 shows three different gap distances between the central electrodes. The longer the distance between the central electrodes, the smaller the non local voltage detected. The dependency is exponential (as stated by eq. 1.19 in sec. 1.4.4) and related to the characteristic length L_s (spin diffusion length) The fitting with an exponential proportional to $e^{\frac{-L}{Ls}}$ is represented by the red line. The deduced characteristic length is found to be 1.2μm: this value is compatible both with the literature [7] and with the previous result of NaBiS group [49].

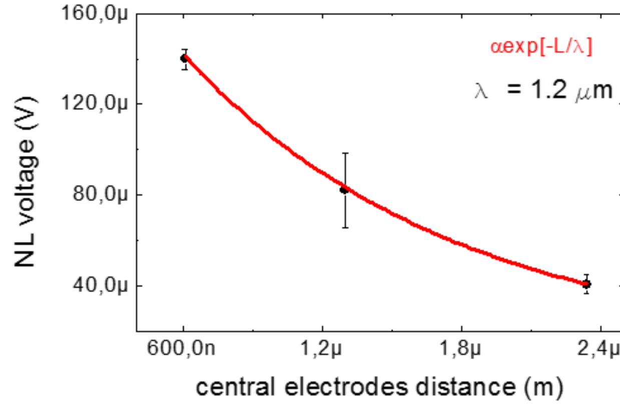

Figure 4.32: NL signal with respect to the gap between the central electrodes. The spin diffusion length (L_s) is extracted by fitting with an exponential with 1.2μm characteristic length.

Using the diffusion constant $D = 4 \cdot 10^{-4}$ m^{2}s^{-1} for intrinsic germanium, the spin lifetime is deduced in the order of 100 ps.

Three terminals Hanle measurements The set up employed for the measurements is described in sec. 3.8. Both the Hanle effect and the inverted-Hanle effect (see section 1.4) are investigated to identify the spin lifetime τ and to study the role of interfacial roughness (disordered magnetic moments and the effect of their stray field on τ).

We repeat the measurement of Hanle and inverted Hanle effect for several temperature (50 K- 400 K). At each temperature, the fit of the Hanle effect with a Lorentzian provides the value of the spin lifetime as illustrated in sec. 1.4. The figure 4.33 illustrates Hanle and inverted Hanle effect peaks for some temperatures. The deduced spin lifetime is around 151 ps at 50 K, compatible with literature value for spin lifetime measured in a sample with roughness in three terminals geometry [51] [5].

As described in sec. 1.4.2 the roughness of the surface can introduce a local magnetic field that causes spins' precession. The inverted-Hanle effect gives an indication about the interface's roughness [51] [5]: in fig. 4.33 the inverted-Hanle peak has a larger amplitude with respect to the Hanle one.

In the semiconductor Spintronics community, it is quite accepted (Jain *et al.* [52]) that the spin lifetime obtained by four and three terminal mea-

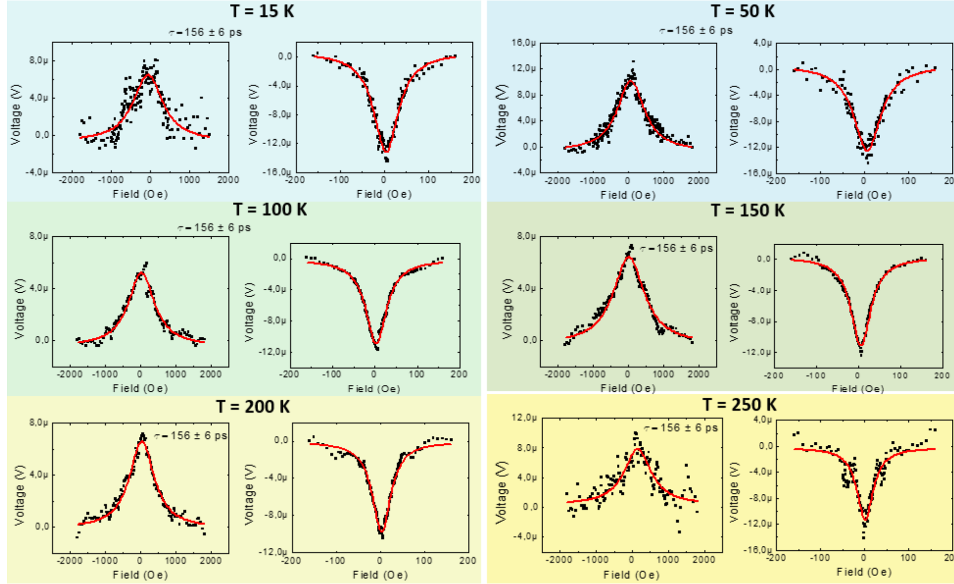

Figure 4.33: Hanle and inverted-Hanle peaks for different temperatures after linear background subtraction. The experimental data are presented as black points, while the Lorentzian fit is the red line.

surements is limited by the roughness at the interface (spurious magnetic moments). It follows that the measured spin lifetime is the one related to the interface roughness that, through a local random magnetic field, causes the Hanle curve broadening and the consequent underestimation of the spin lifetime. In fact, the precession of the spins is not only due to an intrinsic mechanism, but it also depends on the random magneto-static field introduced by roughness.

The temperature dependence of the spin lifetime (that has been deduced by three Hanle effect measurements) is shown in fig. 4.34(a). The lifetime seems to be poorly variable with temperature, coherently with Jain et al. [52] and it lays in the range between 120 and 160 ps. The explanation of this behaviour can be reached by considering the precession induced by the surface roughness as the dominant effect in the spin lifetime determination. The random local magnetic field does not depend on temperature, therefore the measured spin lifetime is approximately constant.

This fact can also explain the incompatibility of our spin lifetime (165 ps) with respect to 1 ns obtained in germanium by Zhou (at 4 K, grown by MBE) [7].

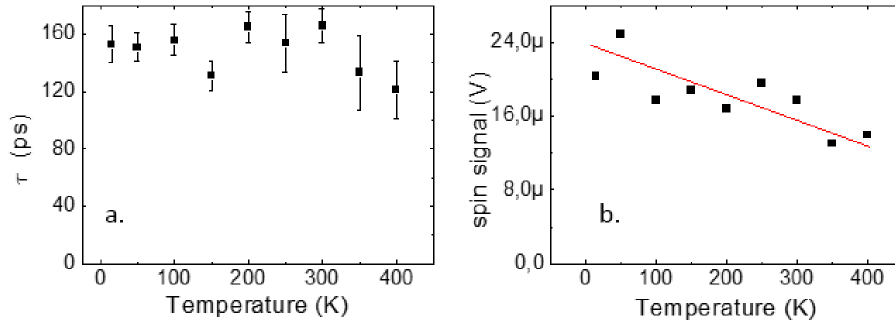

Figure 4.34: (a) Spin lifetime in function of temperature. The value seems to be poorly dependent on temperature with a mean value of 156ps. (b) Spin signal vs temperature: the linear trend is evidenced in red.

Furthermore, the agreement with Jain [52] is kept even in the spin signal, i.e. the sum of the Hanle and inverted-Hanle peaks' heights. The decreasing linear trend evidenced in fig. 4.34(b) is still under investigation.

The analysis performed on germanium through Hanle effect leads to some observations:

- the deduced spin lifetime (140 ± 10 ps) is underestimated with respect to the real one because of the strong effect of the local magnetostatic field induced by the surface roughness; a solution to this problem could be the growth by MBE because, with respect to sputtering, grants sharper interfaces;

- we must note that, in literature, there are some disagreements between the three terminals measurements' results and other kinds of spin lifetime measurements;

- the Germanium Telluride surface at the moment is not flat and uniform, therefore Hanle measurements would give poor information because of the expected strong influence of the roughness.

Thanks to this work the group acquires the necessary know-how to measure spin lifetime in semiconductors through an electrical method. In conclusion, the three terminals Hanle effect for spin lifetime measurements is not the best technique to adopt for Germanium Telluride characterization. The

four-terminals geometry for spin lifetime measurements have been demonstrated to be more reliable with respect to the three terminals geometry [6]. In fact, the results show that both methods are useful to extract the spin lifetime, but the three terminals Hanle measurement is more easily affected by the roughness dependence and other problems (accompanied charge current and electric field at the high temperature [6] [53] [3] [54]).

Conclusions and Perspectives

This thesis work has been devoted to the study of the FERSC (Ferro-Electric Rashba SemiConductor) material Germanium Telluride. Theoretical calculations predicted ferroelectricity and Rashba splitting at the same time in the same material, making it very attractive for an implementation of spin-orbitronic devices. Our measurements confirmed both the ferroelectric and the Rashba characters of the material and fixed preliminary results for a further development of GeTe-based heterostructures and devices. Here we summarize the main results obtained during the thesis.

Growth process In this thesis some growth issues have been faced and solved. The first batch of samples (see tab. 4.1) was affected by the presence of rotational domains as revealed by after-growth XRD and after preparation LEED. The solution to rotational domains problem was found by R. Calarco *et al.*: a buffer layer of Sb has been used between Si(111) and GeTe to accommodate the lattice mismatch. The interdiffusion of Sb during annealing has been studied and minimized through the optimization of the process.

Surface Preparation The development of an optimized preparation procedure was of fundamental importance for both spectroscopic studies (e.g. ARPES and S-ARPES investigation) and growth of spintronic heterostructures. A chemical wet etching procedure was optimized in order to remove the silicon nitride protective capping layer used for transferring samples from PDI to Politecnico di Milano or synchrotrons. Moreover, we performed a complete study of the annealing process intended to:

- remove contaminants (oxygen and carbon) from the surface;
- keep the stoichiometry of GeTe layer with a 50:50 proportion;
- order the surface (presence of a LEED) pattern.

Ferrolectricity The ferroelectric nature of the Germanium Telluride has been demonstrated through piezo-force microscope (PFM) measurements. The material presents ferroelectric domains with a spontaneous out-of-plane polarization (in the outward direction).

Band structure The angle resolved photoemission spectroscopy measurements permit to probe the band structure of Germanium Telluride. The predicted 6-fold symmetry has been confirmed through the observation of an hexagonal LEED pattern and by the iso-energy cuts of the ARPES collected band structure. The Rashba induced k-splitting was experimentally shown for surface and bulk states. A good accordance of theoretical calculations with measured surface and bulk bands have been shown. The spin-resolved ARPES measurements demonstrated the presence of spin polarized k-splitted bands. The analysis of spin-resolved data, partially reported in this thesis, already shows the rotation of the in-plane component of the spin around the Rashba field. Such a rotation is intimately related to the physics of the Rashba effect and is in good agreement with calculations. The position of the Fermi level indicates a high p-doping level.

Electrical measurements Hall measurements permitted to evaluate the conductivity and the doping level (and type) of the GeTe layers. The results confirmed the high p-doping level (10^{20} cm^{-3}) observed by ARPES and the resulting high value of conductivity. Furthermore, preliminary lifetime measurements were performed on germanium (as a well-know test case) in order to acquire the necessary know-how and prepare for future measurement on GeTe.

Ferromagnetic thin films growth on GeTe The thesis demonstrate the possibility to grow FM metals on FERSCs: we show that Fe(111)-oriented thin film can be epitaxially grown on GeTe(111) surface. This paves the way to: (i) an electrical control of magnetization through the injection of

a spin current into a FM; (ii) the feasibility of Fe (and Fe/MgO) electrodes for devices (i.e. spinFET); (iii) the use of GeTe as a channel/injector in STT-MRAM structures.

This thesis studied extensively the Germanium Telluride features and confirmed its high innovative and attractive potential. Furthermore, the actual feasibility of spin-orbitronic devices based on FERSCs has been demonstrated, paving the way to a fully electrical control of the spin texture into materials.

Bibliography

[1] H Jaffres and A Fert. Spin injection from a ferromagnetic metal into a semiconductor. *Journal of applied physics*, 91(10):8111–8113, 2002.

[2] Jörg Wunderlich, Byong-Guk Park, Andrew C Irvine, Liviu P Zârbo, Eva Rozkotová, Petr Nemec, Vít Novák, Jairo Sinova, and Tomás Jungwirth. Spin hall effect transistor. *Science*, 330(6012):1801–1804, 2010.

[3] Saroj P Dash, Sandeep Sharma, Ram S Patel, Michel P de Jong, and Ron Jansen. Electrical creation of spin polarization in silicon at room temperature. *Nature*, 462(7272):491–494, 2009.

[4] AT Hanbicki, S F Cheng, R Goswami, OMJ vant Erve, and BT Jonker. Electrical injection and detection of spin accumulation in ge at room temperature. *Solid State Communications*, 152(4):244–248, 2012.

[5] Saroj Prasad Dash, S Sharma, JC Le Breton, J Peiro, H Jaffrès, J-M George, A Lemaître, and R Jansen. Spin precession and inverted hanle effect in a semiconductor near a finite-roughness ferromagnetic interface. *Physical Review B*, 84(5):054410, 2011.

[6] LT Chang, W Han, Y Zhou, J Tang, IA Fischer, M Oehme, J Schulze, RK Kawakami, and KL Wang. Comparison of spin lifetimes in n-ge characterized between three-terminal and four-terminal nonlocal hanle measurements. *Semiconductor Science and Technology*, 28(1):015018, 2013.

[7] Yi Zhou, Wei Han, Li-Te Chang, Faxian Xiu, Minsheng Wang, Michael Oehme, Inga A Fischer, Joerg Schulze, Roland K Kawakami, and

Kang L Wang. Electrical spin injection and transport in germanium. *Physical Review B*, 84(12):125323, 2011.

[8] Mario Norberto Baibich, JM Broto, Albert Fert, F Nguyen Van Dau, F Petroff, P Etienne, G Creuzet, A Friederich, and J Chazelas. Giant magnetoresistance of (001) fe/(001) cr magnetic superlattices. *Physical Review Letters*, 61(21):2472, 1988.

[9] Takayuki Kawahara, Kenchi Ito, Riichiro Takemura, and Hideo Ohno. Spin-transfer torque ram technology: review and prospect. *Microelectronics Reliability*, 52(4):613–627, 2012.

[10] Silvia Picozzi. Ferroelectric rashba semiconductors as a novel class of multifunctional materials. *arXiv preprint arXiv:1312.0095*, 2013.

[11] JE Hirsch. Spin hall effect. *Physical Review Letters*, 83(9):1834, 1999.

[12] K Prabhakaran and T Ogino. Oxidation of ge (100) and ge (111) surfaces: an ups and xps study. *Surface Science*, 325(3):263–271, 1995.

[13] Domenico Di Sante, Paolo Barone, Riccardo Bertacco, and Silvia Picozzi. Electric control of the giant rashba effect in bulk gete. *Advanced Materials*, 25(4):509–513, 2013.

[14] J Hugo Dil. Spin and angle resolved photoemission on non-magnetic low-dimensional systems. *Journal of Physics: Condensed Matter*, 21(40):403001, 2009.

[15] G Radaelli, D Petti, E Plekhanov, I Fina, P Torelli, BR Salles, M Cantoni, C Rinaldi, D Gutiérrez, G Panaccione, et al. Electric control of magnetism at the fe/batio3 interface. *Nature communications*, 5, 2014.

[16] Luqiao Liu, Chi-Feng Pai, Y Li, HW Tseng, DC Ralph, and RA Buhrman. Spin-torque switching with the giant spin hall effect of tantalum. *Science*, 336(6081):555–558, 2012.

[17] NF Mott. The resistance and thermoelectric properties of the transition metals. *Proceedings of the Royal Society of London. Series A-Mathematical and Physical Sciences*, 156(888):368–382, 1936.

[18] A Fert and IA Campbell. Transport properties of ferromagnetic transition metals. *Le Journal de Physique Colloques*, 32(C1):C1–46, 1971.

[19] AG Aronov. Spin injection in metals and polarization of nuclei. *Jetp Lett*, 24(1):32–34, 1976.

[20] EI Rashba. Theory of electrical spin injection: Tunnel contacts as a solution of the conductivity mismatch problem. *Physical Review B*, 62(24):R16267, 2000.

[21] A Fert and H Jaffres. Conditions for efficient spin injection from a ferromagnetic metal into a semiconductor. *Physical Review B*, 64(18):184420, 2001.

[22] Aubrey T Hanbicki, BT Jonker, G Itskos, G Kioseoglou, and A Petrou. Efficient electrical spin injection from a magnetic metal/tunnel barrier contact into a semiconductor. *Applied Physics Letters*, 80(7):1240–1242, 2002.

[23] G Schmidt, D Ferrand, LW Molenkamp, AT Filip, and BJ Van Wees. Fundamental obstacle for electrical spin injection from a ferromagnetic metal into a diffusive semiconductor. *Physical Review B*, 62(8):R4790, 2000.

[24] DJ Monsma and SSP Parkin. Spin polarization of tunneling current from ferromagnet/al2o3 interfaces using copper-doped aluminum superconducting films. *Applied Physics Letters*, 77(5):720–722, 2000.

[25] X Jiang, R Wang, RM Shelby, RM Macfarlane, SR Bank, JS Harris, and SSP Parkin. Highly spin-polarized room-temperature tunnel injector for semiconductor spintronics using mgo (100). *Physical review letters*, 94(5):056601, 2005.

[26] Stephen Blundell. *Magnetism in Condensed Matter*. Oxford Master Series in Physics, 2001.

[27] YK Kato, RC Myers, AC Gossard, and DD Awschalom. Observation of the spin hall effect in semiconductors. *science*, 306(5703):1910–1913, 2004.

[28] Sergio O Valenzuela. Nonlocal electronic spin detection, spin accumulation and the spin hall effect. *International Journal of Modern Physics B*, 23(11):2413–2438, 2009.

[29] Michel Julliere. Tunneling between ferromagnetic films. *Physics Letters A*, 54(3):225–226, 1975.

[30] Stuart SP Parkin, Christian Kaiser, Alex Panchula, Philip M Rice, Brian Hughes, Mahesh Samant, and See-Hun Yang. Giant tunnelling magnetoresistance at room temperature with mgo (100) tunnel barriers. *Nature materials*, 3(12):862–867, 2004.

[31] T Valet and A Fert. Theory of the perpendicular magnetoresistance in magnetic multilayers. *Physical Review B*, 48(10):7099, 1993.

[32] WH Butler, X-G Zhang, TC Schulthess, and JM MacLaren. Spin-dependent tunneling conductance of fe— mgo— fe sandwiches. *Physical Review B*, 63(5):054416, 2001.

[33] M Bowen, V Cros, F Petroff, Albert Fert, C Martınez Boubeta, José Luis Costa-Krämer, José Virgilio Anguita, Alfonso Cebollada, F Briones, JM De Teresa, et al. Large magnetoresistance in fe/mgo/feco (001) epitaxial tunnel junctions on gaas (001). *Applied Physics Letters*, 79(11):1655–1657, 2001.

[34] S Ikeda, J Hayakawa, Y Ashizawa, YM Lee, K Miura, H Hasegawa, M Tsunoda, F Matsukura, and H Ohno. Tunnel magnetoresistance of 604% at 300 k by suppression of ta diffusion in cofeb/mgo/cofeb pseudo-spin-valves annealed at high temperature. *Applied Physics Letters*, 93(8):082508–082508, 2008.

[35] Supriyo Datta and Biswajit Das. Electronic analog of the electro-optic modulator. *Applied Physics Letters*, 56(7):665–667, 1990.

[36] T Jungwirth, V Novák, X Marti, M Cukr, F Máca, AB Shick, J Mašek, P Horodyská, P Němec, V Holỳ, et al. Demonstration of molecular beam epitaxy and a semiconducting band structure for i-mn-v compounds. *Physical Review B*, 83(3):035321, 2011.

[37] Robert J Cava, T Jungwirth, V Novák, X Martí, M Cukr, F Máca, AB Shick, J Mašek, P Horodyská, P Němec, et al. Viewpoint: A useful pyramid scheme. *Phys. Rev. B*, 83:035321, 2011.

[38] P Wadley, V Novak, RP Campion, C Rinaldi, X Marti, H Reichlova, J Železnỳ, J Gazquez, MA Roldan, M Varela, et al. Tetragonal phase

of epitaxial room-temperature antiferromagnet cumnas. *Nature communications*, 4, 2013.

[39] Silvia Picozzi. Ferroelectric rashba semiconductors as a novel class of multifunctional materials. *Frontiers in Physics*, 2(10), 2014.

[40] Victor M Edelstein. Spin polarization of conduction electrons induced by electric current in two-dimensional asymmetric electron systems. *Solid State Communications*, 73(3):233–235, 1990.

[41] K Ishizaka, MS Bahramy, H Murakawa, M Sakano, T Shimojima, T Sonobe, K Koizumi, S Shin, H Miyahara, A Kimura, et al. Giant rashba-type spin splitting in bulk bitei. *Nature materials*, 10(7):521–526, 2011.

[42] MI Dyakonov and VI Perel. Current-induced spin orientation of electrons in semiconductors. *Physics Letters A*, 35(6):459–460, 1971.

[43] R Bertacco, M Cantoni, M Riva, A Tagliaferri, and F Ciccacci. Epitaxial growth and characterization of layered magnetic nanostructures. *Applied surface science*, 252(5):1754–1764, 2005.

[44] Alessandro Giussani, Karthick Perumal, Michael Hanke, Peter Rodenbach, Henning Riechert, and Raffaella Calarco. On the epitaxy of germanium telluride thin films on silicon substrates. *physica status solidi (b)*, 249(10):1939–1944, 2012.

[45] Clifford Glenwood Shull, CT Chase, and FE Myers. Electron polarization. *Physical Review*, 63(1-2):29, 1943.

[46] M Cantoni, M Riva, R Bertacco, and F Ciccacci. Uniaxial magnetic anisotropies in fe films on single crystal and virtual ge (001) substrates studied with spin polarized inverse photoemission and moke. *Physical Review B*, 74(13):134415, 2006.

[47] Jun Ye, Wei He, Qiong Wu, Hao-Liang Liu, Xiang-Qun Zhang, Zi-Yu Chen, and Zhao-Hua Cheng. Determination of magnetic anisotropy constants in fe ultrathin film on vicinal si (111) by anisotropic magnetoresistance. *Scientific reports*, 3, 2013.

[48] M Cantoni, D Petti, C Rinaldi, and R Bertacco. Bandstructure line-up of epitaxial fe/mgo/ge heterostructures: A combined x-ray photo-electron spectroscopy and transport study. *Applied Physics Letters*, 98(3):032104, 2011.

[49] Christian Rinaldi, Matteo Cantoni, Daniela Petti, Andrea Sottocorno, Marco Leone, Nuala M Caffrey, Stefano Sanvito, and Riccardo Bertacco. Ge-based spin-photodiodes for room-temperature integrated detection of photon helicity. *Advanced Materials*, 24(22):3037–3041, 2012.

[50] M Cantoni, D Petti, C Rinaldi, and R Bertacco. Epitaxial growth of fe/mgo/ge (001) heterostructures. *Microelectronic Engineering*, 88(4):530–533, 2011.

[51] Kun-Rok Jeon, Byoung-Chul Min, Youn-Ho Park, Young-Hun Jo, Seung-Young Park, Chang-Yup Park, and Sung-Chul Shin. Effect of spin relaxation rate on the interfacial spin depolarization in ferromagnet/oxide/semiconductor contacts. *Applied Physics Letters*, 101(2):022401, 2012.

[52] A Jain, L Louahadj, J Peiro, JC Le Breton, C Vergnaud, A Barski, C Beigné, L Notin, A Marty, V Baltz, et al. Electrical spin injection and detection at al2o3/n-type germanium interface using three terminal geometry. *Applied Physics Letters*, 99(16):162102, 2011.

[53] FJ Jedema, HB Heersche, AT Filip, JJA Baselmans, and BJ Van Wees. Electrical detection of spin precession in a metallic mesoscopic spin valve. *Nature*, 416(6882):713–716, 2002.

[54] M Tran, H Jaffrès, C Deranlot, J-M George, A Fert, A Miard, and A Lemaître. Enhancement of the spin accumulation at the interface between a spin-polarized tunnel junction and a semiconductor. *Physical review letters*, 102(3):036601, 2009.